UNIVERSITY OF CALIFORNIA

Santa Barbara

Understanding Polymer-Fullerene Morphology in Organic Solar Cells via Photoluminescence, Raman Scattering, and Spectroscopic Imaging

A dissertation submitted in partial satisfaction of the

requirements for the degree Doctor of Philosophy

in Chemical Engineering

by

Christopher Andrew Carach

Committee in charge:

Professor Michael Gordon, Chair

Professor Michael Chabinyc

Professor Bradley Chmelka

Professor Ed Kramer

June 2014

The dissertation of Christopher Andrew Carach is approved.

_____

Professor Michael Chabinyc

_____

Professor Bradley Chmelka

_____

Professor Ed Kramer

_____

Professor Michael Gordon, Chair

March 2014

Understanding Polymer-Fullerene Morphology in Organic Solar Cells via Photoluminescence, Raman Scattering, and Spectroscopic Imaging

Christopher Andrew Carach

ACKNOWLEDGEMENTS

As much as I'd like to take sole credit for my ever-so-close Ph. D degree, to do so wouldn't be scientifically objective, and a slew of acknowledgements are in order. Being the left-brained being that I am, these will flow in an organized manner, with my somewhat-suppressed right-brained side effecting an unorthodox reverse-chronological order.

First I must offer my gratitude to my fellow laborers in the Gordon Lab – the old, the new, the in-between, and the eternal. To the *vieille garde* of Raphael, Travis, Isaac, and Louis: I'll always cherish the in-lab games and dreams (e.g., Sporcle.com and the 40-hour work week), the out-of-lab excursions (barbeques and baseball games), and the lessons I've learned from all of you. Raph, you taught me that French people actually like beer and good music, and offered a solid data point to support my assertion that the smartest guy in the room is usually the quietest. Travis, you've been a constant friend, roommate and drinking buddy all these years, and your assiduousness and self-reliance present a great example of the traits necessary to tackle the difficult (impossible?) task of achieving both research excellence *and* work-life balance. To my organic photovoltaic partner-in-crime Ike, I think we've facilitated a cultural exchange unsurpassed by Marco Polo and the Great Khan, trading expertise in March Madness brackets and American sports strategy for that in Magic cards and wild mushrooms! Louis, you've taught me that primary (or even tertiary) colors need not suffice in Powerpoint presentations, and have been a "colorful" conversation companion in both the technical (the finer points

of physical chemistry) and the inane (the bottoms of our oceans) ever since our fateful meeting in a UCSB recruiting van in March 2008. To *die zweite Welle* of Fed and Andrew, I thank you (selfishly of course) for perpetuating my interests in classical piano and 49ers fanship in the Gordon Lab for years to come! To my compatriot Alex Heilman(zadeh), I thank you for bringing the cuisine of Southwest Ohio to the Left Coast (Skyline chili dip!), even if you are from "south of the border", and I want to express in the most straight-laced way possible my regret that we never got to see each other in Lederhosen while stomping on tables in Bavarian beer halls! I've had several excellent undergraduate researchers and summer interns whose work has been enormously valuable (and indeed well-represented in the proceeding pages), and thus I am forever grateful to Martin, Eric, Calvin, and Jose for their skill and hard work.

Finally, Mike, I've learned so many things from you, some of which I've already forgotten (how to make a BNC cable without messing it up five times prior), some of which I'll soon forget (the mechanism of RF plasma formation), and some things I'll never forget (when in doubt, always add a 50-ohm terminator). Among the many items in the latter category I wish to highlight the most important, the most far-reaching, and the one I feel I will struggle to adequately describe: the self-confidence to tackle any technical challenge (regardless if the necessary apparatus is currently nonexistent – "We can build anything" is a phrase I heard you quite prophetically say during my first year in the lab, and might well serve as a Gordon Lab Motto displayed atop the door of Engineering II Room 3165); the stripping-

away of the mystique of as-purchased equipment and the fearlessness to look inside or take it apart; and the supremacy of one's own understanding of fundamental science over blind trust in the operator's manual. The ability to create, the disdain for dogma, the reductionism in peeling back a complex entity part-by-part to fully understand it…these are the traits of a true scientist, and I'm grateful to have learned them in my five years in your lab.

For a small-time Ohio boy whose only knowledge of the existence University of California came from big-time sports (the Bruins and the Bears), I must thank the man who first told me of the "other" UC campuses and helped push me towards Santa Barbara and the Gordon Lab: Professor Mohan Sankaran of my alma mater, Case Western Reserve University in Cleveland, Ohio. Mohan, I thank you for taking a chance on the tenderfoot chemical engineer whose first act in your lab was to dissolve in a flask the sawdust surrounding the $NaBH_4$ vial, thinking it was the actual chemical (did I ever tell you about this?). On the note of tolerating inexperienced and amusingly inept young engineers, my gratitude also goes out to Dr. Wei Fan and the engineers of the CVD team at Momentive (née GE Advanced Materials), who more than anything inspired me to seek a Ph.D. in Chemical Engineering.

The quality of education I've been so fortunate to receive predates both Santa Barbara and Case Western Reserve, and reaches all the way back to my primary (or is it secondary?) schooling in beautiful Austintown, Ohio. The doctorate in engineering I will soon receive builds upon all the math and science knowledge I've acquired since, well…ever since I've had math and science teachers! Tom Reardon,

Marla Morton, and Deborah Shell, I thank you for your excellent instruction in calculus, chemistry and physics, especially to a recalcitrant kid who refused to do his homework even though he certainly should have (yes, you were right!) Tim Tryon, you taught me how properly-balanced rockets fashioned from soda bottles (oops – pop bottles!) can fly seventy yards using compressed air, and Carl Pennington, you ignited my initial interest in math (and coached me through my initial hang-up on the difficult concept of negative numbers!). The fact that I remember your names after so many years is a testament to the effect you've had on my life through the quality of your teaching (and perhaps a testament to my absurd memory for detail), and I hope my future achievements will help justify what I believe is the crucial impact math and science teachers have upon society.

I've reserved my most important thank-you for the end, and I'll make it the shortest in an endeavor to make it the most poignant. To my family: Matt, you're the best brother anyone could ask for, and you're my best friend. Mom and Dad, the love and guidance you've always provided, the sacrifices of time and money you've made on my behalf, the selflessness you show by valuing my happiness even above your own…is (to borrow from Wigner) something I neither understand nor deserve. I owe everything to you.

All this science I don't understand; it's just my job five days a week.

- Elton John, *Rocket Man*

Life is a series of hellos and goodbyes; I'm afraid it's time for goodbye again.

- Billy Joel, *Say Goodbye to Hollywood*

CURRICULUM VITAE OF CHRISTOPHER ANDREW CARACH

March 2014

EDUCATION

Doctor of Philosophy in Chemical Engineering, University of California, Santa Barbara, March 2014

Bachelor of Science in Chemical Engineering, Case Western Reserve University, May 2008

PROFESSIONAL EMPLOYMENT

2010-2012: Teaching Assistant, Department of Chemical Engineering, University of California, Santa Barbara

PUBLICATIONS

I. Riisness, C. Carach, and M. J. Gordon. "Spatially resolved spectral mapping of phase mixing and charge transfer excitons in bulk heterojunction solar cell films." *Applied Physics Letters,* **100**, 073308 (2012).

C. Carach, I. Rissness, and M. J. Gordon. "Raman and low temperature photoluminescence spectroscopy of polymer disorder in bulk heterojunction solar cell films." *Applied Physics Letters,* **101**, 083302 (2012).

C. Carach and M. J. Gordon. "Optical Measures of Thermally Induced Chain Ordering and Oxidative Damage in Polythiophene Films." *Journal of Physical Chemistry B*, **117**, 1950, (2013)

PRESENTATIONS

"Raman and low temperature photoluminescence analysis of polymer disorder in bulk heterojunction solar cell films." Materials Research Society Spring Meeting, San Francisco, CA (2013).

ABSTRACT

Understanding Polymer-Fullerene Morphology in Organic Solar Cells via Photoluminescence, Raman Scattering, and Spectroscopic Imaging

by

Christopher Andrew Carach

Understanding and controlling carrier transport in conjugated polymer films and composites is critical to the development and application of plastic solar cells. Recent efforts have focused on "bulk heterojunction" structures where a conjugated polymer donor is mixed at the nanoscale with a fullerene acceptor to achieve large interfacial areas for exciton splitting. In these systems, fabrication protocols dramatically affect device efficiency and charge transport is intimately tied to film morphology through local order, domain formation, and compositional heterogeneity. We employ both far-field and confocal/near-field optical spectroscopy (absorbance, low-temperature photoluminescence, Raman) to study chain order (aggregation, π-stacking), photo-oxidation, and local morphology in conjugated polymer (PPV and polythiophene) – fullerene (PCBM) blends. Through quantitative analysis of exciton bandwidths, emission intensity, and vibronic lineshapes, we demonstrate that competition exists between the chemical "disordering" effect of photo-degradation and the physical "ordering" effect of aggregation, each of which dominate under different processing conditions. Large changes in photoluminescence and Raman show that PCBM begins to significantly

hinder intra-chain planarization and inter-chain π-overlap at a critical PCBM weight fraction. Furthermore, the critical weight fraction is a function of the polymer regiochemistry, occurring at lower PCBM weight fractions for a more regio-random polymer. Mild thermal annealing of blended films was seen to restore order, which results from PCBM phase segregation (lower dispersion) and growth of polymer aggregates. Spatially resolved spectral analysis of photoluminescence was also used to map fullerene diffusion and agglomeration as well as detect local changes in interfacial contact between donor and acceptor domains due to thermal annealing.

TABLE OF CONTENTS

LIST OF FIGURES AND TABLES

Figure ***Page***

Table ***Page***

Chapter 1

Organic Photovoltaics: Background and Motivation

The miracle of the appropriateness of the language of mathematics for the formulation of the laws of physics is a wonderful gift which we neither understand nor deserve.

- Eugene Wigner

1.1 Organic Photovoltaics as a Renewable Energy Source

Before diving into the world of *organic* photovoltaics, it is useful to take a step back and consider why one would study a photovoltaic in the generic sense. The primary motivation is rather obvious from the name alone – electrical energy, more specifically the "photovoltage" that arises upon illumination of a photovoltaic device by sunlight. Photovoltaics have found use in a myriad of applications in their half-century of existence, from the familiar (handheld calculators and communication satellites) to the less familiar (lighted Coast Guard buoys and microwave communication stations in remote locations).[1] However, the greatest future market for photovoltaic electricity, and the cause that has prompted so much photovoltaic research funding by Western governments, is not expansion into further niche applications, but rather wide-spread and large-scale application of photovoltaics for residential and industrial electricity. To understand the motivation for this, however, requires an analysis of the current world energy landscape.

Worldwide energy consumption currently sits at approximately 13 TW, and population and economic growth will likely cause this figure to more than double (~30 TW) by 2050.[2] Fulfilling this requirement is unquestionably one of society's greatest challenges in this half-century. But simply providing the requisite capacity is not sufficient – there is also an environmental constraint that must be met. Growing concerns of global warming due to greenhouse gas production have spurred interest in clean and renewable energy sources. Though the environmental ramifications of a warming planet will continue to be debated in both scientific and

political forums, it is probable that governmental support of clean energy sources and scarcity of fossil fuel energy sources will increase. It is therefore the job of the scientific community to develop clean energy sources that are scalable and economical.

There are relatively few energy sources in existence, and even fewer that are sustainable and scalable. For example, fossil fuel sources (oil, gas, and coal) have sufficient energy density and abundance but are not environmentally clean; renewable sources such as hydroelectric, tidal, and geothermal simply do not have the capacity to constitute a significant fraction of a 30 TW world energy budget. In fact, it has been argued that only nuclear energy, solar energy, and carbon-sequestered fossil fuels can provide the extra ~15 TW of clean energy needed in the next fifty years.[3] The sheer number of requisite nuclear power plants (1000 1 GW nuclear plants per TW) and sizeable uncertainty surrounding the feasibility of carbon sequestration leave solar energy standing alone. At first glance, this is not discomforting as the sun holds enormous promise as a clean energy source: it irradiates the earth with 120,000 TW, far in excess of the world's energy demand. Furthermore, solar energy is carbon-free and has a variety of methods by which it can be captured, converted and stored, including solar thermal, photovoltaic, and mock-photosynthetic solar fuels.

Despite the apparent advantages of solar energy, it makes up a minute fraction of even the renewable energy landscape, as seen in Figure 1.1a. The reason for this is simple, and is clearly depicted in the adjacent Figure 1.1b – it is simply too

expensive relative to other renewables as well as fossil fuels. Thus, for solar energy to ever be significant in a market economy that neglects externalities, a primary technical challenge is *significant reduction in cost per Watt*. This requirement applies to all forms of solar energy conversion (solar thermal, solar fuel, and photovoltaic), and each form has its own set of technical challenges that must be fulfilled to make it cost-competitive. This dissertation will focus on the technical challenges involved in the development of organic photovoltaics as an energy source.

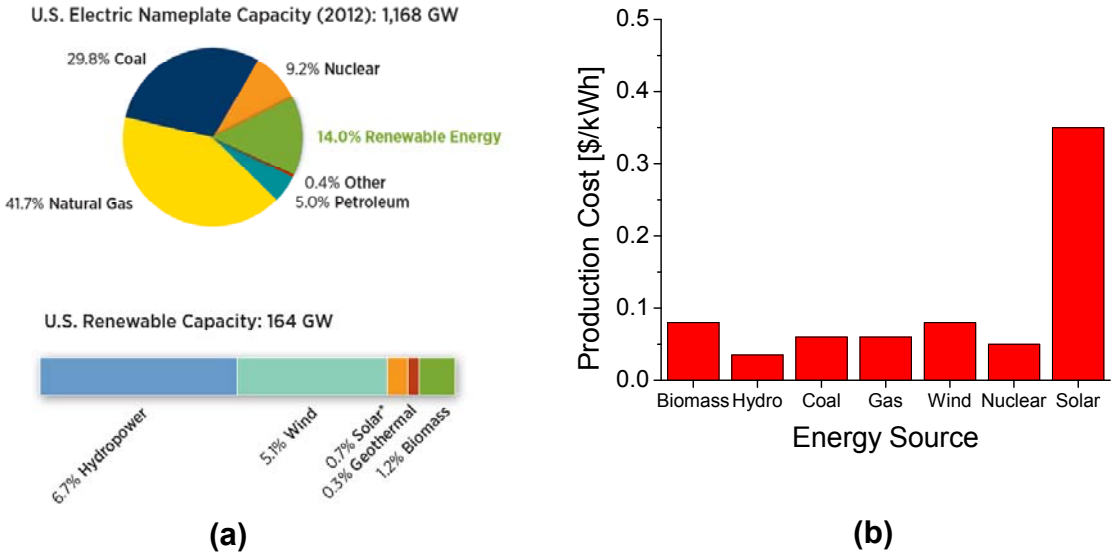

Figure 1.1 (a) 2012 U.S. electrical energy production by "Nameplate Capacity" (maximum rated output power of generator) by energy source. (Source: 2012 Renewable Energy Data Book, National Renewable Energy Laboratory). (b) Production cost by energy source (data from 2009 Transparent Cost Database, National Renewable Energy Laboratory).

Organic photovoltaics represent one of the latest manifestations of devices that create electric current from sunlight, the most primitive of which was demonstrated over one hundred fifty years ago. Edmund Becquerel is credited with the discovery of the photovoltaic effect in 1839 for his work on a photoelectrochemical cell.[4] The first account of photoconductivity in a solid sample (selenium sandwiched between platinum electrodes) was reported by Adams and Day in 1876.[5] It was not until the advent of semiconductors, however, that photovoltaic energy conversion was demonstrated, first by Chapin, Fuller, and Pearson at Bell Labs in 1954 (a 6% efficient single-crystal Si p-n junction).[6] Though interest in photovoltaics in the 1950s and 60s arose mainly from space applications, the 1973 oil embargo spurred significant funding for research and development of solar cells ("photovoltaics" and "solar cells" will be taken to be synonymous throughout). The evolution of solar cell efficiency since that time is displayed in Figure 1.2. Two initial observations are of importance: first, the efficiency of all types of solar cells has steadily (albeit slowly) increased, and second, there are large jumps in efficiency between each family of solar cells.

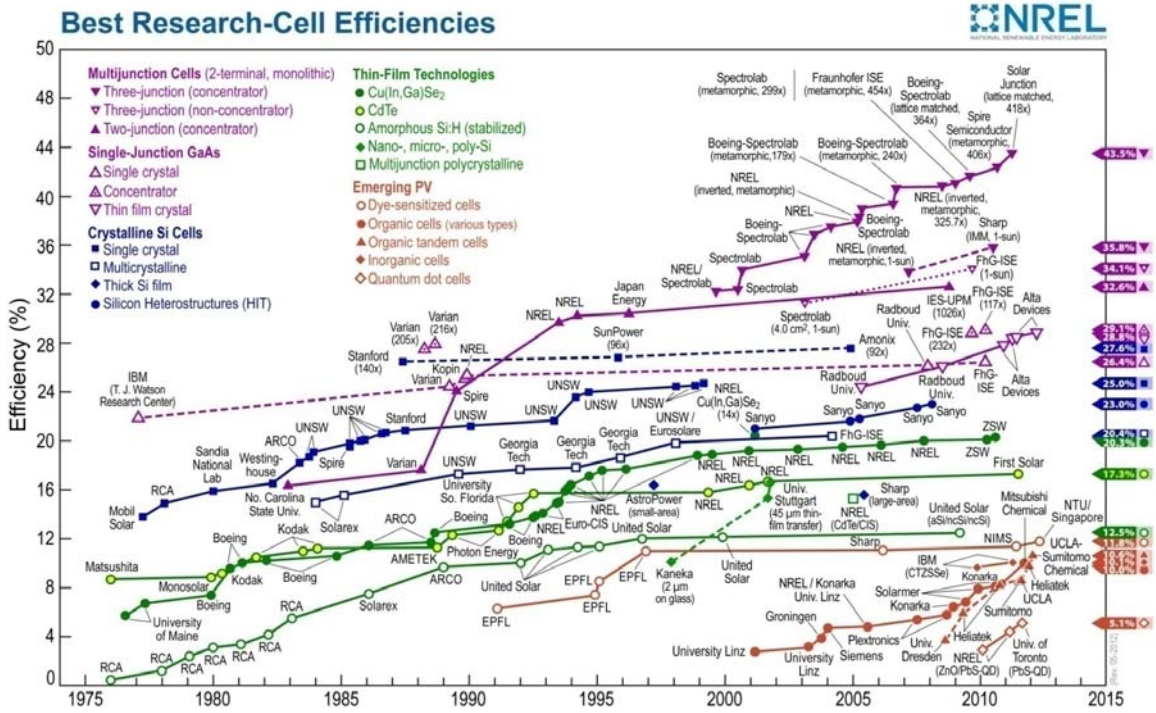

Figure 1.2 Best research cell efficiencies, 1975-present (National Renewable Energy Laboratory).

Excluding multijunction cells, the highest efficiencies to date are exhibited by crystalline Si cells (blue curves, ~25%), the successors to the original Bell Labs cell. The high efficiency can be ascribed to its high electrical mobility resulting from its ordered structure (crystalline lattice) as well as a favorable bandgap for solar absorption (reaching into the near-IR). However, the energy input associated with the melting, drawing, and dicing of high-purity single-crystal Si render these cells more expensive than some of their counterparts. Thin film solar cells (green curves), comprised of compound semiconductor heterostructures as well as amorphous silicon, can be less costly than single-crystal cells because they have less material (thickness 1-10 μm vs. 100-500 μm) and are less energy-intensive to produce.

Because thin film cells are inherently disordered (polycrystalline or amorphous), mobilities are lower than in monocrystalline cells. Additionally, several commonly used elements are very low in abundance (Te, Cd, In), making these devices ill-suited for large-scale application. Alone in the bottom right corner are the organic photovoltaics, unique in their late birth (1990s) and their low efficiencies (≤10% as of 2013). (Note: "organic" solar cells encompass dye-sensitized photoelectrochemical cells, small molecule cells, and polymeric cells; as the work in this dissertation only pertains to polymeric solar cells, "organic" solar cells will refer only to "polymeric" solar cells).

The low efficiencies of organic solar cells are due to their low electrical mobilities resulting from their inherently disordered microstructure, as well as their inability to absorb sunlight in the near-IR spectral region (in complete contrast with the attributes of single crystal Si solar cells). However, organic solar cells have two key advantages that keep them at the forefront of research despite their low efficiency, and they are closely linked: flexibility and cheap processing. Polymeric solar cells can be fabricated by so-called "roll-to-roll" processing techniques, whereby the solar cell precursor materials are solution deposited (e.g., slot coating, ink jet printing, screen printing) onto reams of flexible substrate (thin plastic or metal foil) in a continuous process under ambient conditions. Such processing avoids the costs associated with the high temperatures, high vacuum, and material purity requirements associated with crystalline Si solar cells. Furthermore, the resulting solar cells are thin (<500 nm) and flexible, making them amenable for niche

consumer applications and integration into curved architectures.[7] If mass-produced polymeric solar cells can achieve 10% efficiency and a 10-year lifetime, they could provide clean electricity cheaper than the monocrystalline Si and thin-film solar cell arrays currently on the market.[8]

1.2 Fundamental Science of Organic Photovoltaics

If cheap, clean renewable energy is the motivation for the study of organic photovoltaics from the perspective of the hard-nosed applied scientist or engineer, a completely different but equally valid argument can be offered by the starry-eyed theoretician – namely, organic photovoltaic materials lie in the uncharted waters of fundamental science. This assertion will become clearer upon examination of Figure 1.3. As pictured here, the behavior of any material lies somewhere on a continuum between two extremes. On one end, there are crystalline solids, where the close proximity of atoms and their fixed, periodic arrangement dictate their mechanical, electrical and optical properties. Such crystals can be said to be the limiting case of perfect order; monocrystalline silicon is a good example. On the other end are isolated molecules that, due to their lack of periodic placement and coupling to neighboring molecules, represent the opposite extreme of perfectly disordered materials. The benzene molecule is a good example. Interestingly, the theoretical description of each class of materials began to evolve at about the same time (ca. 1930) from the newly-established quantum theory. For example, Linus Pauling pioneered early work on chemical bonds in molecules and Erich Hückel developed

the molecular orbital description of cycloconjugated molecules such as benzene. Conversely, Felix Bloch found wave-like solutions to the Schrödinger equation for a periodic lattice, and Eugene Wigner studied the symmetry properties of these waves. Furthermore, each class of materials uses its own language. The molecular description invokes terms like molecular orbital and ionization energy whereas the solid state description talks about bands and work functions. However, the side-by-side glossaries of terms that first appear to lead to confusion actually lead to greater understanding once it is realized that each term in the molecular lexicon has an analogue in the solid state tongue, and vice versa. For example, the linear combination of atomic orbital (LCAO) method of constructing molecular orbitals in molecules is essentially the so-called "tight-binding" method of calculating band structure in solids;[9] the ionization energy of an atom of, say, sodium, is the energy required to pull the outermost electron to vacuum, whereas the work function of sodium is the energy required to pull a conduction band electron from a sodium metal surface; and an "excited state" or "donor" in the molecular parlance is synonymous with an "exciton" in a solid.

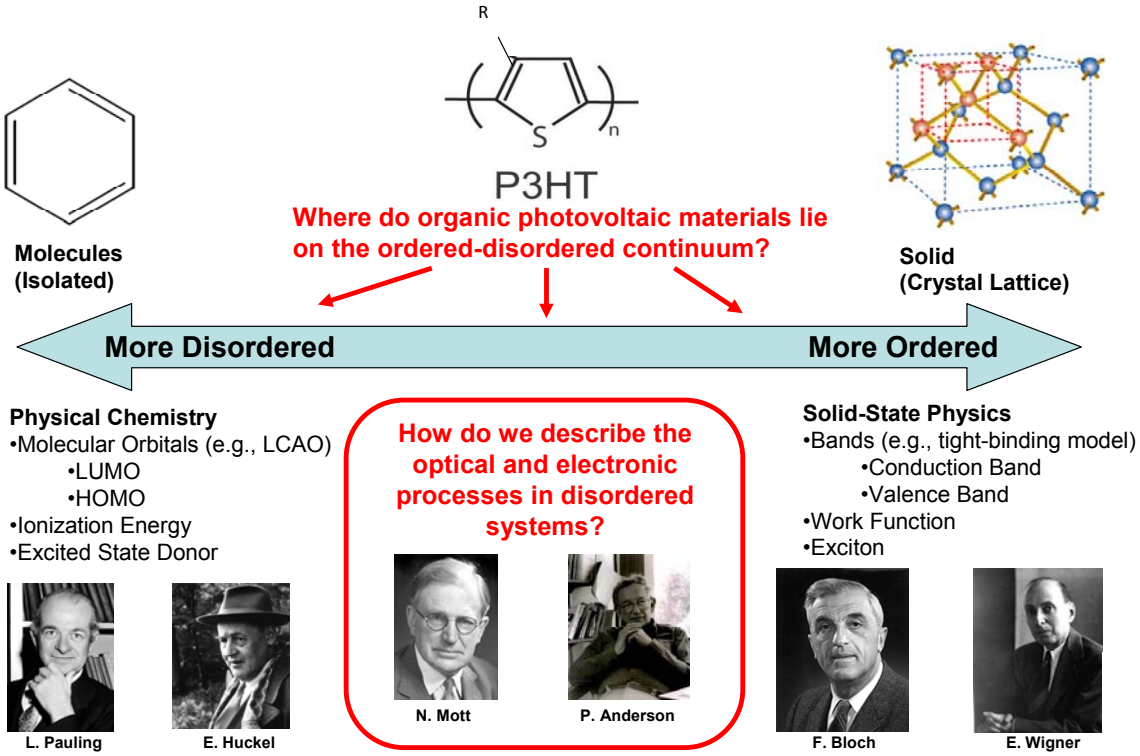

Figure 1.3 Illustration of the molecule-solid continuum.

This dissertation will borrow from the language of both molecules and solids, and that is because the materials studied herein (such as the archetypical conjugated polymer poly(3-hexylthiophene), shown in Figure 1.3) cannot be accurately described as either a solid or from a molecular framework. The true description of such materials would seem to lie somewhere in between. Furthermore, the place of a given material on the disordered-ordered continuum is not always fixed, but can be a function of its microstructure, which in turn is a function of processing conditions. As will be shown later, solid films of P3HT can be processed in such a way that creates more "ordered" or aggregated domains that more closely approximate the solid state, or can be processed in a way that leads to more isolated polymer chains

(more molecule-like). The theory to describe this "no-man's land" between molecules and solids is largely incomplete, and even the existing ground-breaking work (e.g., Mott and Anderson's theory of spin diffusion and electrical conductivity in amorphous solids)[10] is typically not universal but material-dependent, applying to some but not all materials that exist in the intermediately-ordered middle ground. Efforts to describe the electrical and optical properties of such systems usually employ, roughly speaking, either the molecular picture as a zeroth-order approximation with a first-order solid state perturbation, or the inverse. The modified H-aggregate theory that will be used here to describe the electro-optical properties of P3HT is an example of the former. Though the theoretical framework to explain the optical and electronic behavior of disordered materials is at the frontier of academic research and thus still evolving, much reliable groundwork has already been laid, some of which will be utilized here in the study of organic photovoltaic materials.

1.3 Optimizing the Performance of Organic Solar Cells

To understand how to improve the efficiency of an organic solar cell, it is necessary to understand the device structure and the device physics, both of which are quite different than that of the well-known silicon solar cell. These differences in structure and physics are due to several underlying differences in materials properties. Silicon and P3HT will continue to serve well as exemplars of well-ordered and disordered/intermediately-ordered materials, respectively. First,

consider the absorption coefficient: in general, indirect-bandgap monocrystalline silicon is a weaker absorber than most photovoltaic polymers by about an order of magnitude (see Table 1.1). The electrical transport properties are even more disparate.

Unsurprisingly, the electrical mobilities of ordered solids like monocrystalline silicon are much higher than materials like P3HT, as the former involves defect-free band transport and the latter is so disordered that charge transport is best described by a thermally-activated hopping mechanism. The magnitude of this disparity, however, may be surprising – a factor of 10^5 when comparing silicon (~1000 cm^2/Vs) to a typical organic semiconductor like P3HT (~10^{-2} cm^2/Vs). The Einstein relationship (easily abused, but shown to be valid even for organic semiconductors under most conditions)[11] can be used to link the electrical mobility to a charge carrier diffusivity:

$$D = \frac{\mu k_B T}{q} \tag{1.1}$$

where D is the diffusivity, μ is the mobility, k_B is Boltzmann's constant, and q is the elementary charge. Furthermore, using measured values of the charge carrier lifetime, and invoking a simple one-dimensional diffusion model,

$$L_D = \sqrt{D\tau} \tag{1.2}$$

a charge carrier diffusion length may be calculated (Table 1.1), where L_D is the diffusion length and τ is the lifetime. In the case of silicon, this diffusion length is on the order of a hundred microns; in the case of P3HT, it is only several nanometers. The implications of the diffusion length in organic photovoltaics will

be elaborated upon below, but for now it is important to note the combined effect of absorption coefficient and diffusion length on the length scale of each type of solar cell. The light-absorbing region ("active layer") of a solar cell should be thick enough to absorb most of the incident solar flux but not much thicker than the carrier diffusion length (otherwise charge extraction becomes inefficient). Thus commercial silicon solar cells are ~100's um thick, absorbing as much light as possible while not exceeding the diffusion length (cf. Table 1.1 and Figure 1.4a). In contrast, organic solar cells, with their increased absorptivity and much lower transport quality, are made much thinner (~100 nm).

Table 1.1 Comparison of material properties of an archetypical ordered solid (silicon) and the semi-ordered conjugated polymer poly(3-hexylthiophene) (P3HT). α is the absorption coefficient at 500 nm wavelength, μ is the electrical mobility, D is the positive charge carrier (hole) diffusivity, τ is the lifetime of conduction band charge carriers (excitons in the case of P3HT), L_D is the diffusion length given by Equation 1.2, and ε is the dielectric constant.

	α [cm^{-1}]	μ [cm^2/Vs]	D [cm^2/s]	τ [s]	L_D [m]	ε
Silicon	$\sim 10^4$	$\sim 10^3$	$\sim 10^1$	$\sim 10^{-6}$	$\sim 10^{-4}$	~15
P3HT	$\sim 10^5$	$\sim 10^{-2}$	$\sim 10^{-4}$	$\sim 10^{-9}$	$\sim 10^{-9}$	~3

Finally, the dielectric constants of solid state materials like silicon are typically much higher than those of organic materials like conjugated polymers (e.g., ε~15 in silicon vs. ε~3 in P3HT, see Table 1.1), which drastically modifies the nature of the photogenerated charge carriers in each case. Because of the additional electrical screening from the surrounding solid, photogenerated electrons and holes do not "feel" each other, so excitonic effects can be ignored in inorganic semiconductors

like Si or GaAs (more precisely, the electron-hole attractive Coulombic energy, or "exciton binding energy", is only several meV, so nearly all excitons will be ionized at room temperature).[13] Thus, referring to Figure 1.4a, electrons photogenerated in the p-doped silicon are instantly free carriers (no attraction to the left-behind hole), may diffuse to the p-n junction, drift across the junction due to the built-in field, and diffuse across the n-doped region where they may be extracted at the adjacent electrode (not pictured).

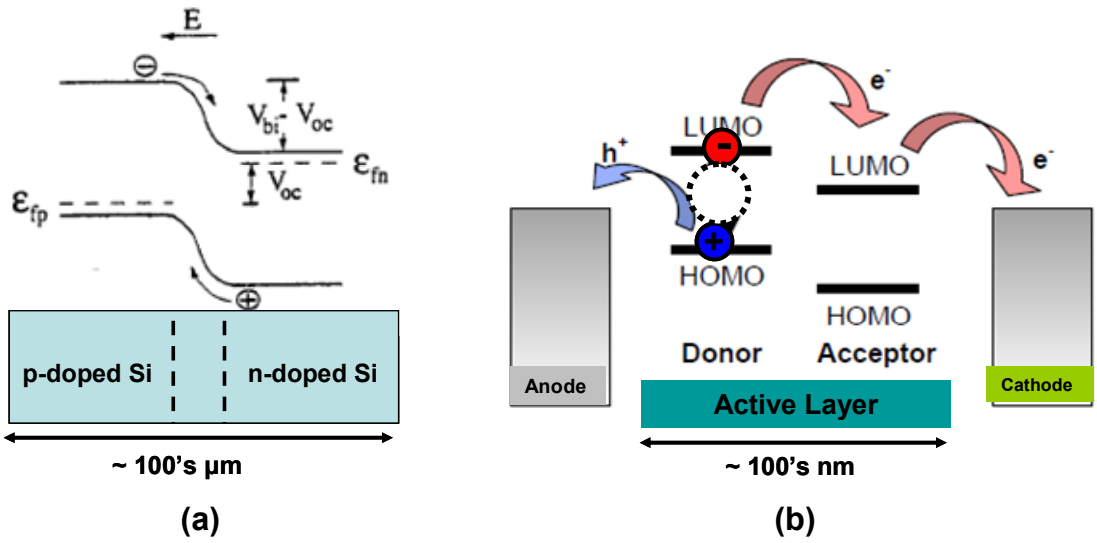

Figure 1.4 (a) Band structure of a p-n junction silicon solar cell. (b) Energy level structure of a donor-acceptor organic photovoltaic device.

In organic photovoltaics, the charge extraction process is not so simple. The lower dielectric constants of organic materials result in non-negligible exciton binding energies ($E_B \sim 1/\varepsilon^2$) – generally in the range of 0.1 to 1 eV.[13] Photogenerated electron-hole pairs thus take the form of tightly-bound (Frenkel)

excitons, which, due to their charge neutrality, are immune to the effects of local electric fields but may diffuse through the material in a random walk. However, exciton lifetimes and the corresponding diffusion lengths are short in organic materials, typically on the order of ns and nm, respectively (Table 1.1). Excitons can be dissociated, however, at an interface of the material they reside in and an adjacent material of different electronic structure – such a scheme is pictured in Figure 1.4b where an exciton created in a donor material can be dissociated at an acceptor material with a lower-lying LUMO. The electron "hops" to the acceptor and the hole remains in the donor. This is fundamentally a quantum-mechanical event that is best described in the framework of electron transfer theory (i.e., Marcus theory),[14] though, in a crude sense, the electron and hole may be said to be driven apart by the strong electric field at the interface due to the step change in electron affinity of donor and acceptor.[15] Once separate, the electron and hole are free to drift under the influence of the local field (set by an anode and cathode of differing work functions) and may be extracted from the device. (Note that an amended picture will be presented in Section 1.6 that introduces an intermediate charge transfer state after the electron hops across the interface; for now, the charges will be assumed to be free after electron transfer). A key requirement for making an effective organic photovoltaic, therefore, is to ensure that the exciton reaches a donor-acceptor interface before it recombines.

One possible architecture that attempts to satisfy this requirement is the bilayer heterojunction in Figure 1.5a. This method, however, largely fails as excitons more

than L_D away from the central interface recombine before having the chance to dissociate, and only excitons within L_D of the interface may be harvested. In a ~100 nm thick cell with an L_D of 5 nm, most excitons will be wasted. This explains, in part, the low efficiency (<1%) of early bilayer devices.[16] The architecture shown in Figure 1.5b may be considered the ideal architecture if the widths of the interdigitated donor and acceptor "fingers" are on the order of L_D. Not only will all excitons be split, but each resulting hole has a continuous path in the donor phase to the anode, and each electron has a continuous path in the acceptor phase to the cathode. This latter consideration is necessary because the anode material is chosen so that it selectively collects holes and the cathode material is chosen to collect electrons; therefore, the photogenerated holes remaining in the donor phase must be able to find their way to the anode and the electrons to the cathode. Thus, the two design criteria for organic solar cells are (1) donor-acceptor phase mixing on the order of L_D (i.e., the nanometer length scale) and (2) continuous pathways in each phase to the proper electrode. Though many research groups have tried to create the idealized structure shown in Figure 1.5b and thus satisfy these design criteria by, for example, incorporating the donor into ordered TiO_2 or using PDMS stamps and soft lithography,[17,18] such methods have not resulted in record efficiencies. The most common (and most effective) laboratory technique is to co-deposit from solution a donor-acceptor film, typically by spin-coating or "doctor blading". This results in a so-called "bulk heterojunction" structure, marked by a kinetically-frozen arrangement of donor and acceptor with high interfacial contact area (good

nanoscale mixing) but discontinuous transport pathways. Subsequent post-processing techniques like thermal or solvent annealing can then be used to induce an optimal amount of donor-acceptor phase separation, sacrificing some interfacial area for additional phase separation, leading to a morphology like that schematized in Figure 1.5c, with good (but not maximum) interfacial area and partially (but not fully) continuous charge transport pathways.

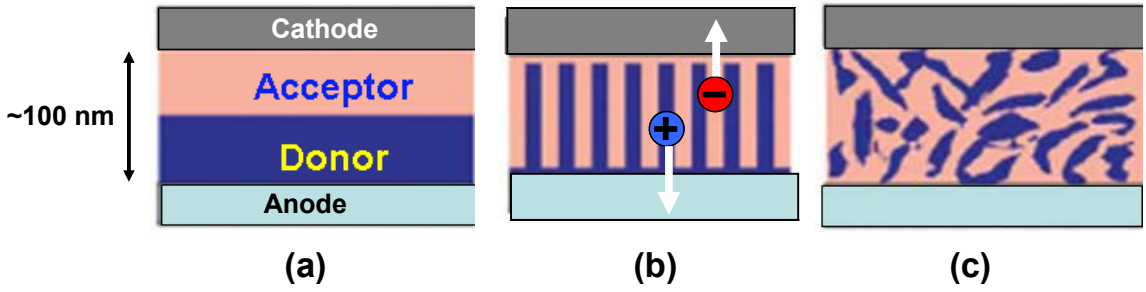

Figure 1.5 Schematics of a (a) bilayer heterojunction, (b) ordered heterojunction, and (c) bulk heterojunction.

In the case of the model P3HT:fullerene donor-acceptor system that will be studied in detail here, employing the technique of solution deposition plus post-processing has resulted in reported power conversion efficiencies of typically ~3-5%. The traditional experimental paradigm for optimizing this efficiency is to successively alter the processing conditions (e.g., solution concentration, annealing temperature, etc.) and then measure the solar cell performance through current-voltage testing under illumination. It is interesting to note that efficiencies in this range have been achieved with a wide variety of processing conditions: film thicknesses of 70-350 nm, thermal annealing times of 4-120 min, and thermal

annealing temperatures of 75-155 °C.[19] However, in the ten years over which the P3HT:fullerene system has been subject to intense study, the efficiency has never exceeded 5% despite hundreds of independent studies.[20] Taken together, these suggest that *you can make a ~5% efficient P3HT:fullerene solar cell by a nearly limitless choice of processing conditions, but no matter what processing conditions you choose, you will never make one with efficiency in excess of 5%.* The P3HT:fullerene system therefore seems to have reached the ends of its useful life as a subject of Edisonian trial-and-error.

While such an Edisonian approach may indeed succeed in progressively zeroing in on the optimal processing conditions (though this may be slightly less impressive when tempered by the fact that a wide array of processing conditions lead to the same optimal efficiency), the underlying phase mixing (morphology) that led to that optimal efficiency goes unexplored. A detailed knowledge of donor-acceptor phase mixing is certainly useful on the grounds of pure science – for example, correlating micro- or nano-scale morphology with macroscopic current-voltage measurements could provide information about charge transport in disordered systems. Such intimate knowledge of morphology is also essential to drive the efficiency of organic solar cells further. For example, much of the opportunity for further increasing device efficiency exists in the materials synthesis area. Any advance in creating a donor polymer with a higher hole mobility to enhance charge transport, a smaller bandgap to collect more near-IR radiation, or a lower-lying HOMO to increase the open circuit voltage would drive efficiency higher. Indeed, it has largely been new

donor polymers that have led to the record ~10% efficiency as of 2013. Each new polymer, though, must be optimally blended with the (fullerene) acceptor; a morphology optimization paradigm based on design rules that arise from a detailed understanding of donor-acceptor mixing may be more expedient than trial-and-error tuning of each new blend. With this in mind, donor-acceptor blends like P3HT:fullerene retain their utility as model systems on which to experimentally explore the morphology of conjugated polymer photovoltaics.

The research described in this dissertation makes use of spectroscopic tools like Raman scattering, low-temperature photoluminescence, and scanning confocal microscopy to form a picture of the micro- and nanoscale physical structure of organic photovoltaic systems. To do this, the spectroscopic data must be interpreted within the framework of the current knowledge of the electronic structure and electro-optical processes of conjugated polymers. In a nutshell, this research may be described as "theory plus spectroscopy yields knowledge about morphology." The remainder of this chapter, therefore, contains the necessary background information to understand the somewhat complex quantum chemical description of conjugated systems, the spectroscopic methods employed herein, and the current picture of donor-acceptor morphology in conjugated polymer:fullerene blends. Section 1.4 will introduce common organic photovoltaic materials, their structure, and their physical interactions. Section 1.5 describes the electronic structure of conjugated systems and Section 1.6 follows up with a discussion of electro-optical processes in

such systems. Finally, Section 1.7 summarizes the background information provided in Chapter 1 and briefly outlines Chapters 2-5.

1.4 Physical Structure of Organic Photovoltaic Materials

The proliferation of the conjugated, semiconducting polymers that are at the heart of organic photovoltaics was nearly as serendipitous as the proliferation of their saturated, insulating counterparts several decades before. Whereas accidental nickel contamination in the polymerization reactor of Karl Ziegler in the 1950s led to the discovery of low-temperature, atmospheric-pressure transition metal catalysts for the production of polyethylene,[21] catalyst overloading in the laboratory of Hideki Shirakawa in the 1970s led to the discovery of metal-like optical properties of cis- and trans-polyacetylene.[22] Subsequent work by Heeger and MacDiarmad showed that, through doping, polyacetylene could exhibit electrical conductivity spanning the gamut from insulator to metal,[23] thereby establishing the field of polymer electronics (and providing Heeger, MacDiarmid and Shirakawa the 2000 Nobel Prize in Chemistry). Since then, semiconducting and conducting polymers have found use in industrial applications such as light-emitting diodes (LEDs) and antistatic coatings, and offer promise in applications ranging from solar cells to RFID tags to transistors.[22]

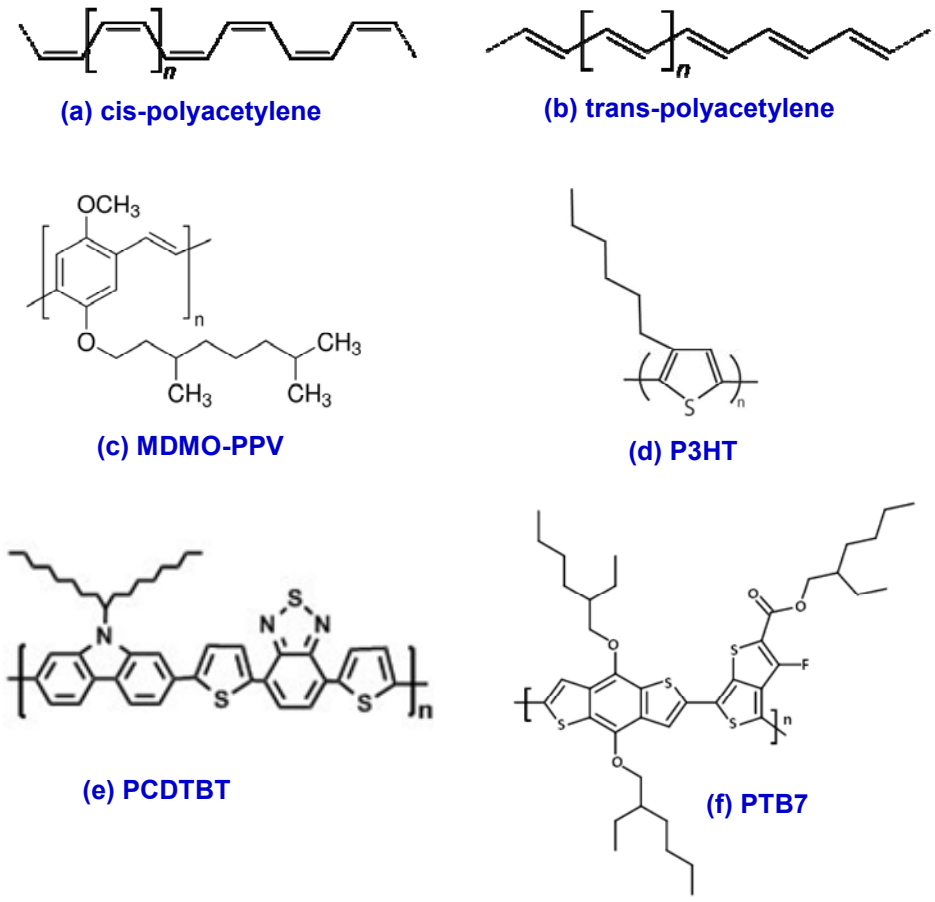

Figure 1.6 Chemical structure of (a) cis-polyacetylene, (b) trans-polyacetylene, (c) poly[2-methoxy-5-(3',7'-dimethyloctyloxy-1,4-phenylene-vinylene], (d) poly(3-hexylthiophene), (e) poly[N-9′-heptadecanyl-2,7-carbazole-alt-5,5-(4′,7′-di-2-thienyl-2′,1′,3′-benzothiadiazole)], and (f) poly({4,8-bis[(2-ethylhexyl)oxy]benzo[1,2-b:4,5-b′]dithiophene-2,6-diyl}{3-fluoro-2-[(2-ethylhexyl)carbonyl]thieno[3,4-b]thiophenediyl}).

Though neither cis- nor trans-polyacetylene (Figures 1.6a and 1.6b, respectively) developed widespread practical use, this most basic of conjugated polymers retains much use as a model on which to build the theoretical description of the optical and electrical properties of conjugated polymers. One drawback of polyacetylene is its poor processability due to a lack of solubility arising from very strong interchain

interactions. Solubility can, however, be promoted synthetically by the addition of alkyl side chains onto the monomer, and most conjugated polymers contain side chains of varying lengths (Figures 1.6c-f). Note that in the case of polyacetylene, adding a side chain would break the conjugation. Figure 1.6c shows a well-studied member of the poly(phenylenevinylene) family of conjugated polymers, MDMO-PPV (poly[2-methoxy-5-(3',7'-dimethyloctyloxy-1,4-phenylene-vinylene]). Like all members of the PPV family, it is electroluminescent and has been employed for use in LEDs. It was also the primary donor polymer for most polymer:fullerene photovoltaics in the late 1990s and early 2000s (the first bulk heterojunction solar cell was made from a PPV and C60).[24] When blended with fullerene derivatives, MDMO-PPV exhibits a rich variety of physical morphologies and optical effects, such as spectroscopically-observable charge transfer excitons, which will be described in Section 1.6 and studied in detail in Chapter 2. P3HT (Figure 1.6d) has dominated organic photovoltaic materials research since its first demonstration in a solar cell in 2001,[25] and, due to its commercial availability and excellent photovoltaic performance, still draws extensive research interest. The processing-structure relationships of neat P3HT films, P3HT:fullerene blends, and the response of P3HT films to photo-oxidation encompasses much of this dissertation. More recent advances in photovoltaic polymers are usually based on more complex thiophene-containing monomers; two examples are PCDTBT (Figure 1.6e, poly[N-9′-heptadecanyl-2,7-carbazole-alt-5,5-(4′,7′-di-2-thienyl-2′,1′,3′-benzothiadiazole)]) and PTB7 (Figure 1.6f, poly({4,8-bis[(2-ethylhexyl)oxy]benzo[1,2-b:4,5-

b′]dithiophene-2,6-diyl}{3-fluoro-2-[(2-ethylhexyl)carbonyl]thieno[3,4-b] thiophenediyl}). In addition to having chemical names that take up nearly two full lines of text, these polymers push solar cell efficiencies toward 10%, mostly due to their lower bandgaps and thus higher fractions of harvested photons. Further improvements in conjugated polymer photovoltaic performance will require the synthesis of conjugated polymers that have even lower bandgaps, while retaining reasonably high mobilities and HOMO/LUMO levels that still facilitate electron transfer to acceptor molecules.

Conjugated polymers such as those shown in Figure 1.6 are certainly not naturally occurring, and much gratitude is due to the synthetic chemists for their discovery and development. The first conducting polymer, polyacetylene, was first synthesized by Natta in 1958 from acetylene using the same addition polymerization and organometallic catalysts (i.e., "Ziegler-Natta" catalysts) originally used by Ziegler in the synthesis of polyethylene.[22] The synthesis of the most widely-used conjugated polymers of the last few decades relies, however, upon polymerization via the cross-coupling chemistries developed largely by the Japanese in the 1970s (e.g., Kumada coupling, Suzuki coupling, Yamamoto coupling). PPVs like MDMO-PPV in Figure 1.6c are often synthesized by the Heck coupling reaction, for example, whereby a benzene derivative is coupled with a vinylbenzene derivative over a palladium catalyst.[27] The synthetic procedures are of more than historical interest, however, because the synthetic conditions affect polymer properties (e.g., molecular weight, polydispersity, presence of defects, impurities), which then affect physical

properties, which further affect electro-optical properties. P3HT is very illustrative of this point. The schematic of the P3HT monomer shown in Figure 1.6d is somewhat misleading in that it does not depict all possible permutations of monomer linkages. Because 3-alkylthiophenes like P3HT are asymmetric, there are three ways in which two adjacent thiophene monomers can link together: a so-called "head-to-tail" linkage, a "head-to-head" linkage, or a "tail-to-tail" linkage (Figures 1.7a, b, and c, respectively). The linkage distribution drastically affects the physical and electro-optical properties of both isolated polymer chains and solid films. The presence of "head-head" linkages causes intrachain torsional deformation due to steric repulsion (twisting of thiophene units – see Figure 1.7d) and an accompanying loss of conjugation. This steric repulsion also inhibits interchain packing (π-stacking). In both cases, this results in blue-shifted absorbance and luminescence and lower conductivity. P3HT containing a significant fraction of head-to-head or tail-to-tail linkages is termed "regiorandom"; conversely, "regioregular" P3HT is composed of (ideally) 100% head-to-tail linkages, which leads to planar backbones and facilitates π-stacking (Figure 1.7e).

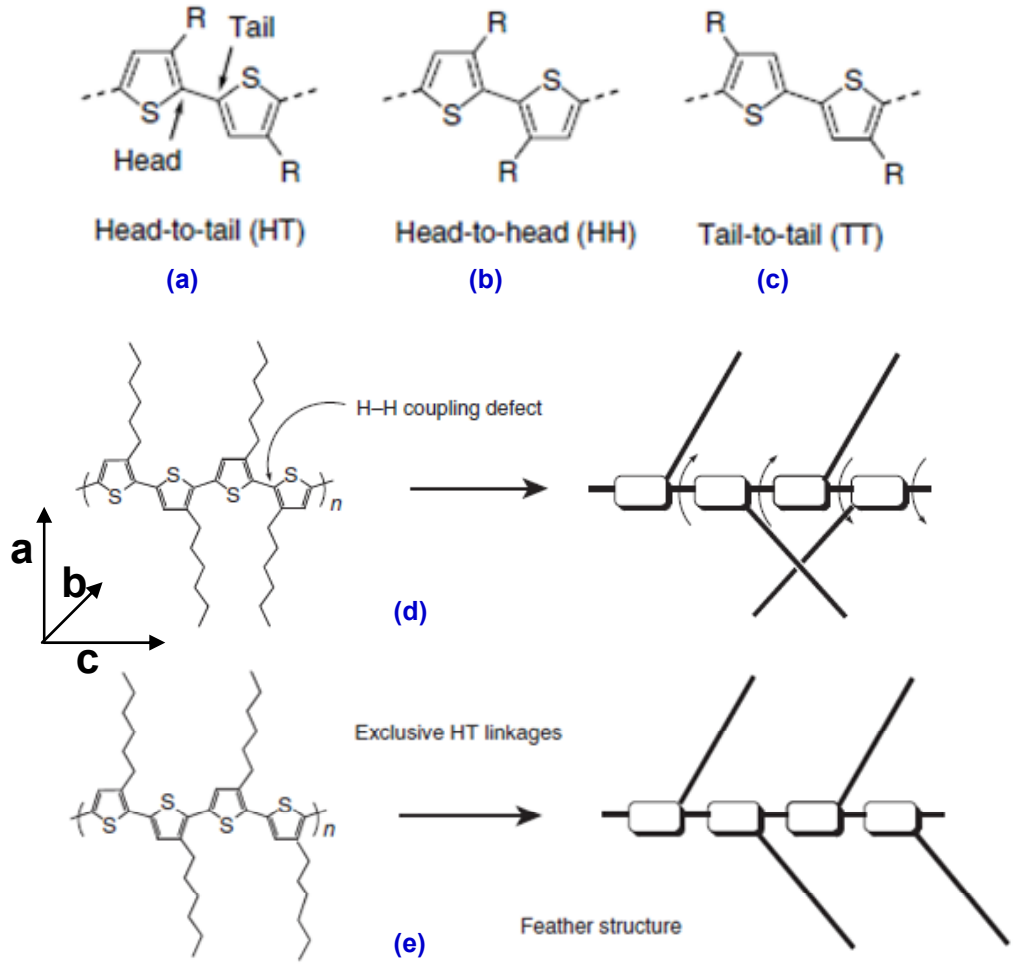

Figure 1.7 Chemical drawings of (a) head-to-tail, (b) head-to-head, and (c) tail-to-tail couplings in P3HT; (d) shows the torsional defect from steric hindrance of alkyl side chains resulting from a head-to-head linkage. (e) Consecutive head-to-tail linkages lead to a defect-free, planar structure.

The regiochemistry of P3HT is controlled solely by synthetic conditions. Thiophene precursors used in P3HT synthesis typically involve adding halogens or other reactive leaving groups to the 2- and 5- (head and tail) positions of the thiophene ring; the 4-position is thus rendered unreactive. At first glance, it would then seem that synthesis would lead to 50% head-to-tail linkages (there are four

possible permutations for two monomers: head-head, head-tail, tail-tail, and tail-head); however, steric effects make head-to-tail couplings more favorable (up to from 70-88%, depending on temperature and monomer concentration).[28] Achieving a greater fraction of head-to-tail linkages requires some built-in synthetic bias. One such method, the so-called "Rieke" synthesis, adds dissimilar leaving groups at the head and tail positions of the 3-hexylthiophene precursor (bromine and a zinc-bromine complex). A nickel polymerization catalyst then leads to regioregular P3HT (>98% head-to-tail couplings) and a palladium catalyst results in regiorandom P3HT (~50% head-to-tail couplings).[29] Regioregularity may be assessed using ^{1}H NMR, as described in Section 2.7.

Regioregular P3HT forms solid films that share many physical characteristics with films of other alkylated conjugated polymers, marked by their stiff backbones and flexible side chains. The films are neither ordered nor fully disordered, but are semicrystalline, having coexisting amorphous regions and π-stacked "crystalline" domains. The structure of P3HT is fully three-dimensional, and one can consider three independent packing axes: the a-axis along the direction of the alkyl side chains, the b-axis along the direction of π-stacking, and finally the c-axis along the length of the polymer chain (see Figure 1.7). The lattice spacing of P3HT along the b-axis is ~0.4 nm and along the a-axis is ~1.6 nm.[30] P3HT chains can further fold back upon themselves in the c-axis forming lamella, leading to an array of lamellar crystalline domains and amorphous interlamellar zones.[31] The π-stacked planes can take any angle from zero to ninety degrees with respect to the substrate. For P3HT

under most processing conditions, the π-stacks align perpendicular to the substrate ("edge-on", a-axis perpendicular to the substrate); for comparison, PCDTBT π-stacks lie parallel to the substrate ("face-on", b-axis perpendicular to the substrate). However, it is important to note that solid film morphology is a strong function of processing conditions. For example, though P3HT self-organizes into edge-on orientation given sufficient time (e.g., solution casting from a high boiling point solvent), spin-coating from a rapidly-evaporating solvent like chloroform leads to a kinetically-frozen structure with face-on π-stacking. The solid film morphology is also a function of the polymer properties: spin-coating low molecular weight P3HT leads to the formation of nanorods, whereas spin-coating high molecular weight P3HT produces dense, spherical nodules.[32] Finally, it should be noted that more exotic P3HT structures can be created, such as nanofibers in solution from controlled cooling in a bad solvent[33] or growing millimeter-scale spherulitic domains using CS_2 vapor pressure to control the nucleation rate.[34] However, this dissertation will focus on the more conventional spin-cast P3HT thin films that are conducive for use in organic solar cells.

Conjugated polymers like P3HT only represent one half of the requisite materials in the active layer of organic solar cells – an acceptor material must be present to accept charge from the donor. Whereas the list of donor polymers that have been used to make efficient solar cells is much more extensive than the several model examples shown in Figure 1.6, the list of well-performing acceptor molecules is quite small, and for all practical purposes may be considered to be completely

contained within Figure 1.8. The buckminsterfullerene molecule ("buckyball" – Figure 1.8a) found quick application in organic solar cells just seven years after its discovery by Smalley et al. in 1985, and has dominated the field ever since. Fullerenes are well-suited for use as electron acceptors due to their high electron affinities and decent electron conductivities (10^{-4} S/cm).[35] Though many non-fullerene acceptor molecules have been synthesized and tested in organic solar cells, nothing has superceded the performance of C_{60} and its derivatives. Soon after the demonstration of a bilayer device of vacuum-deposited C_{60} on PPV in 1993,[36] the soluble fullerene derivative PCBM (phenyl-C_{61} butyric acid methyl ester, Figure 1.8b) allowed for the first true conjugated polymer – fullerene bulk heterojunction through solution-based co-deposition. This device achieved a then-record efficiency of 1%.[37] In the two decades since, PCBM has been the workhorse acceptor molecule, and its performance has only been superceded by its closely related cousin $PC_{71}BM$ (phenyl-C_{71} butyric acid ethyl ester, Figure 1.8c), whose slightly higher electron affinity and slightly lower bandgap result in slightly higher power conversion efficiencies. As of 2013, the PTB7:$PC_{71}BM$ system can be taken to be the most efficient bulk heterojunction solar cell, with efficiencies approaching 9%.[26] This work, however, will focus on the donor-acceptor nanomorphology and dynamics in the model PPV:PCBM and P3HT:PCBM systems.

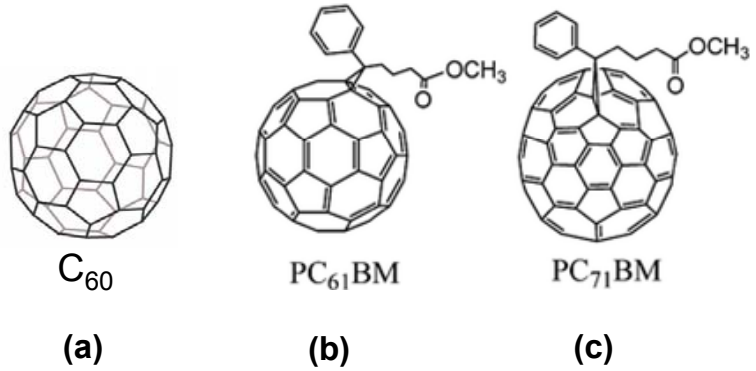

Figure 1.8 Chemical drawings of (a) buckminsterfullerene and two fullerene derivatives commonly employed as electron acceptors in organic photovoltaics: (b) phenyl-C_{61} butyric acid methyl ester, and (c) phenyl-C_{71} butyic acid methyl ester.

The current state of understanding about the morphology of such systems is very unsettled. In the case of the P3HT:PCBM system, there is no consensus review with regards to the morphology, the equilibrium phase diagram, vertical (i.e., anode-to-cathode) phase segregation, or the mechanism of phase segregation, despite a decade of research and more than a thousand publications.[38] For example, one study employing differential thermal calorimetry (DSC) found that the P3HT:PCBM binary system exhibits eutectic phase behavior,[39] while the results of another study also employing DSC contradict those results.[40] Moreover, the dynamics of fullerene diffusion and polymer crystallization upon thermal annealing has long been debated and is still unresolved. Recent studies using grazing-incidence x-ray scattering conclude that P3HT crystallite growth is completely independent of the local concentration of PCBM,[41] and, conversely, that the local PCBM concentration influences the kinetics of P3HT domain growth.[42] It is also debated as to whether PCBM molecules diffuse to form crystals[43] or amorphous agglomerates.[41] The list

of discrepancies goes on. It is perhaps more useful at this point, however, to state the several broad themes underlying the morphology of polymer:fullerene systems that are beyond dispute. First, the morphology or microstructure of a polymer:fullerene blend should be analyzed in terms of its "distance" from the equilibrium structure at that temperature and composition. Virtually all commonly-used thin film deposition methods (e.g., spin-coating and doctor-blading) result in a kinetically-frozen, nonequilibrium polymer-fullerene morphology. Post-deposition thermal or solvent annealing of the as-cast morphology push the morphology closer to equilibrium (though likely still in a nonequilibrium, metastable state) and has been empirically found to result in higher device efficiency, mostly through an increase in the short-circuit current density. This final structure is a complex function of many factors, including properties intrinsic to the materials (e.g., miscibility and crystallinity) as well as processing conditions (e.g., solvent, relative concentrations of polymer and fullerene, overall concentration in solution, thermal annealing time and temperature, etc.).[44] While the precise, nanometer-resolved picture of this optimized morphology is still unknown (and is very much the "holy grail" of this field of research), a few general characteristics of this morphology are now agreed upon. Whereas early publications on polymer:fullerene systems advocated a black-and-white (or rather a blue-and-pink) two-phase picture like the simple caricatures in Figure 1.5, it is now widely accepted that there is a third, mixed phase of amorphous polymer and isolated fullerene molecules to go along with the pure polymer and pure fullerene phases. With regards to the P3HT:PCBM system in particular, at ~50%

PCBM by weight, there exists P3HT crystallites, PCBM agglomerates, and a large mixed phase of PCBM molecules dispersed within amorphous P3HT,[41,42] described more accurately by a schematic such as that in Figure 1.9.[41] This picture will vary for other systems; for example, the miscibility of PCBM in MDMO:PPV is much lower than in P3HT, and there will be a smaller ratio of the mixed phase relative to the pure phases at the same PCBM weight fraction.[44]

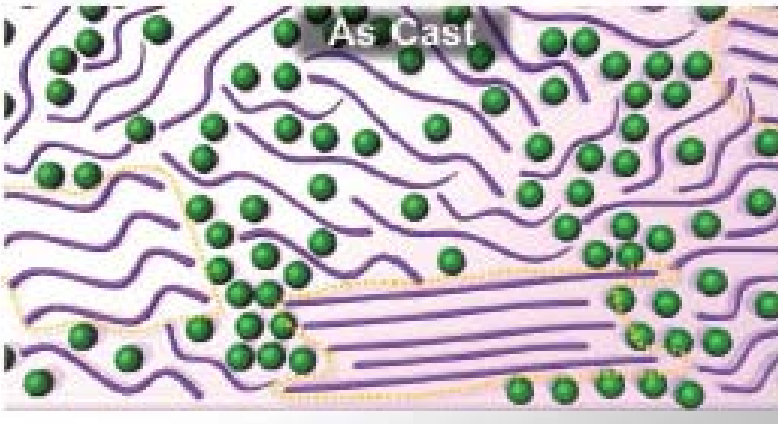

Figure 1.9 Hypothetical morphology of an as-cast P3HT:PCBM thin film. Green circles represent individual fullerene molecules; purple lines are P3HT chains, which may exist as isolated chains (squiggly lines) or crystalline aggregates (close-packed straight lines). Reproduced from Treat, et al. [41].

The low miscibility of PCBM in MDMO:PPV, however, goes hand-in-hand with phase instability, which highlights a final important point – the metastability of optimized polymer:fullerene blends is a hindrance to the lifetime of organic solar cells. The steady-state temperature of organic solar cells in the field can exceed 60 °C,[45] at which temperature PCBM diffusion can be seen in P3HT after only several minutes.[41] Thus, prolonged solar exposure can lead to further morphological

evolution to equilibrium that is undesirable, marked by too much phase separation and too little interface. Though such considerations of device degradation are often an afterthought in academic research, device lifetime is hugely important to the commercialization of organic photovoltaics, where lifetimes in the field will need to reach ~10 years.[19] To this end, Chapter 4 will focus on the dominant degradation mechanism in polymeric solar cells, which is photo-oxidation of the conjugated backbone. Specifically, it will discuss how the same optical spectroscopies that are employed to elucidate the polymer:fullerene morphology may also be employed to deconvolute the concurrent polymer ordering and chemical damage that occurs during thermal annealing in the presence of light and oxygen. Interpretation of such spectroscopic data, however, requires a thorough understanding of the electronic structure of conjugated polymers, which is discussed next.

1.5 Electronic Structure of Organic Photovoltaic Materials

Any description of the electronic structure of disordered materials such as conjugated polymers should take place with the molecule-solid continuum from Section 1.2 illuminating the backdrop. As alluded to in that section, the treatment here can be thought of as a solid-state perturbation to a fundamentally molecular picture of electronic structure (and indeed if one was forced, for the sake of debate, to choose whether conjugated polymers were "molecules" or "solids", the molecular argument may be on more solid footing). With this in mind, it is useful, perhaps, to begin with a brief mention of the electronic structure of simple non-interacting

molecules, then proceed to small aggregates of these molecules (dimers), before finally proceeding to more extensive structures such as semi-crystalline conjugated polymers.

The electronic structure of small aromatic molecules is largely review for most students of chemistry, but it is useful to reiterate several well-known concepts, and perhaps also to emphasize a few overlooked ideas. First, the definition of "molecule" as it is used here is somewhat broad, and can refer to an entity as small as the benzene molecule in Figure 1.3 to one as large as a polyacetylene (macro)molecule of arbitrary molecular weight, as in Figure 1.6. The key point is that these molecular entities are independent and *non-interacting* electronically; aggregates and crystals are composed of interacting molecules and will be discussed in the proceeding paragraphs. These conjugated (alternating single- and double-bonded) molecules and macromolecules all contain a carbon-based "backbone" and are formed by σ and π orbitals. To visualize these orbitals, it is helpful to draw on ideas from both the earlier valence bond theory (Pauling, c.f. Figure 1.3) as well as molecular orbital theory. Conjugated molecules are unsaturated molecules by definition, and thus the concept of orbital hybridization (valence bond model) is informative. All conjugated polymers are sp^2 hybridized (with the exception of the sp-bonded polydiacetylene, not shown), and accordingly are planar structures with the σ bonds composed of 3 sp^2 orbitals at ~120° angles (exactly 120° for benzene and, interestingly, ranging from ~117º to 124º for trans-polyacetylene).[46] The remaining p_z orbital forms the π bond orthogonal to the plane of the molecule.

Electrons in these π orbitals, however, delocalize (i.e., "conjugate") throughout the molecule, and are more aptly described by delocalized molecular orbitals. The first molecular orbital model for planar, sp^2-hybridized molecules was given by Hückel (Figure 1.3) in 1930.[47] Though it is extremely simplified (ignoring all σ orbitals) and only accurately predicts energies of small molecules like ethylene and benzene, it provides several results that will, perhaps surprisingly, hold true for much more complicated conjugated macromolecules. First, the highest occupied molecular orbital (HOMO) is the highest-energy π orbital, and the lowest unoccupied molecular orbital (LUMO) is the lowest energy π* (antibonding) orbital. Furthermore, the HOMO-LUMO energy gap (band gap) is inversely proportional to the number of carbon atoms; a larger molecule has a lower-energy ("red-shifted") band gap. This can be extended to macromolecules, where polymers with longer conjugation lengths (uninterrupted alternating single and double bonds) exhibit red-shifted absorbance and luminescence. Similarly, the Hückel treatment can be extended to a non-simplified, fully-general model where the molecular orbitals are constructed from the superposition of atomic orbitals:

$$\psi_k = \sum_r c_{kr}\phi_r \qquad (1.3)$$

where the φ_r are atomic orbitals, the c_{kr} are coefficients, and the ψ_k are the resulting molecular orbitals. This is the well-known linear combination of atomic orbitals (LCAO) method, or the "tight-binding" approach in the language of solid-state physics.[48] Equation 1.3 can be further refined when applied to a one-dimensional periodic array of atoms such as a conjugated polymer. Here, the long-range

translational symmetry of the N adjacent monomers is analogous to that of a semi-infinite crystal lattice, and thus the molecular orbitals can be approximated by the so-called Bloch functions (Figure 1.3) that reflect the periodicity of the lattice:

$$\psi_k = \sum_{r=0}^{N-1} e^{ikra} \phi_r \qquad (1.4)$$

Such a method can be used to calculate the electronic structure of both conjugated polymers like polyacetylene as well as its non-conjugated analogue polyethyelene.[48] It is very important to note, however, that such a tight-binding approach is an approximation that neglects both electron-electron interactions (e.g., screening and exchange) and electron-phonon interactions ("vibronic coupling"). Both electron-electron and electron-phonon coupling are significant in organic semiconductors. The manifestations of these effects in the electronic structure and electro-optical processes of conjugated polymers will be discussed later; now it is time to consider the electronic structure of aggregates of conjugated molecules.

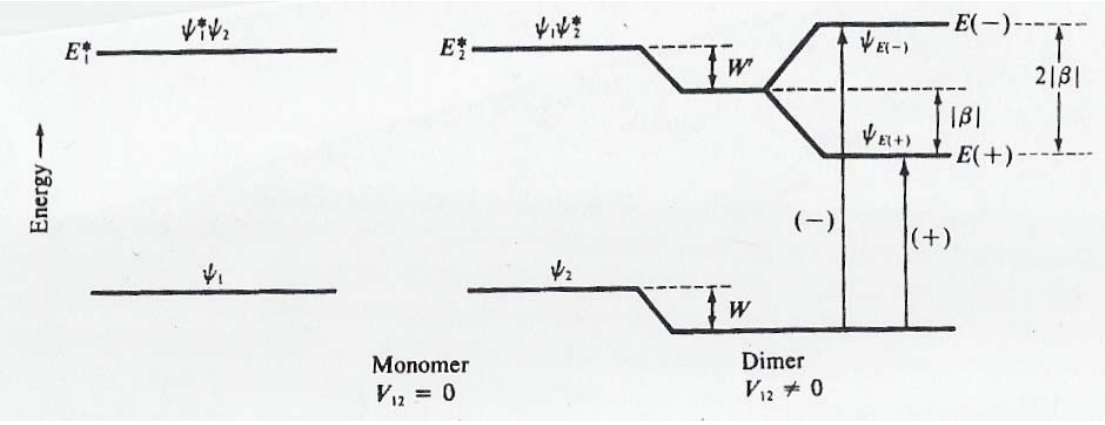

Figure 1.10 Ground and first excited state energy levels of (a) a molecule or monomer, and (b) a dimer. ψ_1 and ψ_2 are the wavefunctions of molecules 1 and 2, V_{12} is the intermolecular interaction energy given in Equation 1.5, W' is the Coulomb intregral given in Equation 1.9, and β is the resonance integral from Equation 1.10. The energy level splitting of the first excited state is 2 β for a dimer. Reproduced from [49].

The smallest molecular aggregate is simply a dimer, and it is in dimers that the departure from single-molecule electronic structure is first seen. Consider two identical molecules, which can be abstractly represented as two point dipoles. A Hamiltonian of this two-molecule system can be written as:

$$H = H_1 + H_2 + V_{12} \tag{1.5}$$

where H_1 and H_2 are the isolated-molecule Hamiltonians for molecules 1 and 2, and V_{12} is the intermolecular interaction energy. The V_{12} intermolecular coupling term has a marked effect on the structure of the ground state energy and the lowest excited states (see Figure 1.10). The ground state energy is lowered (and thus stabilized) by the so-called Coulomb integral W:

$$E_g = E_1 + E_2 + W \tag{1.6}$$

and the energy of the lowest excited states is split according to the Coulomb integral W and resonance integral β:

$$E(\pm) = E_1 + E_2 + W' + \beta \tag{1.7}$$

where

$$W = \langle \psi_1 \psi_2 | V_{12} | \psi_1 \psi_2 \rangle \tag{1.8}$$

$$W' = \langle \psi_1^* \psi_2 | V_{12} | \psi_1^* \psi_2 \rangle \tag{1.9}$$

$$\beta = \langle \psi_1^* \psi_2 | V_{12} | \psi_1 \psi_2^* \rangle \tag{1.10}$$

and ψ_1 and ψ_2 are the ground state wave functions of molecules 1 and 2.[49] (It is instructive to note that this simple buildup of aggregate orbitals from independent molecules is analogous to the buildup of molecular orbitals from individual atoms in Hückel theory; the Coulomb and resonance integrals play the same role in both treatments). As shown in Figure 1.10, there are two possible optical transitions from the ground state to the excited states. The relative strengths of the two transitions are a function of the alignment of the transition dipole moments of the two molecules composing the dimer. Consider a parallel or face-to-face arrangement of molecules such as that shown in Figure 1.11a. Here, the transition dipole moments are orthogonal to an imagined intermolecular packing axis (marked "r" in Figure 1.11a). Because the transition dipole moment couples the ground state to the bonding excited state molecular orbital of the dimer,[51] and this bonding orbital is at a higher energy than that of the monomer (by an amount equal to the resonance integral β, c.f. Figure 1.10), the absorbance is blue-shifted. Conversely, when the transition dipole moments are oriented collinearly with respect to the packing axis, the transition

dipole moment couples the ground state to a lower-energy excited state bonding orbital, and the absorbance is red-shifted (Figure 1.11b). Though the precise reasons for the preferred dipole couplings and opposite energy splitting are beyond the scope of this text (involving consideration of coherent dipolar coupling of the excited state energy from molecule to molecule),[51,52] Figure 1.11c makes the picture a bit more clear.[53] It shows that the dipole-allowed bonding orbital (dark curve) as a function of the angle α between the stacking axis and transition dipole moment vector. From the limit of perfectly collinear stacking to the "magic angle" of 54.7°, absorbance will be red-shifted with respect to the monomer; between 54.7° and the 90° face-to-face stacking limit, absorbance is blue-shifted (note the analogy to the magnetic dipole coupling that is prominent in the analysis of magnetic resonance). This treatment can easily be extended to aggregates larger than dimers: collinearly-stacked aggregates have red-shifted absorbance with respect to the monomer (by an amount 2β for trimers and larger) and are referred to as "J-aggregates". Similarly, an aggregate of face-to-face molecules, with blue-shifted absorbance, is termed an H-aggregate. These terms became prominent when characterizing the unique properties of many organic dyes – J-aggregated dye molecules are "superluminescent" and emit brightly, while H-aggregates are "dark" due to their dipole-forbidden emission from the lower excited state.

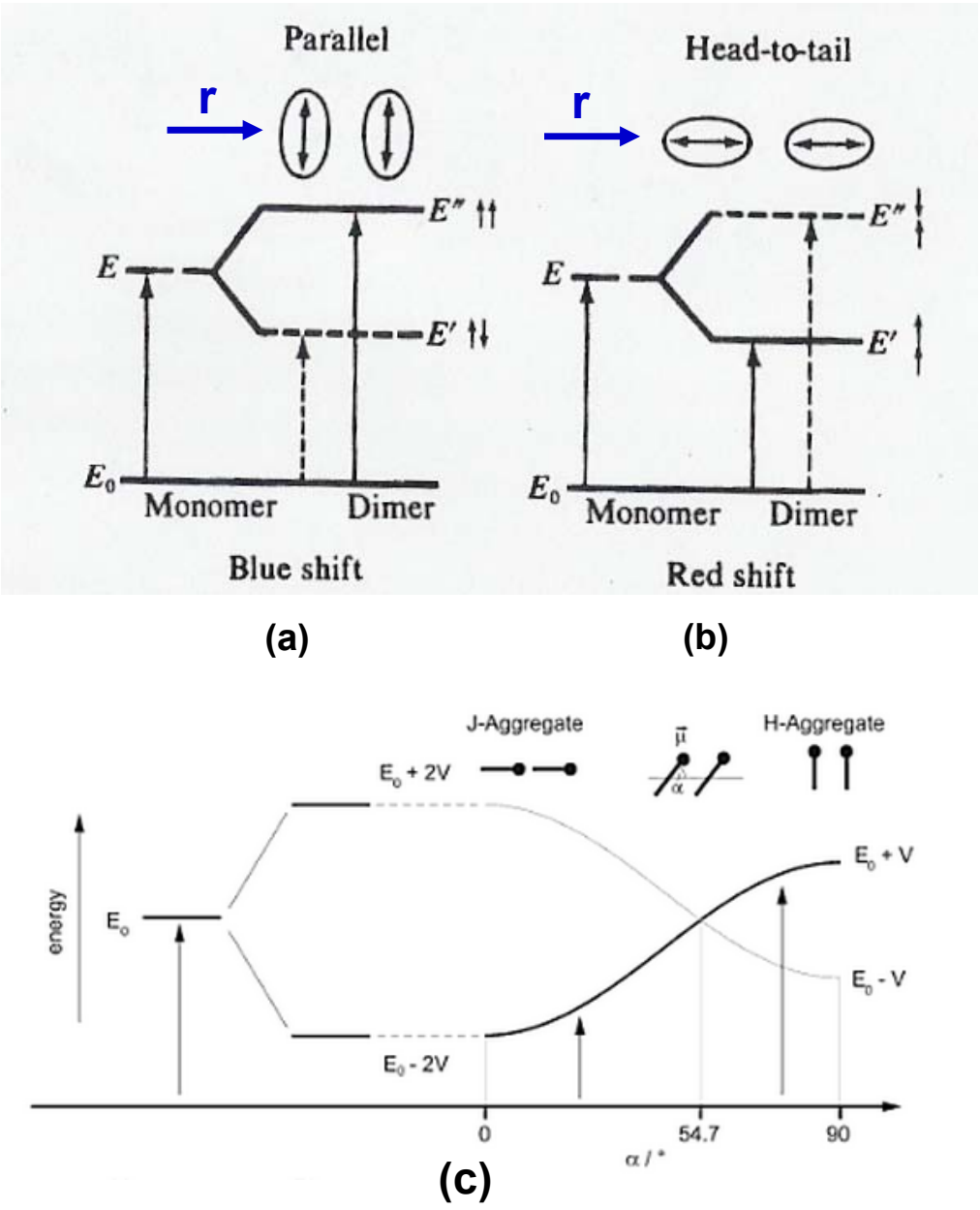

Figure 1.11 (a) Excited state energy level splitting of (a) a parallel or face-to-face arrangement of monomers (i.e., a J-aggregate), and (b) a collinear or head-to-tail arrangement of monomers (i.e., a H-aggregate). Vector "r" is the intermolecular packing axis. (c) shows the energy level splitting for intermediate cases, having orientation of angle α with respect to the packing axis. (a) and (b) are reproduced from [49], and (c) is reproduced from [53].

Now it is time to consider even larger aggregates – solid-state molecular crystals such as (crystalline) conjugated polymer films. Such solids are essentially discrete molecules held together by weak Van der Waals forces ("Van der Waals solids"), and the intermolecular coupling is much weaker than in metals or inorganic crystals. Thus, intermolecular coupling will be introduced as a perturbation of single molecule electronic structure. Furthermore, the strength of the intermolecular coupling relative to intramolecular couplings (electron-electron and electron-phonon) is weaker than in metals and inorganic crystals. Therefore, the effects of nuclear vibrations will be introduced into the description of the electronic structure, and electron exchange (i.e., singlet and triplet states) must be considered. These ideas are made more concrete by Figure 1.12,[54] which shows the evolution of electronic structure from an isolated molecule to a weakly-coupled (Van der Waals) solid. The molecule has (singlet) ground state S_0, and excited vibration states v_1, v_2, and v_3 in excited electronic state S_1; the combined electronic-vibrational levels are termed "vibronic" states. Upon condensing to form a solid, the electronic energy levels red-shift by the so-called "gas-to-crystal shift" energy, as the molecules aggregate and planarize. This can be considered an increase in effective conjugation length,[54] but is fundamentally due to second-order dispersion forces (i.e., Van der Waals forces).[55] If a unit cell of the solid contains more than one inequivalent molecule, it undergoes further energy splitting called Davydov splitting;[49] the P3HT films that will be analyzed here pack in a lamellar arrangement with a single molecule per unit cell, so Davydov splitting will not be present. Finally, the

intermolecular coupling removes the degeneracy of the excited levels of the isolated molecules and splits them into exciton bands of bandwidth W (where W is linked to the resonance integral by $W=4\beta$, the same relation as for the trimer discussed previously). The contradictory-sounding term "exciton band" is perhaps well suited for the final electronic structure picture on the right of Figure 1.12, as the overlapping energy levels consist of energy level splitting from both the vibronic structure of tightly-bound molecular (Frenkel) excitons as well as splitting from the intermolecular forces that forms the pseudo-band structure. In fact, the relative strength of the intramolecular forces compared to the intermolecular forces are borne out in the electronic structure – if the energy width of the exciton band, W, is small (i.e., weak intermolecular resonant coupling) compared to the energy width of the vibronic energy levels, then intramolecular forces dominate and the absorption and emission spectra will show vibronic structure characteristic of the individual molecules. Conversely, if the bandwidth W exceeds the vibronic energy level splitting, then the strong intermolecular coupling "washes out" the spectral signature from molecular vibrations.

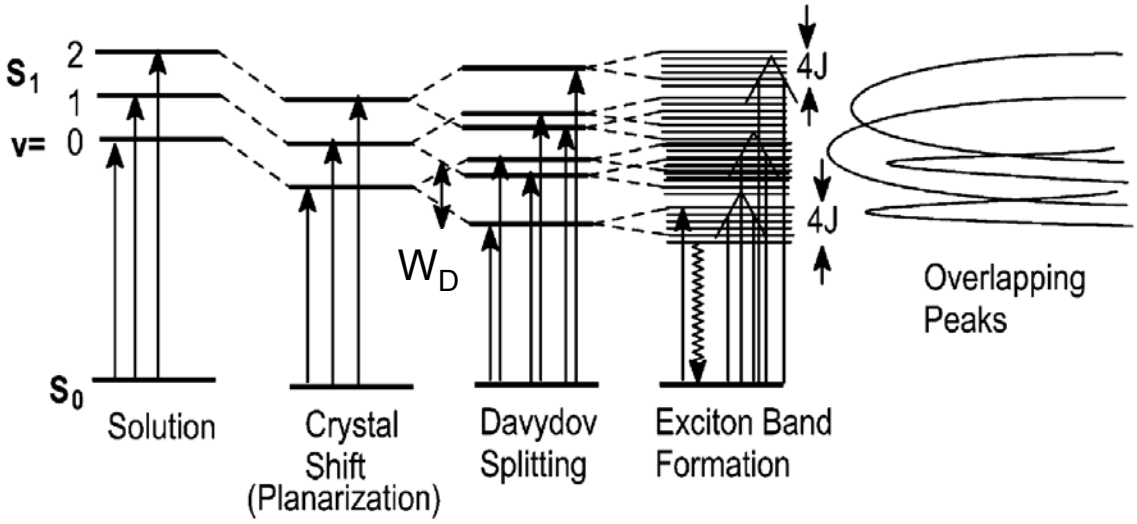

Figure 1.12 Energy level splitting of a vibronically-coupled isolated molecule as it condenses to form the solid phase. S_0 and S_1 are the ground and excited state electronic (singlet) energy levels, the v_i are the vibrational energy states within the first excited singlet state, W_D is the Davydvov splitting due to multiple molecules within the same unit cell, and J is the resonance integral that dictates the width of the exciton band splitting, where W=4J for aggregates of trimers or larger. The combination of energy level splittings due to vibronic and excitonic coupling give rise to the overlapping peaks in the optical spectra, as schematized on the right. Reproduced from [54].

The balance of excitonic and vibronic energies and their effects on the optical spectra of organic solids will become clearer with a concrete example – the electronic structure of poly(3-hexylthiophene). The most up-to-date quantum chemical calculations on P3HT have been largely performed by Spano,[55-57] and the experimental optical spectra presented in Chapters 3-4 are interpreted in the context of his research. The Hamiltonian employed by Spano is nearly identical to the well-known Hamiltonian used by Holstein[58] in his description of polaronic charge transport through molecular crystals. It includes linear electron-phonon (vibronic) coupling (normally neglected under the Born-Oppenheimer approximation) but

excludes electron-electron interactions (correlation and exchange). Hamiltonians of the Holstein type can be decomposed as follows:[49]

$$H = H_0 + H_1 + H_2 + H_3 + H_4 \tag{1.11}$$

where

$$H_0 = \sum_n \varepsilon a_n^\dagger a_n \tag{1.12}$$

$$H_1 = \sum_\lambda \hbar\omega_\lambda (b_\lambda^\dagger b_\lambda + \frac{1}{2}) \tag{1.13}$$

$$H_2 = \sum_n \sum_m J_{mn} a_n^\dagger a_n \tag{1.14}$$

$$H_3 = \sum_\lambda \sum_n g_{n\lambda}^2 \hbar\omega_\lambda a_n^\dagger a_n (b_\lambda + b_{-\lambda}^\dagger) \tag{1.15}$$

$$H_4 = \sum_n \delta\varepsilon_n a_n^\dagger a_n \tag{1.16}$$

A detailed understanding of the "second quantization" notation (creation and annihilation operators) is not necessary, but it is quite useful to understand what each term H_n represents. H_0 is simply the electronic energy at site n, with no coupling to the lattice. Similarly, H_1 is the uncoupled vibrational energy of the lattice. H_2 represented the excitonic coupling to nearest-neighbor molecules (where, again, J is analogous to the resonance integral β). H_3 is the electron-phonon interaction energy, scaled by dimensionless electron-phonon coupling constant(s) $g_{n\lambda}$ that represents an electron coupling to a phonon mode (vibration) of energy $h\omega_\lambda$. Finally, H_4 is the so-called "static diagonal disorder", representing variations in site-to-site energy caused by variations in composition and structure (i.e., disorder). The general idea of Spano's Hamiltonian describing the (excited state) electronic structure of P3HT should now become clear:[55]

$$H = \omega_0 \sum_n b_n^\dagger b_n + \omega_0 \lambda \sum_n (b_n^\dagger + b_n) |n\rangle\langle n| + \sum_m \sum_n (J_{mn} + \Delta_m \delta_{mn}) |n\rangle\langle n| + D + \omega_{0-0} + \lambda^2 \omega_0 \quad (1.17)$$

After accounting for minor changes in notation, a direct comparison of Equation 1.17 with Equations 1.11-1.16 should help define each term. To begin with, the electronic energy term (H_0) is neglected, as it is simply a constant value εN for an N-electron system and vanishes when $\varepsilon=0$ is chosen as the energy origin. The first term on the right hand site is the vibrational energy (cf. Equation 1.13). It is common, as is the case here, to consider one dominant vibrational mode. In polythiophenes, this mode is a collective breathing mode of coupled thiophene rings having an energy of ~0.18 eV. The second term on the right is the (linear) electron-phonon coupling interaction, representing electronic coupling to the ring-breathing mode with a strength given by coupling constant λ. The third term combines the effects of nearest-neighbor excitonic coupling with static diagonal disorder given by Δ_m; Spano essentially adds a random energy offset Δ_m to the electronic energy of site m, with the Δ_m's following a Gaussian distribution with standard deviation σ. There are two important corollaries. First, it should be emphasized that the intermolecular excitonic coupling J_{mn} is between π-stacked polymer chains (i.e., each polymer chain is one "molecule"). This is illustrated in Figure 1.13a, where each horizontal dark line is a polymer chain (conjugation axis out of the plane of the paper), and the coupling is between the chains in the b-axis (π-stacking axis). Second, intramolecular effects (i.e., intrachain effects) are "coarse-grained" out of Spano's model, but indirectly manifest themselves through the disorder parameter σ. For

example, disruptions of intrachain conjugation due to torsion or oxidative defects manifest themselves in an increase of parameter σ. Returning to Equation 1.17, D is simply the dispersion (Van der Waals) energy of the coalescing solid, and $\omega_{0\text{-}0}$ is the electronic transition energy in the gas phase. Finally, $\lambda^2\omega_0$ is the nuclear relaxation energy (or reorganization energy) of the molecule upon electronic excitation. λ^2, also known as the Huang-Rhys factor, is proportional to the strength of the electron-phonon coupling, and will be described at length in the next section. For now, it should be noted that λ^2 has a numerical value of unity for polythiophenes.[55] The electronic structure of P3HT is shown schematically in Figure 1.13b. The ground state and first two excited states (or exciton bands) are shown. The structure is very similar to the general case shown in Figure 1.12 with level splitting due to both vibronic interactions and excitonic coupling. Here, in the case of P3HT, the vibronic energy spacing ω_0 is drawn wider than the effective excitonic bandwidth W_{eff}, which, in the case of vibronic coupling, is given by:[57]

$$W_{eff} = W\lambda^{2\nu}e^{-\lambda^2}/\nu! \tag{1.18}$$

Here, W is the free exciton bandwidth (W=4J) and v is the index of the vibronic state. Though W varies as a function of polymer structure, a reasonable estimate for W for P3HT films is 0.1 eV. Plugging this into Equation 1.18 for the widest excited band S_1v_0 yields a W_{eff} value of $0.1/e \approx 0.037$ eV. Comparing this to the magnitude of the electron-phonon coupling, $\lambda^2\omega_0 \approx 0.18$ eV, it is easy to see that the sketch in Figure 1.13b is justified, and that the electronic structure of P3HT indeed lies in the realm of strong electron-phonon coupling and weak excitonic coupling.

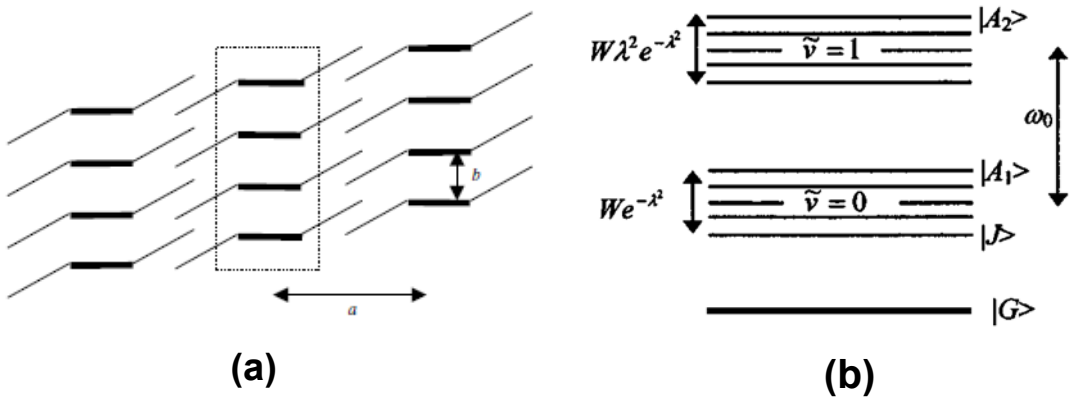

Figure 1.13 (a) Model of molecular packing in P3HT used to calculate its electronic structure. Each bold horizontal line is an individual polymer chain, with its axis of conjugation extending into the page and its alkyl side chains (diagonal lines) extending in the direction of the alkyl packing axis "a". The intermolecular coupling is only due to interactions along the π-stacking or "b" axis. Reproduced from [56]. (b) Electronic structure of P3HT. |G> is the ground state, v=0 and v=1 represent vibrational (vibronic) states within the first excited electronic state. |A> and |J> represent substates at the top and bottom of each exciton band, respectively. ω_0 is the vibrational energy of the dominant vibrational mode in P3HT (the ring-breathing mode), and the width of the exciton bands are given by Equation 1.18. Reproduced from [55].

Before proceeding to discuss the optical processes in conjugated polymers, a few final points should be made regarding electronic structure. Even though electron-phonon coupling manifests itself in the electronic structure, and in the next section will be shown to strongly affect the optical properties, it gives rise to many more interesting physical phenomena in conjugated polymers. For example, it allows for the Peierls transition in polyacetylene, whereby lattice vibration opens up a mid-gap electronic state (the solid-state analogue of the Jahn-Teller effect); it is responsible for bond-alternation defects called solitons that are analogous to domain walls in ferromagnets;[51] and it associates a local lattice distortion with each excited electron or free charge. It is the last effect that is most relevant for the materials studied here,

and the coupling of the excited particle with its surrounding distortion is termed a polaron. Because of the strong electron-phonon coupling in P3HT, excitons may be more accurately termed "polaron excitons", and electron-hole pairs may be called "polaron pairs"; both of these terms are often used in the literature. Finally, electron-electron effects, though sizeable in conjugated polymers, will not be discussed in detail here. However, it should be noted that strong electron-electron coupling (due to weak electronic screening in such low-ε materials) lead to large singlet-triplet exchange energies (i.e., the excited state triplet T_1 is usually much red-shifted with respect to the excited state singlet S_1). Furthermore, this large singlet-triplet splitting, combined with the fact than spin-orbit coupling is weak (organics are intrinsically low-Z materials) means that spin is conserved during electronic transitions. But this is more the language of optical spectroscopy, which leads to the next section.

1.6 Electro-Optical Processes in Organic Photovoltaic Materials

1.6.1 Absorption and Emission

The purpose of this subsection is to lay the theoretical groundwork to understand the general features of absorbance and luminescence in conjugated polymers, as well as the peculiar optical spectroscopic features of P3HT. A key theme, again, is vibronic coupling. In the previous section, it was shown how vibronic coupling leads to vibronic sublevels in the manifold of excited states. Now the theoretical description of the electronic structure of the molecule must be combined with a

theoretical description of the electromagnetic field that couples to the molecule. This is exactly what has been done by Spano,[55-57] but the calculations are so complex that it is difficult for the uninitiated to comprehend the mathematical gear-turning that leads from the initial Hamiltonian to the final calculated spectra. Therefore, before discussing the absorption and emission spectra of P3HT, a simple model of absorption and emission in a vibronically-coupled generic molecule will be presented to illustrate the salient features of the optical spectrum and to illuminate the basic mathematics involved. Interestingly, it will be shown how even a system described by a simplified (Born-Oppenheimer) Hamiltonian that lacks explicit vibronic coupling can still lead to a vibronic optical spectrum.

This simplified description of vibronic optical transitions borrows five important approximations, and the order in which they appear in the derivation leads to the final result. They are (1) the Born-Oppenheimer Approximation; (2) Fermi's Golden Rule (first order perturbation approximation); (3) the semiclassical approximation (treating the photon flux as a classical time-varying EM field but the molecule quantum-mechanically); (4) the dipole or "long-wavelength" approximation; and (5) the Franck-Condon principle. To begin with, the Hamiltonian for an arbitrary molecule is comprised of the kinetic energies of the nuclei and electrons, and the potential energies of Coulombically-interacting nucleus-nucleus, electron-electron, and electron-nucleus pairs:

$$H = T_N + T_e + V_{NN} + V_{ee} + V_{eN} \tag{1.19}$$

Because the electrons are ~1000 times lighter than the nuclei, they respond nearly instantly to nuclear motion. This difference in timescales motivates the factorization of the time-independent molecular wavefunction into an electronic part φ and a nuclear part χ:

$$\Psi(r,R) = \phi(r;R)\chi(R) \tag{1.20}$$

This is the Born-Oppenheimer approximation. Here, the electronic wave function φ depends parametrically on nuclear coordinate R. The factorization of the wavefunction enables the time-independent Schrödinger equation to be likewise factored into electronic and nuclear equations:

$$(T_e + V_{eN} + V_{ee})\phi(r;R) = E_{el}(R)\phi(r;R) \tag{1.21}$$

$$(T_N + V_{NN} + E_{el})\chi(R) = E_{nuc}\chi(R) \tag{1.22}$$

It is important to note the absence of the T_N term in Equation 1.21 – the electronic wavefunction has no dependence on nuclear motion under the Born-Oppenheimer approximation (in contrast to the Holstein Hamiltonian shown previously). The electronic Schrödinger equation, Equation 1.21, is used to compute the electronic potential energy surfaces $E_{el}(R)$. Such surfaces are shown pictorially in Figure 1.14 where they are assumed to be harmonic and one-dimensional. The vibrational wavefunctions sketched inside the potential energy wells can be calculated using Equation 1.22. However, because the potential energy surface can always be approximated as harmonic, the vibrational wavefunctions can be taken to be the solutions of the quantum harmonic oscillator;[59] these will manifest themselves in the

shape of the absorption and emission envelopes sketched on the right side of Figure 1.14.

Now it is time to consider the interaction of a beam of light perturbing the molecule from an initial state to a final state (e.g., from the ground state to the first excited state in the case of absorption). This fundamentally involves the solution of the time-dependent Schrödinger equation for the molecule and the light beam. Fortunately, as long as the light beam is not too strong (i.e., a weak perturbation) the transition rate can be accurately calculated using a first-order perturbation approximation known as Fermi's Golden Rule:

$$R_{I\to F} = \frac{2\pi}{\hbar}\left\langle I\left|V\right|F\right\rangle^2 \delta(E_F - E_I) \tag{1.23}$$

Here, I is the initial state of the molecule, F the final state, V is the perturbation caused by the interacting light beam, and δ is the Dirac delta function. If the light beam is described classically and its wavelength is much larger than the molecular dimensions (approximations 3 and 4), then the transition rate can be rewritten as:

$$R_{I\to F} = \frac{2\pi}{\hbar}\left\langle I\left|\mu\right|F\right\rangle^2 \delta(E_F - E_I) \tag{1.24}$$

where μ is the electric dipole operator. Inserting the Born-Oppenheimer wavefunctions, and suppressing the delta function (which, in practice, simply acts as a line shape function):

$$R_{I\to F} \propto \left\langle \phi_i(r;R)\chi_i(R)\left|\mu(r)\right|\phi_f(r;R)\chi_f(R)\right\rangle^2 \tag{1.25}$$

$$R_{I\to F} \propto \left\langle \chi_i(R)\left|M_{if}(R)\right|\chi_f(R)\right\rangle^2 \tag{1.26}$$

where

$$M_{if}(R) = \langle \phi_i(r;R) | \mu(r) | \phi_f(r;R) \rangle \tag{1.27}$$

is the transition dipole moment. Because the electronic wavefunctions are slowly-varying functions of nuclear coordinate R (Born-Oppenheimer approximation), it can be argued that the transition dipole $M_{if}(R)$ is also a slowly-varying function of R.[60] Therefore, M can be Taylor expanded around an arbitrary fixed nuclear coordinate R_0:

$$M_{if}(R) \approx M_{if}(R_0) + \left.\frac{\partial M_{if}}{\partial R}\right|_{R=R_0} (R - R_0) + \ldots \tag{1.28}$$

If only the constant term from the expansion of M_{if} is kept, M_{if} is no longer a function of the nuclear coordinates; this is the Franck-Condon approximation, and leads to a factoring of the transition rate expression:

$$R_{I \to F} \propto M_{if}^2(R_0) \langle \chi_i(R) | \chi_f(R) \rangle^2 \tag{1.29}$$

Equation 1.29 says that Franck-Condon transitions are "vertical" (at fixed nuclear coordinate R_0 – the line AB in Figure 1.14), and that the oscillator strength of the electronic transition given by M_{if}^2 is redistributed according to the square of the vibrational wave function overlap integral $\langle \chi_i(R) | \chi_f(R) \rangle^2$, the so-called Franck-Condon factor. This leads to optical spectra composed of a series of vibronic "bands", as shown in Figure 1.14. The precise weighting of the vibronic bands requires mathematical evaluation of the Franck-Condon factors.

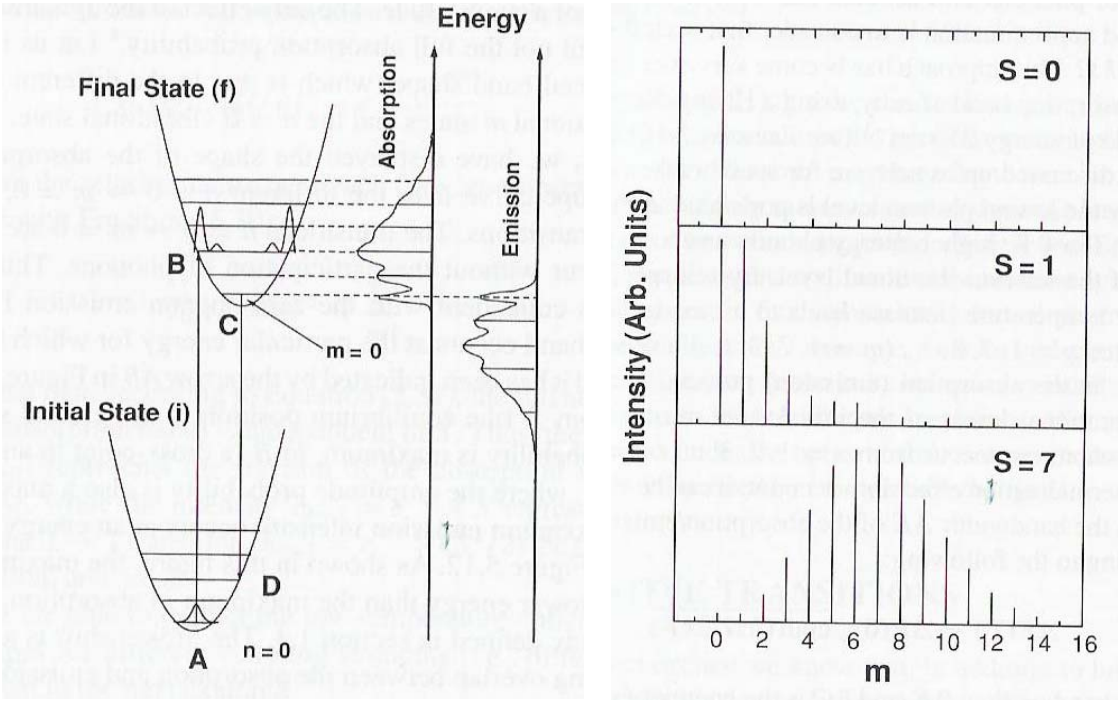

Figure 1.14 (a) Ground and excited state potential wells for a vibronically-coupled system (non-zero Stokes shift). The vibrational states within the ground electronic state are labeled n_i and those within the excited state are labeled m_j. Franck-Condon vertical transitions are shown for absorption (line AB) and luminescence (line CD). Transitions from vibrational states i≠j give rise to the sidebands shown in the generic absorption and emission spectra on the right. (b) Relative weighting of absorbance peaks arising from Franck-Condon transitions from n=0 → m, according to Equation 1.39, for several values of the Huang-Rhys factor (c.f. Equation 1.34). Both reproduced from [63].

The harmonic oscillator wavefunctions are the product of Gaussian functions and Hermite polynomials,[59]

$$\chi_n(R) = (\frac{\alpha}{\pi})^{1/4} \frac{1}{2^n n!} H_n(R) e^{-R^2/2} \tag{1.30}$$

where

$$\alpha = \frac{m\omega}{\hbar} \tag{1.31}$$

and H_n are Hermite polynomials of order n. It is instructive to evaluate the first several Franck-Condon integrals:

$$\langle \chi_0(R) | \chi_0(R) \rangle = (\frac{\alpha}{\pi})^{1/2} \int_{-\infty}^{\infty} e^{-(R-R_0)^2/2} e^{-(R-Q_0)^2/2} dR = e^{-\alpha(R_0-Q_0)^2/4} \quad (1.32)$$

$$\langle \chi_0(R) | \chi_1(R) \rangle = (\frac{\alpha}{\pi})^{1/2} \int_{-\infty}^{\infty} e^{-(R-R_0)^2/2} e^{-(R-Q_0)^2/2} 2RdR = \frac{\sqrt{\alpha}}{\sqrt{2}} (R_0 - Q_0) e^{-\alpha(R_0-Q_0)^2/4} \quad (1.33)$$

R_0 is the equilibrium position of the ground-state potential well (see Figure 1.14) and Q_0 is the equilibrium position of the excited state potential well. *The introduction of the possibility of different equilibrium geometries R_0 and Q_0 is key* – this is where vibronic coupling enters this model. If R_0=Q_0, it is trivial to see that the 0-1 Franck-Condon integral is zero, and it will be shortly shown that this would be true for all transitions except for the 0-0 transition. Therefore, it is only when $R_0 \neq Q_0$ that oscillator strength is distributed away from the 0-0 transition and vibronic structure arises in the optical spectra. In fact, displacement of the excited state potential well with respect to the ground state potential well is an example of linear electron-phonon coupling;[61] its introduction here in produces the same end result as the introduction of a linear electron-phonon coupling term in the initial Hamiltonian (such as the Holstein Hamiltonian shown previously). The displacement (R_0-Q_0) is a fundamental quantity that can be associated with a dimensionless energy S:

$$S = \frac{\alpha}{2}(R_0 - Q_0)^2 = \frac{\lambda}{\hbar\omega} \quad (1.34)$$

S is known as the Huang-Rhys factor, first derived by Huang in 1950 during his study of the coupling of F-center electronic transitions to lattice modes.[62] From Figure 1.14a it can be seen that the Huang-Rhys factor is the (dimensionless)

relaxation or reorganization energy that is proportional to the square of the potential well displacement (and is proportional to the square of the linear electron-phonon coupling constant[60]). In terms of the Huang-Rhys factor, Equations 1.31 and 1.32 become:

$$\langle \chi_0(R) | \chi_0(R) \rangle = e^{-S/2} \tag{1.35}$$

$$\langle \chi_0(R) | \chi_1(R) \rangle = \sqrt{S} e^{-S/2} \tag{1.36}$$

and, squaring them to get the Franck-Condon factors:

$$\langle \chi_0(R) | \chi_0(R) \rangle^2 = e^{-S} \tag{1.37}$$

$$\langle \chi_0(R) | \chi_1(R) \rangle^2 = S e^{-S} \tag{1.38}$$

At the limit of T=0K, only the ground vibrational states are occupied, and it can be shown that the transition intensity from the 0^{th} to the m^{th} vibrational state is:[63]

$$I_{0 \to m} = e^{-S} \frac{S^m}{m!} \tag{1.39}$$

Thus, the distribution of oscillator strength in a vibronic transition follows a Poisson distribution, where the Poisson parameter is the Huang-Rhys factor. (At finite temperature when the occupation of the vibrational states is described by a Boltzmann distribution, the intensity profile follows a Laguerre distribution,[61] but here only the zero temperature limit will be considered). When there is no displacement of potential wells, all oscillator strength is contained in the 0-0 transition (Figure 1.14b, top panel); as the displacement (vibronic coupling) increases, oscillator strength will be shifted to higher vibrational modes, taking a Gaussian form centered on mode m=S (Figure 1.14b, bottom panel). For all S>0, the emission spectrum will be red-shifted from the absorption spectrum; this is called the

Stokes shift and its magnitude is governed by the Huang-Rhys parameter S. Thus, the magnitude of the Stokes shift in the optical spectra is proportional to the amount of vibronic coupling in the molecule. Finally, irrespective of the value of S, the absorption and emission profiles exhibit mirror symmetry, as sketched in Figure 1.14a.

Several comments should be made regarding the universality of the above treatment. First, the picture of the two coupled potential wells in Figure 1.14 need not only apply to optical excitations – with simply a smaller energy gap between the two wells, the diagram is analogous to that used to describe electron transfer in a two-site system, and the relaxation energy λ is equivalent to the "reorganization energy" in Marcus electron transfer theory. Moreover, Equation 1.29 resembles a general rate equation describing a two-level electron system linearly coupled to a vibrational mode (a "spin-boson" system).[60] A linearly coupled vibrational system will always contain the Franck-Condon factors, but the form of "M_{if}" becomes more general – the transition dipole moment becomes an electronic tunneling term in electron transfer theory, or the spin-orbit operator for intersystem crossing, and so on.[60]

The interpretation of the optical emission spectra of P3HT combines the ideas from Franck-Condon transitions with the rules of H- and J-aggregate emission. Basically, the Franck-Condon progression P3HT is distorted away from its Poissonian form in proportion to the magnitude of its H-like aggregation (recall the face-to-face packing structure of P3HT shown in Figure 1.13a). The majority of the

distortion is encompassed by the first two vibronic peaks in both the absorbance and luminescence spectra. From measurements of the photoluminescence of dilute P3HT in solution, the Huang-Rhys factor is ~1; therefore, the vibronic intensity distribution of unaggregated P3HT should resembled the middle panel of Figure 1.14b for both absorbance and luminescence. The presence of H-aggregation, however, means that R_{abs}, the ratio the 0-0 to 0-1 vibronic peaks in absorption, will decrease from its isolated molecule value with increasing excitonic coupling.[64] This may be made more tangible with the following model of the absorbance spectrum of P3HT:[65]

$$A = \sum_{m=0}\left(\frac{e^{-s}s^{m}}{m!}\right)\left(1-\frac{We^{-s}}{2E_{p}}\left(\sum_{n\neq m}\frac{s^{n}}{n!(n-m)}\right)\right)^{2}\exp\left[\frac{-(\hbar\omega-E_{00}-mE_{p})^{2}}{2\sigma^{2}}\right] \qquad (1.40)$$

In Equation 1.40, it is seen that the Gaussian lineshapes of each vibronic transition m are modulated by the single-molecule Poisson distribution (first factor under the summation) as well as an H-aggregate correction scaled by W; as W→0, the absorbance spectrum will revert to its isolated molecule Poissonian form. Figure 1.15a shows a fit of Equation 1.40 to an experimental absorbance spectrum of P3HT with W~0.150 eV (it should be noted that Equation 1.40 only represents the low-energy aggregated region of the total absorbance envelope).[65] The relationship between the interchain excitonic coupling and the intrachain conjugation length is essential to drawing conclusions from P3HT absorption spectra. Quantum chemical calculations show that the exciton bandwidth W is inversely proportional to the

intrachain conjugation length.[66] Therefore, absorbance measurements of P3HT films can quantify the intrachain order. Absorbance measurements have been used to correlate the mobility of P3HT with the conjugation length in P3HT films cast from different solvents,[65] and will be used here (Chapter 4) to quantify the intrachain ordering during thermal annealing under different oxidative environments.

The photoluminescence (or luminescence or fluorescence or emission– these terms will be used interchangeably) spectrum of P3HT reveals similar clues regarding order/disorder in solid films. In non-vibronically coupled H-aggregates, emission is dipole forbidden and nearly undetectable. Fortunately, for vibronically-coupled systems like P3HT, only the 0-0 transition is dipole forbidden, so the photoluminescence spectrum of P3HT (a) exists and (b) can be used as a diagnostic of the ordering of solid films. In a perfectly ordered P3HT (H)-aggregate, the forbidden 0-0 transition leads to a photoluminescence spectrum like the schematic shown in Figure 1.15b. If the perfect H-aggregate electronic coupling is broken (e.g., from packing defects, from conjugation loss due to oxidation), then the 0-0 transition becomes optically allowed. Thus the ratio R_{em} is a metric of disorder in P3HT films. This ratio will be used in Chapters 2 and 4 to study the disordering of P3HT films caused by PCBM infiltration and photo-oxidation, respectively. Several final details should be pointed out. In contrast to the unique sensitivity of disorder of the 0-0 transition, higher order vibronic transitions have no special aggregate selection rules controlling their emission intensity, and thus retain their Poissonian form regardless of the amount of ordering.[57] The intensity ratio can be accurately

estimated by comparison of peak heights in the optical spectra as long as the spectral peaks are well-resolved with similar linewidths (i.e., fitting and integrating each peak is not required).

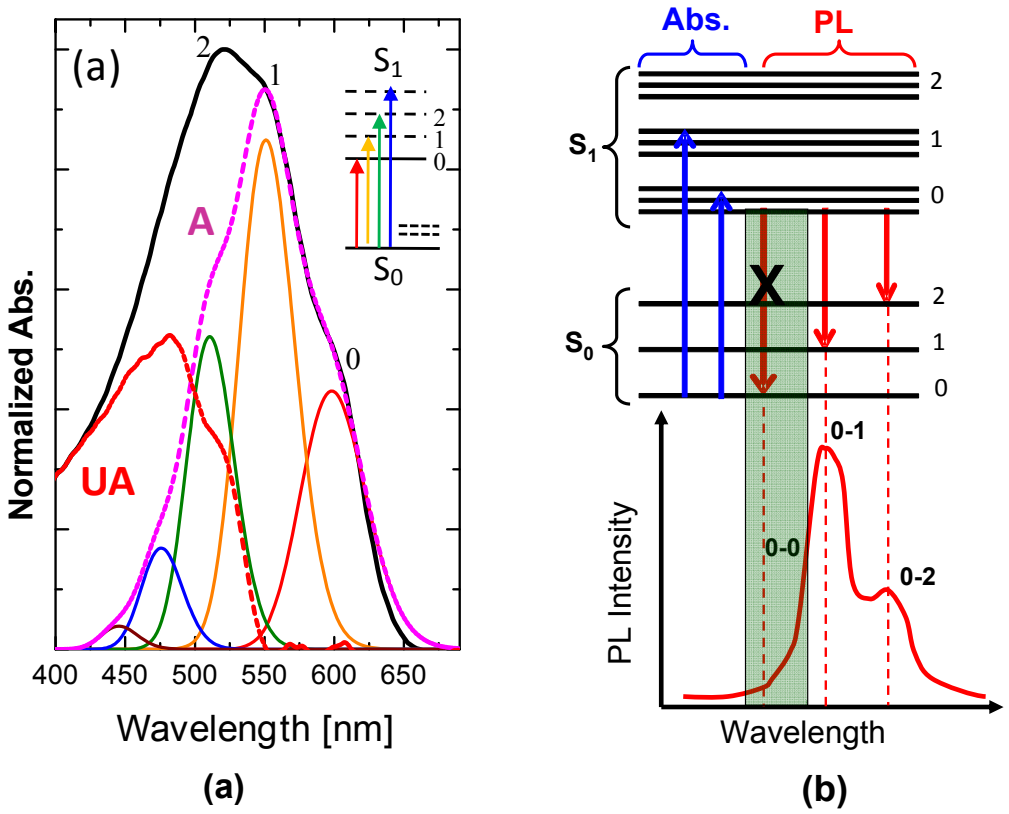

Figure 1.15 (a) Experimental absorbance spectrum of P3HT (black curve) with fit given by Equation 1.40 (for aggregated P3HT, "A", the pink envelope which is the superposition of the colored Gaussians). The red "UA" curve represents absorbance due to isolated chains that are not included in the model given by Equation 1.40. (b) Schematic of photoluminescence (PL) in P3HT, illustrating the forbidden 0-0 transition for perfectly-ordered P3HT aggregates.

However, the peaks are only well-resolved, as sketched in Figure 1.14b, at low temperature (T→0K). At room temperature, several broadening effects contribute to the smearing-together of the vibronic sidebands. A comparison of the room temperature photoluminescence spectrum of P3HT and the low temperature (~13 K)

spectrum is shown in Figure 1.16 (dashed and solid curves, respectively). The much broader vibronic peaks in the room temperature spectrum are due partly to enhanced electron-phonon scattering at higher temperatures – the higher scattering rate leads to a shorter excited state lifetime and consequently a wider spectral peak (lifetime broadening). The enhanced rate of phonon interactions also manifests itself in the magnitude of the photoluminescence envelope itself. Although it is not evident from the normalized spectra in Figure 1.16, the absolute intensity of the room temperature spectrum is approximately a factor of two lower than the low-T spectrum, due to the enhanced nonradiative deactivation pathway at room temperature. The room temperature broadening is also due to thermally-activated emission above the band bottom (previously, our considerations of the optical selection rules had been based on the limit of T=0 K). Finite temperature entails that the luminescence also initiates from states above the exciton band bottom, populated according to the Boltzmann distribution; this results in a form of heterogeneous broadening. The Boltzmann population of excited states also loosens the 0-0 selection rule (because now not all luminescence originates from the band bottom), leading to the increase in the 0-0/0-1 peak ratio R_{em} at room temperature.[67] As a side note, it is also evident from Figure 1.16 that the room temperature photoluminescence spectrum is slightly blue-shifted with respect to the low temperature spectrum. This can be rationalized by the expansion of the lattice at room temperature, and the concomitant decrease in intermolecular dispersion interactions (D) at greater intermolecular distances.[57]

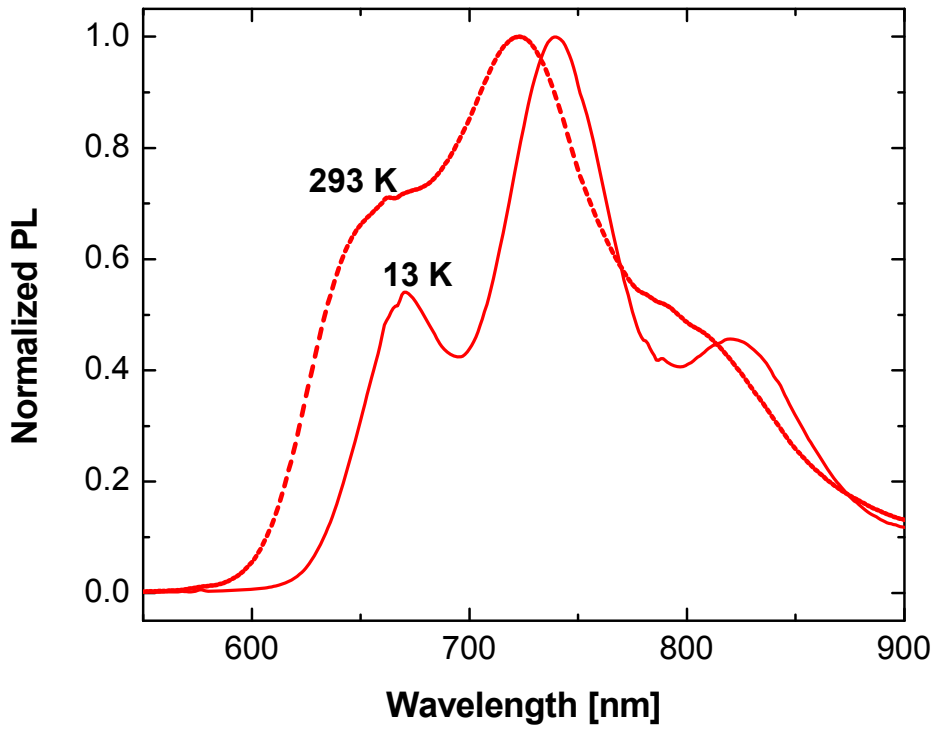

Figure 1.16 Experimental P3HT photoluminescence spectra at room temperature (293K, dotted curve) and low temperature (13K, solid curve).

1.6.2 Raman Scattering

So far, the discussion of optical transitions has dealt with vibronic transitions and their link to order vs. disorder in P3HT films. It is also possible to gain structural information about P3HT (and other conjugated polymers) by probing the pure vibrational transitions of the molecule. There are two main ways by which to experimentally obtain the vibrational spectrum of a given molecule – infrared absorption and Raman scattering. Infrared absorption involves the direct absorption of a photon to stimulate a transition between vibrational states; this scheme is

sketched in Figure 1.17. This requires excitation energy resonant with molecular vibrations (~0.1 eV) and, in practice, usually involves a transmission measurement with an IR light source. On the other hand, a (Stokes) Raman scattering experiment (Figure 1.17) accesses the vibrational transition by exciting the ground state to an intermediate or "virtual" state, and measuring the Stokes-shifted radiation emitted upon the transition from the virtual state to the final state. This grants several experimental advantages: the fact that Raman scattering is non-resonant permits the use of laser sources of arbitrary frequency, and, for solids, the experiment can be performed in a reflection-based geometry (negating any interference from a highly absorptive substrate). Of course, there are other differences between IR and Raman scattering, and the choice of one over the other will depend upon the molecule in question or even vibrational modes of the molecule. In this work, IR spectroscopy is used to measure the change in intensity of various aliphatic, olefinic, hydroxyl and carbonyl modes of P3HT to study degradation kinetics. At the same time, the Raman spectrum of P3HT is used to track changes in chain conformation and conjugation in its interactions with PCBM, and the Raman signature of MDMO-PPV, collected in a confocal microscope, is used for the high-resolution detection of MDMO-PPV domains in organic solar cell blends. In particular, one specific Raman-active mode dominates the spectra of conjugated polymer thin films, so a brief background on Raman scattering and its specificity to conjugated polymers will now be presented.

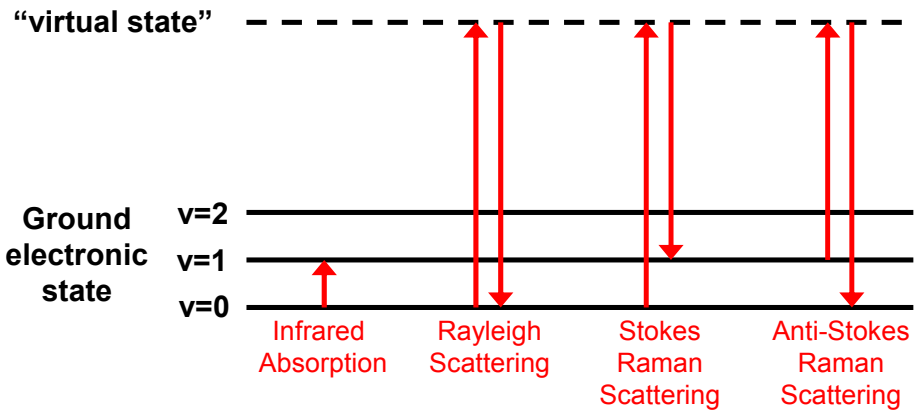

Figure 1.17 Resonant and non-resonant vibrational processes depicted in an energy level scheme. The v_i are different vibrational states within the ground electronic state.

The Raman effect[68] is the scattering of light from an induced dipole moment in a molecule. Whereas infrared absorption involves the interaction of the electromagnetic field with the dipole moment of the molecule (and thus only molecules with permanent dipole moments are IR-active), Raman scattering occurs from any molecule whose polarizability is changed (i.e., its electron cloud perturbed) by the incident radiation. The Raman effect can be well-explained by a simple classical analysis. It is based on the premise that the molecular polarizability α varies harmonically with the resonant frequency v_0 of the bond in question:

$$\alpha = \alpha_0 + (\Delta\alpha)\cos[2\pi v_0 t] \qquad (1.41)$$

where α_0 is the polarizability at the equilibrium bond length, and $\Delta\alpha$ is the maximum variation in polarizability during the vibration. If the incoming radiation is modeled

the usual way as a harmonically-varying electromagnetic field, the electric field is given by:

$$E = E_0 \cos[2\pi\nu t] \tag{1.42}$$

then the induced dipole moment in the molecule is the product of a harmonically-varying polarizabilty and a harmonically-varying electric field:

$$\mu_{ind} = \alpha E = (\alpha_0 + (\Delta\alpha)\cos[2\pi\nu_0 t])E_0 \cos[2\pi\nu t] \tag{1.43}$$

After applying a trigonometric identity, it is seen that the induced dipole moment consists of three terms:

$$\mu_{ind} = \alpha_0 E_0 \cos[2\pi\nu t] + \frac{1}{2}\Delta\alpha E_0(\cos[2\pi(\nu - \nu_0)t]) + \cos[2\pi(\nu + \nu_0 t]) \tag{1.44}$$

The term at the excitation frequency ν represents Rayleigh scattering, the (ν-ν_0) term represents Stokes Raman scattering, and the (ν+ν_0) term represents anti-Stokes Raman scattering. The three processes are schematized in Figure 1.17. The nature of the "virtual state" introduced in this figure is not immediately obvious, and arises from the mathematics of a quantum mechanical perturbation treatment of Raman scattering[69] that is beyond the scope of this section; for the present purpose, it is best viewed as a tool for illustrating an inherently nonresonant optical process (scattering) alongside a resonant optical process (absorption). The intensity of each type of scattered light follows the dipole radiation law from classical electromagnetics:

$$I = \frac{16\pi^4\nu^4}{3c^3}\mu^2 \tag{1.45}$$

Though the intensity of both Rayleigh and Raman scattering scales with the fourth power of the radiation frequency, Rayleigh scattering is the dominant process no

matter what the frequency – about 10^7 photons are Rayleigh-scattered for every Raman-scattered photon. Rayleigh scattering, however, reveals nothing about the vibrational structure of the molecule (see Figure 1.17), and it is the Raman scattering that should be detected (in particular the Stokes Raman signal, stronger than the anti-Stokes signal according to the Boltzmann distribution at the given temperature). Before going on to highlight Raman scattering in P3HT, brief pause should be made to emphasize the role of vibronic coupling in the Raman scattering process. The Raman scattering experiment, which involves (typically) optical frequencies that are not resonant with vibrational frequencies, only is possible through the coupling of the electron cloud to the nuclei. To quote Long,[69] "Raman scattering arises from the electric dipoles oscillating at $(\omega_1 \pm \omega_k)$, which are produced when the electric dipole oscillating at ω_1 is modulated by the molecule oscillating at frequency ω_k. The necessary coupling between the nuclear motions and the electric field is provided by the electrons whose rearrangement with nuclear motion impose a harmonic variation on the polarizability."

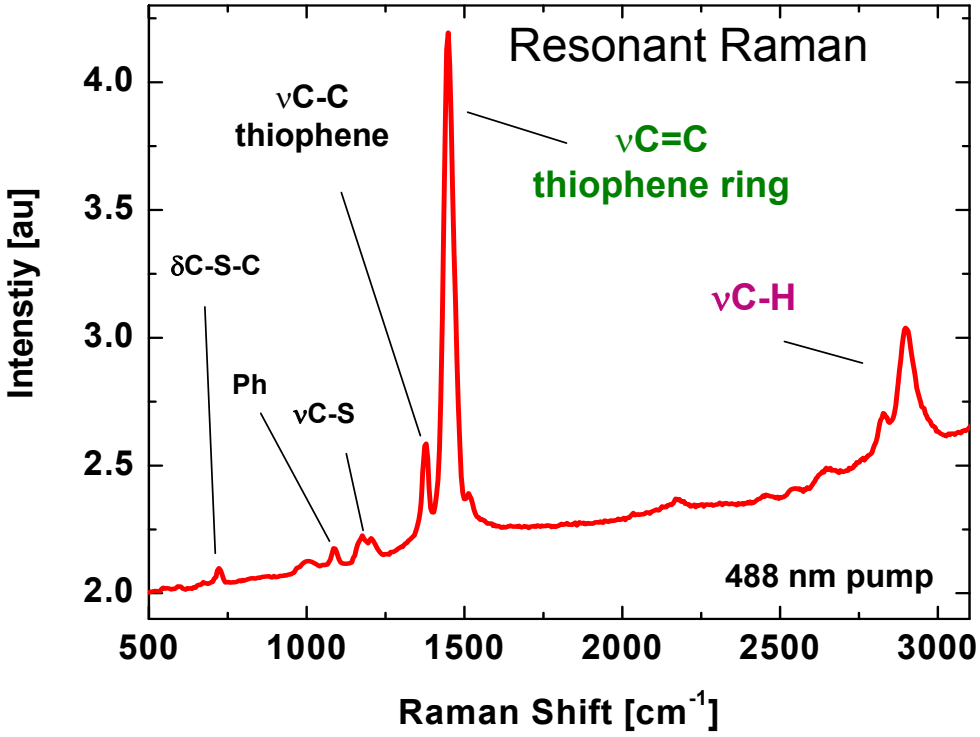

Figure 1.18 Experimental Raman spectrum of a P3HT thin film. Excitation performed with the 488 nm line of an Argon ion laser (resonant Raman, c.f. Figure 1.15). The ring-breathing mode (νC=C "thiophene ring") dominates the spectrum, though several additional modes may be identified.

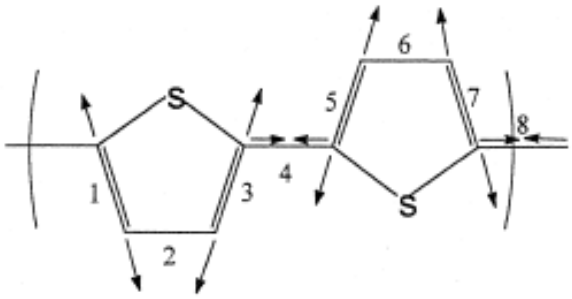

Figure 1.19 Illustration of the dominant ring-breathing vibrational mode in P3HT. This mode involves the collective, simultaneous symmetric stretching of C=C and C-C bonds as shown by the arrows. Reproduced from [73].

The Raman spectra of polymers like MDMO-PPV and P3HT have characteristics unique to conjugated systems. First is the relative dearth of experimentally observed Raman modes despite the immense size of these molecules (M_w~10^5-10^6 Da) and corresponding number of normal modes (>1000). For example, the Raman spectrum of a P3HT thin film shown in Figure 1.18 contains only ~5 distinguishable peaks. All of these are related to various vibrational modes originating on the thiophene repeat unit. Furthermore, the scattering cross-sections of conjugated polymers are much higher when compared with those of σ-bonded compounds.[70] At first glance, the high scattering intensities of conjugated polymers might be attributed to resonant enhancement upon excitation with pump sources within the absorption envelope (as is the case with the 488 nm excitation of P3HT in Figure 1.18). However, conjugated molecules still show abnormally high Raman intensities even when excited with lasers outside of the HOMO-LUMO gap. Several theories have been proposed to explain the uniquely enhanced Raman signatures in conjugated polymers;[70-72] here, we will invoke the Effective Conjugation Coordinate (ECC) model put forward by Zerbi and coworkers.[70,73-74] A thorough description of the ECC model would require a quite involved mathematical exposition, so only a brief discussion of the premises and implications will be presented here. Basically, it can be shown that a pseudo-resonant enhancement occurs for Raman modes whose normal coordinate is along the direction which electron-phonon coupling is most effective.[70] Another way of saying this is that the enhanced Raman mode is along the direction in which the potential energy in the excited state is displaced with

respect to the ground-state minimum. Such an abstract description may be made more tangible by considering the enhanced Raman mode in P3HT, shown in Figure 1.19. This complex mode is essentially a superposition of breathing modes of adjacent thiophene monomers, and will hereafter be referred to as the ring-breathing mode. As can be seen from this figure, the ring-breathing mode is symmetric along the axis of conjugation (and correspondingly along the axis of displacement of ground and excited state potential wells, as the normal coordinate in Figure 1.14 is taken to be this intramolecular vibration by Spano).[57] It has been shown both experimentally and through calculations that such modes are sensitive to the conjugation length – larger conjugation lengths soften the effective force constant and thus lower the vibrational frequency, and shorter conjugation lengths lead to higher vibrational frequencies. The high enhancement factor of the ring-breathing mode, plus its unique sensitivity to conjugation length, suggests that measuring the shift of the Raman shift of this mode is an excellent probe of intramolecular order (via the conjugation length) in conjugated polymers.

1.6.3 Excited State Processes in Organic Solar Cells

Thus far, the nature of the excited states in conjugatd polymers has been thoroughly described, as well as several dynamic optical processes: absorption, emission, and scattering. Of course, if limited to these processes alone, photovoltaic action would not be possible – some other kinetic pathway(s) must exist to create free charge carriers after absorption and exciton formation. This section will

overview the rest of the charge generation process, expanding upon what was mentioned briefly in Section 1.3.

The charge generation process in conjugated polymers consists of five steps:

1. Light absorption and exciton formation
2. Exciton diffusion to a donor-acceptor interface
3. Exciton dissociation at the donor-acceptor interface and charge-transfer exciton formation
4. Charge transfer exciton separation
5. Charge transport to electrodes and extraction

So far, only Step 1 has been described in detail, and so this section will begin with the story of the newly-born exciton, which must find some way to traverse the donor phase and reach a donor-acceptor interface. It does this by diffusion (exciton "migration" is also an oft-used term). Because an exciton is a delocalized entity in molecular aggregates of finite bandwidth W, it is intrinsically mobile. There are several theoretical frameworks with which to consider the diffusion of the exciton. On one hand, the exciton can be thought of as a delocalized wave with a wavelength close to that of the exciting radiation; such a wave would travel coherently throughout the aggregate until disturbed by some scattering event.[49] On the other hand, exciton diffusion can be described as a particle undergoing a random walk, traversing from one molecular site to another via a hopping mechanism. Because of the short coherence times in disordered materials like conjugated polymers (frequent scattering events), the latter description is more useful. However, the fine details of

the "hopping" mechanism are crucial. The exciton is best thought of as a localized dipole at a molecular site that hops to neighboring sites via dipole-dipole (Förster) resonant energy transfer.[75] A key feature of dipole-dipole energy transfer is that it must occur energetically "downhill", i.e., the process can only occur if the energy of the acceptor moiety is equal to or lower than that of the donor. Because the diffusion process consists of a series of rapid (~ps)[76] energy transfer events, photogenerated excitons quickly end up in low-energy, well-ordered regions of the polymer. This is a well-established experimental fact, observed both for P3HT[67,76] and MDMO-PPV[77]. This downhill exciton migration occurs whether at room temperature or at cryogenic temperatures, though the process is slightly faster at room temperature in MDMO-PPV[77] (effective diffusion length of 5 nm at 293 K vs. 3 nm at 4K). Since emission then preferentially probes well-ordered regions of the polymer film and/or polymer chains, conclusions drawn from the analysis of photoluminescence peak height ratios (R_{em}) would seem to underestimate the amount of disorder present in a given film.

In a well-mixed blend of conjugated polymer donor and fullerene acceptor, the exciton created in the donor phase is likely to reach a donor-acceptor interface during its downhill migration if the phase mixing is on the length scale of its diffusion length. Upon reaching that interface, the exciton in the polymer phase transfers its electron to the fullerene acceptor, the hole remaining behind in the polymer phase. The kinetics of the electron transfer process is given by Marcus theory, but the details of this step of the charge generation process are not so

important because it is not rate limiting in polymer-fullerene systems. For both PPVs[78] and polythiophenes,[79] the electron transfer to fullerenes is ultrafast (<200 fs) and proceeds with ~100% quantum efficiency. The fate of the resulting charge-separated state, however, is very important. In the early days of conjugated polymer:fullerene bulk heterojunction solar cells, it was assumed that, after electron transfer at the interface, the electron and hole were free to drift towards the electrodes in their respective phases.[8,35] It has become accepted now, however, that there is still a Coulombic binding energy between the electron in the acceptor phase and the hole left behind in the donor phase, and that this "charge transfer state" or "charge transfer exciton" must be dissociated before charge transport can take place.[14, 80] The concept of a charge transfer exciton, while new to the field of polymer:fullerene photovoltaics, is a relatively old concept in the fields of photochemistry and molecular crystals (e.g., naphthalene, anthracene, etc.).[49, 81] In molecular crystals, having the electron and hole on nearest-neighbor molecules was considered as an exciton delocalized over several lattice spacings, sort of an intermediately-bound exciton (looser than a tightly-bound Frenkel exciton, but tighter than a long-range Wannier-Mott exciton). In addition, it was observed that the charge transfer state was very difficult to observe through direct absorption (having oscillator strength orders of magnitude lower than the dipole-allowed $S_0 \rightarrow S_1$ transition), and it was recognized that charge transfer states exist as intermediates in carrier recombination.[49] These characteristics hold true for charge transfer excitons in conjugated polymer:fullerene systems as well – they are hard to see (via

absorbance spectroscopy) and they are an intermediate state in the charge separation process. In the following chapters, it will be shown how charge transfer states in PPV:PCBM and P3HT:PCBM systems can be detected through a red-shifted luminescence with respect to that of the pure polymer. Because the charge transfer luminescence is spectrally shifted from the luminescence of the exciton residing in the pure polymer, it is a spectral signal of interfacial regions, which can be understood from the scheme illustrated in Figure 1.20. While the luminescence signature proves to be a useful indirect measure of morphology in lab-bench solar cells, in a real device, this recombination is an undesired event that inhibits photocurrent production. Rather than recombine at the interface, the charge transfer state must dissociate. The most often-invoked desciption of the dissociation of a Coulombically bound state is Braun's 1984 adaptation of Onsager's 1938 theory ("Braun-Onsager theory")[82, 83] describing the escape probability of two oppositely-charged ions given their finite Brownian motion. This probability increases with both temperature and the electric field. While the finer points of charge transfer exciton dissociation in polymer:fullerene blends is still an unsettled area of research,[14] it can be assumed that this intermediate state dissociates due to the combined effects of thermal motion at finite temperature and the local electric field at the donor-acceptor interface.

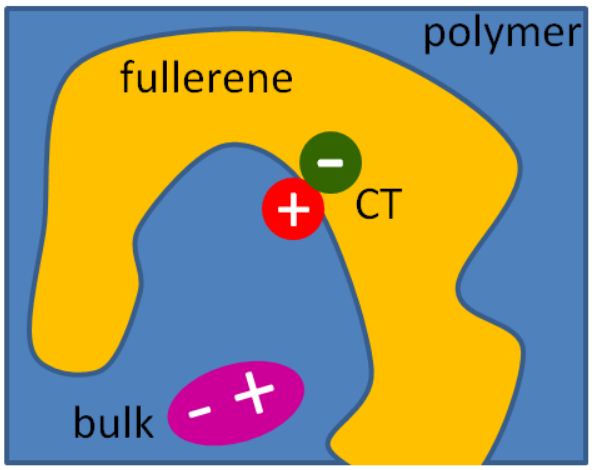

Figure 1.20 Schematic of a "bulk" exciton (a bound electron-hole pair existing in a pure phase) and a charge transfer exciton ("CT", an interfacial state where the electron and hole reside in different material phases across an interface). The specific case shown here depicts a conjugated polymer-fullerene heterojunction, in which a "bulk" exciton photogenerated in the polymer diffuses to the polymer-fullerene interface, whereupon the electron transfers to the fullerene phase.

Just like the diffusion of excitons throughout the exited state manifold, the transport of free charges has two differing descriptions, one which is characterized by a delocalized plane wave with a large mean free path, and one which is an activated site-to-site hopping mechanism. The carrier mobility of the former process decreases with temperature due to increased frequency of scattering events; the carrier mobility of the latter increase with temperature due to increased thermal energy to overcome the hopping barrier. While the latter description fits conjugated molecules much more aptly due to their large disorder and electron-phonon coupling (the charge carriers being polarons with a large accompanying lattice distortion), the former description is usually the one (implicitly) brought into play, probably for the

convenience and comfort of using the better-known language of solid states physics. For the purposes of organic photovoltaic device making and testing, the solid-state picture is the more sensible one to use, as one will need to measure and communicate open-circuit voltages, dark saturation currents, electron and hole mobilities, and so forth. It is always important, though, to be cognizant of the fact that the electrical and optical properties of organic, disordered materials result from vastly different fundamental physics than their inorganic, ordered solid-state counterparts, even if many similarities can be drawn on macroscopic length scales.

1.7 Summary and Outline

This introductory chapter has attempted to both motivate the promise of organic photovoltaics as a potential source of cheap, renewable energy, while at the same time introducing the requisite theoretical and practical background necessary for the interpretation of the experimental findings presented in the following chapters. All the while, the discussion of the electrical, optical, and physical properties of organic solar cell materials was conveyed in the context of the overarching theme of the continuum between ordered, crystalline solids and disordered, isolated molecules. Thus, the dual motivations presented here are inextricably linked: the theoretical constructs presented here are necessary for the interpretation of experimental data that will aid in the design of future organic photovoltaic devices; and at the same time, the experimental study of organic photovoltaic materials offers valuable data with which to amend the ever-evolving theoretical description of the electrical and

optical excitations in these materials. To that end, Chapter 2 highlights the P3HT:PCBM system, where the evolution of low-temperature photoluminescence and Raman scattering signatures tracks the evolution of film morphology as a function of PCBM loading, P3HT regiochemistry, and thermal annealing conditions. Chapter 3 refines the spectroscopic characterization of organic photovoltaic blends to small (diffraction-limited) length scales, via the scanning conocal imaging of charge transfer luminescence in the MDMO-PPV:PCBM systems. Through quantitative analysis of exciton bandwidths, emission intensity, and vibronic lineshapes, Chapter 4 demonstrates that competition exists between the chemical "disordering" effect of photo-degradation and the physical "ordering" effect of aggregation in pure P3HT films, each of which dominate under different processing conditions. Finally, Chapter 5 takes a turn away from focused research on conjugated polymer:fullerene blends, and instead describes the assembly, operation, and best practices of a femtosecond laser and photon counting system that has potential applications in a wide variety of materials systems.

1.8 References

[1]J. Perlin, *From Space to Earth: The Story of Solar Electricity,* (Aatec Publications, Michigan, 1999).

[2]N.S. Lewis, G. Crabtree, "Basic Research Needs for Solar Energy Utilization", United States Department of Energy, (2005).

[3]N.S. Lewis, "Powering the Planet", MRS Bulletin, **32**, 808 (2007).

[4]A. E. Becquerel, *Compt. Rend. Acad. Sci,* **9**, 145 (1839).

[5]W. G. Adams, R.E. Day, *Proc. R. Soc. London*, **25**, 113 (1876).

[6]D. M. Chapin, C.S. Fuller, G. L. Pearson, *J. Appl. Phys.*, **25**, 676 (1954).

[7]C. Brabec, N. S. Sariciftci, J. C. Hummelen, *Adv. Funct. Mat,* **11,** 15 (2001).

[8]K. M. Coakley, M. D. McGehee, *Chem. Mat.,* **16,** 4533 (2003).

[9]R. Hoffmann., C. Janiak, and C. Kollmar, *Macromolecules*, **24,** 9297 (1991).

[10]P. Anderson, *Phys. Rev.,* **109,** 1492 (1958).

[11]M. Kuik, L. J. A. Koster, G. A. H. Wetzelaer, and P. W. M. Blom, *Phys. Rev. Lett.,* **107,** 256805 (2011).

[12]M. Fox, *The Optical Properties of Solids*, (Oxford University Press, New York, 2001).

[13]M. Knupfer, *Appl. Phys. A,* **77,** 623 (2003).

[14]T. M. Clarke and J. R. Durrant, *Chem. Rev.,* **110,** 6736 (2010).

[15]J. Nelson, *The Physics of Solar Cells,* (Imperial College Press, London, 2002).

[16]C. Tang, *Appl. Phys. Lett.,* **48,** 182 (1986).

[17]G. Mor, K. Shankar, G. Paulose, O. Varghese, C. A. Grimes, *Appl. Phys. Lett.,* **91,** 152111 (2007)

[18]D. Lipomi, R. Chiechi, W. Reus, G. Whitesides, *Adv. Funct. Mat.,* **86,** 63502 (2005).

[19]C. J. Brabec, S. Gowrisanker, J. J. M. Halls, D. Laird, S. Jia, and S. P. Williams, *Adv. Mater.,* **22,** 3839 (2010).

[20]M. T. Dang, L. Hirsch, and G. Wantz, *Adv. Mat.,* **23,** 3597 (2011).

[21]J. P. Claverie and F. Schaper, *MRS Bulletin,* **38,** 213 (2013).

[22]M. Geoghegan, *Polymer Electronics,* (Oxford University Press, Oxford, 2013).

[23]H. Shirakawa, E. J. Louis, A. G. MacDiarmid, C. K. Chiang, and A. J. Heeger, *J. C. S. Chem. Comm.,* **474,** 578 (1977).

24. ref of early PPV and C60 solar cell from 1990s (candicacy?)

[25]S. E. Shaheen, C. J. Brabec, N. S. Sariciftci, F. Padinger, T. Fromherz, J. C. Hummelen, *Appl. Phys. Lett.,* **78,** 841 (2001).

[26]Z. He, C. Zhong, S. Su, M. Xu, H. Wu, and Y. Cao, *Nature Photonics,* **6,** 591 (2012).

[27]T. A. Skotheim and J. Reynods, *Conjugated Polymers: Theory, Synthesis, Properties, and Characterization* (Taylor & Francis, Boca Raton, 2007).

[28]S. Amou, O. Haba, K. Shirato, T. Hayakawa, M. Ueda, K. Takeuchi, M. Asai. *J. Pol. Sci. A: Polym. Chem,* **37,** 1943 (1999).

[29]T. A. Chen, R. D. Rieke, *J. Am. Chem. Soc.,* **114,** 10087 (1992).

[30]M. Brinkmann, *J. Pol. Sci. B: Pol. Phys.,* **49,** 1218 (2011)

[31]M. Brinkman and J. C. Wittmann, *Adv. Mater.,* **18,** 860 (2006).

[32]R. J. Kline, M. D. McGehee, E. N. Kadnikova, J. Liu, J.M.J. Frechet, and M. F. Toney, *Adv. Mater.,* **15,** 1519 (2003).

[33]S. Berson, R. DeBettignies, S. Bailly, and S. Guillerez, *Adv. Funct. Mat.,* **17,** 1377 (2007).

[34]I. Botiz, N. Grozev, H. Schlaad, G. Reiter, *Soft Matter,* **4,** 993 (2008).

[35]H. Spanggard and F. C. Krebs, *Solar Energy Materials & Solar Cells,* **83,** 125 (2004).

[36]N. S. Sariciftci, D. Braun, C. Zhang, V. Srdanov, A. J. Heeger, G. Stucky, F. Wudl, *Appl. Phys. Lett.,* **62,** 585 (1993)

[37]G. Yu, J. Gao, J. C. Hummelen, F. Wudl, and A. J. Heeger, *Science,* **270,** 1789 (1995).

[38]B. Collins, J. Tumbleston, and H. Ade, *J. Phys. Chem. Lett*., **2,** 3135 (2011).

39C. Müller, T. A. M. Ferenczi, M. Campoy-Quiles, J. M. Frost, D. D. C. Bradley, P. Smith, N. Stingelin-Stutzmann, and J. Nelson, *Adv. Mater.,* **20,** 3510 (2008).

[40]J. Zhao, A. Swinnen, G. Van Assche, J. Manca, D. Vanderzande, and B. Van Mele., *J. Phys. Chem. B.,* **113,** 1587 (2009).

[41]N. Treat, M. Brady, G. Smith, M. Toney, E. Kramer, C. Hawker, and M. Chabinyc, *Adv. Energy Mater.*, **1,** 82 (2011).

[42]S. Lilliu, T. Agostinelli, E. Pires, M. Hampton, J. Nelson, and J. Emyr MacDonald, *Macromolecules,* **44,** 2725 (2011).

[43]E. Verploegen, R. Mondal, C. J. Bettinger, S. Sok, M. F. Toney, and Z. Bao, *Adv. Funct. Mater.,* **20,** 3519 (2010).

[44]B. C. Thompson and J. M. Frechet, *Angew. Chem. Int. Ed.,* **47,** 58 (2008).

[45]R. De Bettignies, J. Leroy, M. Firon, and C. Sentein, *Synthetic Metals,* **156,** 510 (2006).

[46]C. Q. Wu, R. T. Fu, Z. Q. Li, and Y. Kawazoe*, J. Phys.: Condens. Matter,* **9,** 351 (1997).

[47]E. Hückel, *Zeitschrift für Physik,* **60,** 423 (1930.

[48]J. M. Ziman, *Principles of the Theory of Solids,* (Cambridge University Press, New York, 1972).

[49]M. Pope and C. E. Swenberg, *Electronic Processes in Organic Crystals and Polymers,* (Oxford University Press, New York, 1999).

[50]M. Kasha, *Spectroscopy of the Excited State,* (Plenum Press, New York, 1976).

[51]W. Barford, *Electronic and Optical Properties of Conjugated Polymers,* (Oxford University Press, New York, 2005).

[52]S. K. Saikin, A. Eisfeld, S. Valleau, A. Aspuru-Guzik, *Nanophotonics,* **2,** 21 (2013).

[53]M. F. Richter, J. Baier, T. Prem, S. Oellerich, F. Francia, G. Venturoli, D. Oesterhelt, J. Southall, R. J. Cogdell, and J. Köhler, *Proc. Nat. Acad. Sci.,* **104,** 6661 (2007).

[54]A. B. Koren, M. D. Curtis, A. H. Francis, and J. W. Kampf, *J. Amer. Chem. Soc.,* **125,** 5040 (2003).

[55]F. C. Spano, *J. Chem. Phys.*, **122,** 23470 (2005).

[56]F. C. Spano, *Chem. Phys.,* **325,** 22 (2006).

[57]F. C. Spano, J. Clark, C. Silva, and R. H. Friend, *J. Chem. Phys.,* **130,** 074904 (2009).

[58]T. Holstein, *Ann. Phys.,* **8,** 325 (1959).

[59]L. Pauling, *Introduction to Quantum Mechanics,* (McGraw-Hill, New York, 1935).

[60]G. C. Schatz and M. A. Ratner, *Quantum Mechanics in Chemistry,* (Prentice-Hall, New Jersey, 1993).

[61]V. Seshadri and V. M. Kenkre, *Phys. Rev. A,* **17,** 223 (1978).

[62]K. Huang and A. Rhys, Proc. R. Soc. Lond. A, 204, 406 (1950).

[63]J. Garcia-Sole, L. E. Bausa, and D. Jaque, *An introduction to the optical spectroscopy of inorganic solids*, (John Wiley & Sons, West Sussex, 2005).

[64]F. Spano, *Acct. Chem. Res.*, **43,** 429 (2010).

[65]J. Clark, J. Chang, F. C. Spano, R. H. Friend, and C. Silva, *Appl. Phys. Lett.,* **94,** 163306 (2009).

[66]J. Cornil, D. A. dos Santos, X. Crispin, R. Silbey, and J. L. Bredas, *J. Am. Chem. Soc.*, **120,** 1289 (1998).

[67]J. Clark, C. Silva, R. Friend, and F. C. Spano, *Phys. Rev. Lett.*, **98,** 206406 (2007).

[68]C. V. Raman and K. S. Krishnan, *Nature,* **121,** 3048 (1928).

[69]D. A. Long, *The Raman Effect: A Unified Treatment of the Theory of Raman Scattering by Molecules,* (John Wiley & Sons, West Sussex, 2002).

[70]C. Castiglioni, M. Del Zoppo, and G. Zerbi, *Journal of Raman Spectroscopy,* **24,** 485 (1993).

[71]B. Horovitz, *Solid State Commun.,* **41,** 729 (1982).

[72]G. P. Brivio and E. Mulazzi, *Phys. Rev. B,* **30,** 876 (1984).

[73]C. Castiglioni, M. Tommasini, and G. Zerbi, *Phil. Trans. R. Soc. Lond. A,* **362,** 2424 (2004).

[74]E. Agosti, M. Rivola, V. Hernandez, M. Del Zoppo, and G. Zerbi, *Synthetic Metals,* **100,** 101 (1999).

[75]T. Förster, *Annalen der Physik,* **437,** 55 (1948).

[76]N. P. Wells, B. W. Boudouris, M. A. Hillmyer, and D. A. Blank, *J. Phys. Chem. C,* **111,** 15404 (2007).

[77]O. Mikhnenko, F. Cordella, A. B. Sieval, J. C. Hummelen, P. W. M. Blom, and M. A. Loi, *J. Phys. Chem. B*, **112,** 11601 (2008).

[78]C. J. Brabec, G. Zerza, G. Cerullo, S. De Silvestri, S. Luzzati, J. C. Hummelen, and S. Sariciftci, *Chem. Phys. Lett.,* **340,** 232 (2001).

[79]I. Hwang, D. Moses, and A. J. Heeger, *J. Phys. Chem. C,* **112,** 4350 (2008).

[80]C. Deibel, T. Strobel, and V. Dyakonov, *Adv. Mater.,* **22,** 4097 (2010).

[81]N. J. Turro, V. Ramamurthy, and J. C. Scaiano, *Principles of Molecular Photochemistry,* (University Science Books, Sausalito, California, 2009).

[82]C. L. Braun, *J. Chem. Phys.,* **80,** 4157 (1984).

[83]L. Onsager, *Phys. Rev.,* **54,** 554 (1938).

Chapter 2

Raman and low temperature photoluminescence spectroscopy of polymer disorder in bulk heterojunction solar cell films

Adapted from the Applied Physics Letters article:

C. Carach, I. Riisness, and M. J. Gordon. *Appl. Phys. Lett.* **101**, 083302. (2012)

2.1 Abstract

Raman and low temperature photoluminescence (PL) spectroscopies were used to assess how fullerene loading and thermal annealing affect the morphology (e.g., aggregation, p-stacking, and fullerene dispersion) of regio-random and regular P3HT bulk heterojunction films. Large changes in PL and Raman show that PCBM begins to significantly hinder planarization (intra-chain) and p-overlap (inter-chain) of P3HT chains over a relatively small concentration window (30-40% and 45-55% PCBM for regio-random and regular, respectively). Mild thermal annealing of blended films was seen to restore order (i.e., vibronic PL line shapes, indicative of H-like aggregation) which result from PCBM phase segregation (lower dispersion) and growth of polymer aggregates. Overall, it is demonstrated that low-temperature PL and Raman are highly sensitive and informative metrics to evaluate polymer (dis)order in bulk heterojunction films.

2.2 Introduction

Conjugated polymer-fullerene organic photovoltaics (OPVs) based on bulk heterojunction (BHJ) architectures are widely studied due to their potential as a low-cost source of electrical energy. For the past ten years, the poly-(3-hexylthiophene):[6,6]-phenyl-C61-butyric acid methyl ester (P3HT:PCBM) system, which involves electron transfer from the polymer to the fullerene at a molecular junction,[1] has served as the workhorse of OPV research.[2] Synthetic tailoring of new, low-bandgap thiophene-based donors has recently driven efficiencies past 8%;[3] further optimization, however, will hinge on the ability to understand and control BHJ morphology. In this respect, the P3HT:PCBM BHJ retains utility as a model system to interrogate the nanoscale morphology of thiophene-based donor and functionalized-fullerene acceptor blends.

The morphology of P3HT:PCBM blends has been investigated with a myriad of experimental techniques (e.g., optical spectroscopy, x-ray scattering, electron microscopy, etc.), and a consensus on some basic observations has been reached. Perhaps TEM tomography most succinctly summarizes these observations, as it allows one to "see" that such blends are composed of a network of P3HT nanocrystallites interspersed with PCBM.[4] Recent studies employing x-ray scattering have refined this two-phase picture to include three regions: P3HT crystallites, PCBM agglomerates, and a "solution" of molecularly-dispersed PCBM and amorphous P3HT.[5] Herein, we demonstrate that data from several common optical spectroscopies, when analyzed together, can give further insight into the morphology

of P3HT:PCBM blends. Specifically, resonant Raman spectroscopy and low-temperature photoluminescence (PL) provide information about the degree of polymer ordering/alignment and fullerene dispersion by directly probing the electronic structure of P3HT. By examining optical spectra of both regioregular (rreg) and regiorandom (rrand) P3HT vs. PCBM loading and heat treatment, we show (1) how the polymer self-orders for different PCBM loadings in the spin-cast blend, (2) how the blend system rearranges upon thermal annealing, and (3) how the dynamics of P3HT:PCBM systems depend on regiochemistry.

2.3 Experimental Methods

Rreg-P3HT (M_W=52 kDa, PDI=2.2, Rieke) and rrand-P3HT (M_W=236 kDa, PDI=4.1, American Dye Source) were blended with PCBM (American Dye Source) dissolved in $CHCl_3$ (20mg/mL), and spin-cast onto ITO-coated glass slides to form ~120-150 nm thick films. Regiochemistry of the polymers was assessed with ^1H NMR (Bruker, 500 MHz) using chemical shifts in the 6.8-7.2 ppm range.[6] PL and Raman spectra were obtained with 514.5 nm excitation (Ar^+, ~2 mW, 300 mm spot, random polarization); light from the sample was collected with a 0.42NA long working distance objective and fiber-coupled to a JobinYvon iHR320 monochromator with a cooled CCD detector. Samples were cooled to 13K in a closed-cycle helium refrigerator.

2.4 Results and Discussion

Absorbance and emission (PL) can both be used to assess P3HT aggregation[7] and changes to it due to PCBM incorporation and thermal annealing. Figure 2.1 shows typical absorbance (normalized) and low-T PL (absolute) data for neat films of rreg-P3HT and PCBM. PL of P3HT:PCBM blends has traditionally been used to study quenching and conjugation length through intensity changes and qualitative blue/red-shifts of emission. However, detailed examination of the PL lineshape, based on the H-aggregate theory of Spano,[7] offers unique and more detailed information about P3HT morphology. In this scheme, P3HT domains are modeled as cofacially stacked linear aggregates, and the selection rules for emission are similar to those for H-aggregated dye molecules, namely, zero emission from the 0-0 vibronic sideband (*cf.* Figure 2.1b) for a perfectly-ordered aggregate. In the same vein, introduction of disorder "allows" 0-0 emission, making the 0-0/0-1 line intensity ratio an indicator of order in P3HT aggregates (e.g., lower 0-0/0-1 = more order). However, due to significant lineshape broadening, subtle changes in vibronic peak intensities are obscured at room temperature, making it necessary to collect PL at low temperature (see Figure 2.1b).

The evolution of low-T PL with PCBM loading of rreg- and rrand-P3HT is displayed in Figs. 2.1a and b, respectively. The lineshape of the pristine rreg-P3HT film is qualitatively similar to other low-T PL spectra in literature, as is its line intensity ratio (0-0/0-1 = 0.58, falling within the somewhat wide range of reported values from ~0.3-0.8).[8] Interestingly, the rrand-P3HT spectrum is similar to rreg-

P3HT, except for a minute increase in 0-0/0-1 (0.60 vs. 0.58) and a slightly broader linewidth. Indeed, a non-aggregating polymer would be expected to have an emission spectrum similar to an isolated (macro)molecule in solution, with approximately equal 0-0 and 0-1 line intensities (i.e., a Franck-Condon progression where S~1).[7,9] These data suggest that P3HT with ~70% regioregularity (see supplementary information[6]) is capable of at least *some* μ-stacking in the solid film.

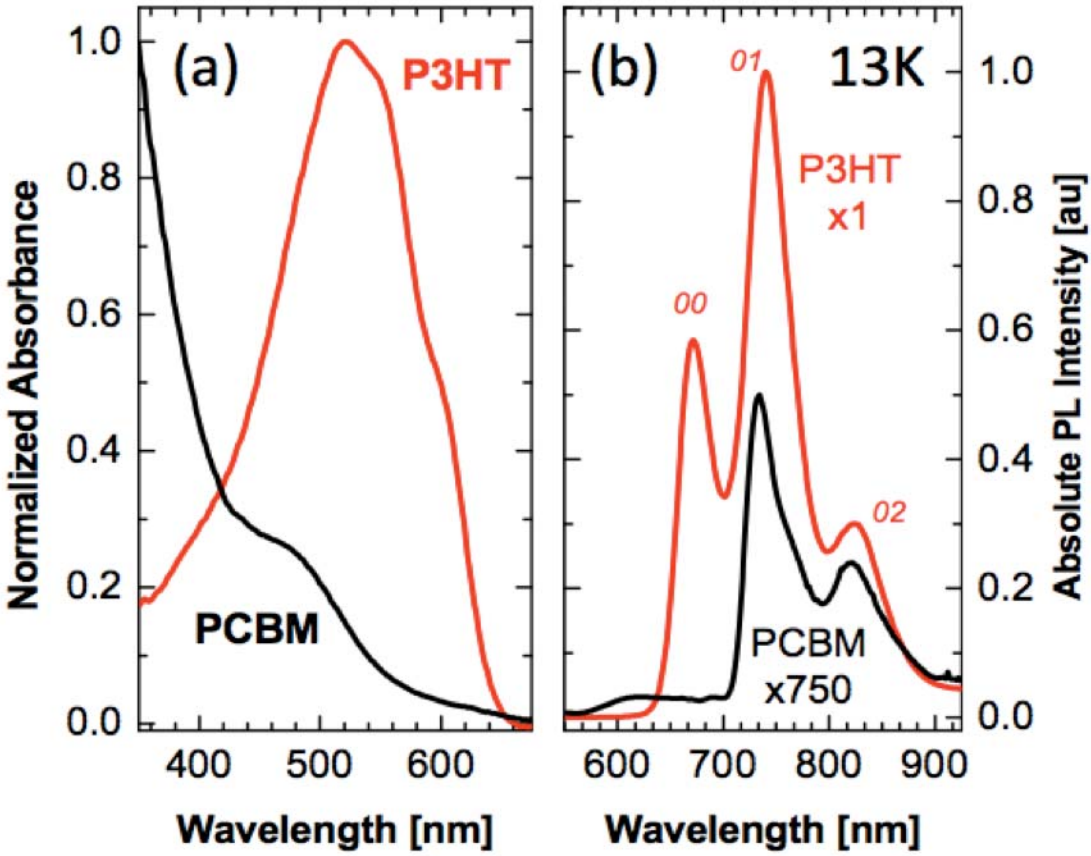

Figure 2.1 (a) Normalized absorbance and (b) 13K PL (absolute, 514.5 nm pump) of pure rreg-P3HT and PCBM films. Note: PL data was normalized by the laser pump power and detector sensitivity; in addition, the PCBM data was multiplied by 750 to display on the absolute intensity scale. The 00, 01, and 02 vibronic peaks for P3HT are noted.

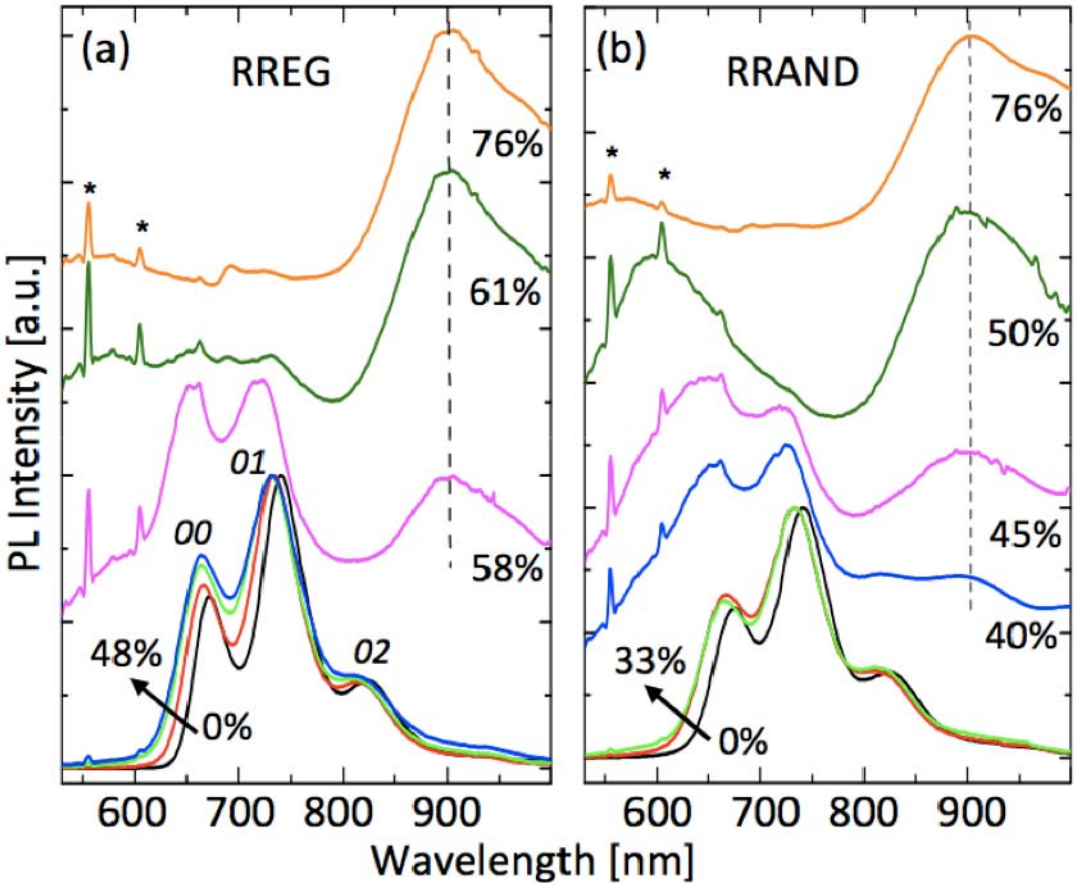

Figure 2.2 Normalized PL spectra of as-cast (a) rreg- and (b) rrand-P3HT:PCBM films at 13K using 514.5 nm pumping. PCBM content (wt. %) for each film is noted; (00, 01, 02) represent PL emission from the n = 0 excited state to the n = 0, 1, 2 vibrational levels of the ground state, and Raman peaks from P3HT are denoted as *.

As PCBM is incorporated into the as-cast film, the PL spectra of both polymers are systematically perturbed; a gradual blue-shifting of the lineshape and a concurrent increase in the 0-0/0-1 ratio occur. Such small and systematic changes in the line intensity ratio have been used to track changes in the H-aggregate ordering of pristine P3HT films as a function of molecular weight.[8b] We interpret the same small, systematic changes seen here as representative of gradual perturbation of the

H-aggregated P3HT by the fullerene, while acknowledging the following paradox: one would think that the observed PL is from chromophores that are *not* quenched, i.e., from P3HT that is more than a few exciton diffusion lengths away from PCBM. It is apparent that the rreg-P3HT in the 48% blend must somehow "feel" the disordering effect of the fullerene as its lineshape is perturbed from that of the pure film; on the other hand, the fullerene cannot be "too close" or the P3HT emission would otherwise be quenched. In any case, above a critical PCBM weight fraction (~0.35 for rrand- and ~0.50 for rreg-P3HT), small lineshape changes give way to an extreme transformation: a rapid broadening and loss of vibronic fine-structure with a simultaneous rapid loss in PL intensity (as seen by the relative growth of the Raman lines in the 550-600 nm range and broad peak at ~900 nm). We ascribe the 900 nm peak to emission from the charge-transfer exciton state formed at the polymer-fullerene interface (more easily observed in PPV:PCBM blends, but nonetheless still reported for the P3HT:PCBM system[10]).

The collective ring breathing mode (RBM) of the thiophene monomer (see Figure 2.3a) is a useful metric for polymer disorder because P3HT is a strongly coupled vibronic system (*cf*. Figs. 2.1b and 2.2). For instance, some poly-conjugated molecules show (resonant) enhancement of particular vibrational modes that are highly symmetric with respect to the conjugation direction.[12] In the P3HT case, the (collective) RBMs of the thiophene repeat units, because they involve large-scale perturbation of the p-electron cloud, couple strongly to the electronic excited state of

the polymer. As such, red (blue) shifts of the RBM are indicative of longer (shorter) conjugation lengths due to (non)optimal p-stacking of adjacent polymer chains.

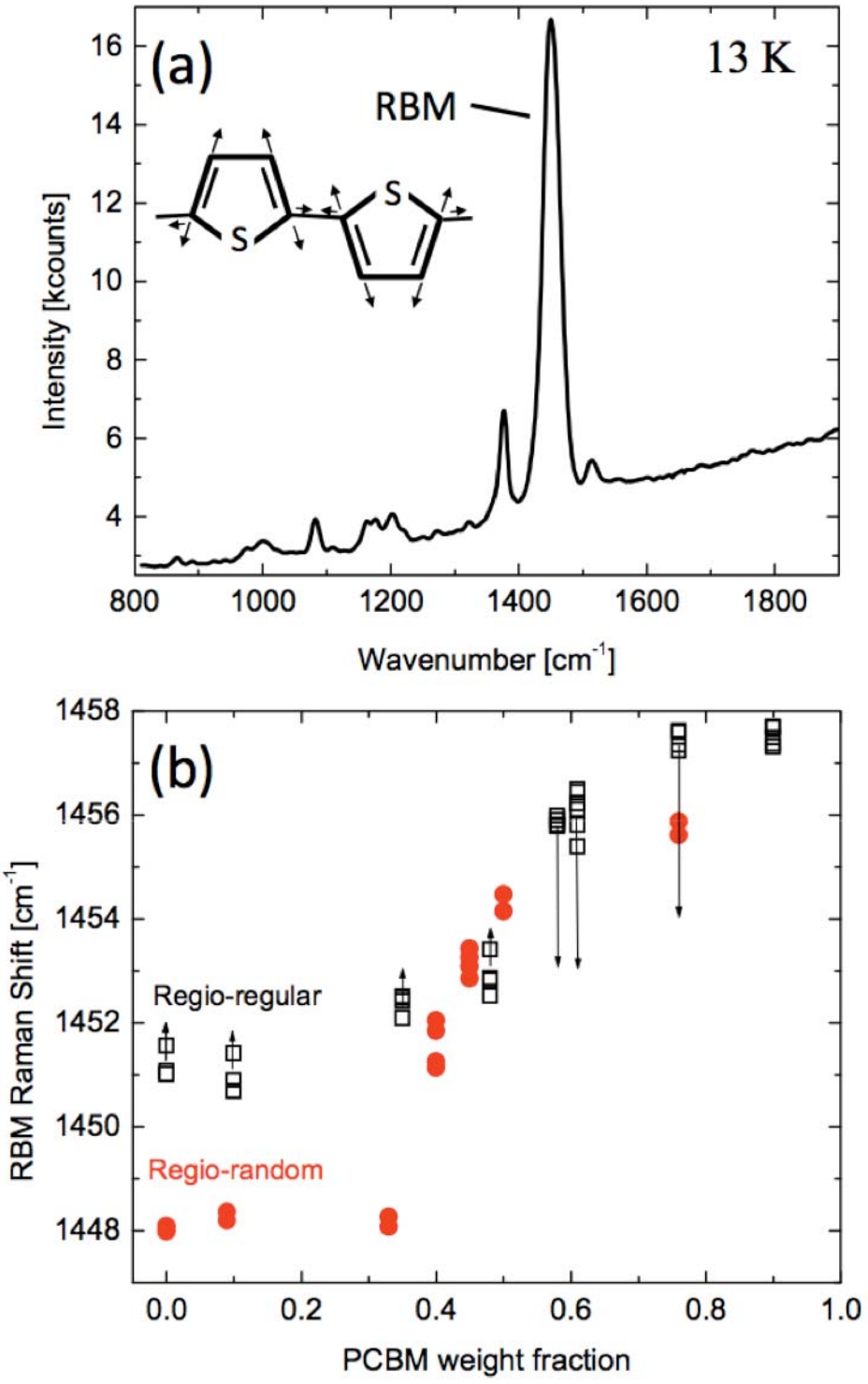

Figure 2.3 (a) Raman spectrum of rreg-P3HT at 13K using 514.5 nm pump. Atom displacements of the ring breathing mode (RBM) are noted in the inset (b) Raman shift (centroid of the peak) of the RBM for rreg- and rrand-P3HT:PCBM films. Arrows indicate the Raman shift change due to annealing the films at 145 °C for 5 min in a glovebox (< 100 ppm O_2).

The RBM Raman shift of the pure polymers in Figure 2.3b is ~1450 cm^{-1}, in good agreement with previous work for rreg-P3HT,[13a,b] but slightly different for rrand-P3HT[12]. This latter result suggests that P3HT with 70% HT linkages has solid-state ordering comparable to that of the (91%) regioregular polymer. In general, the Raman shift increases monotonically for both polymers with PCBM loading. Some groups have interpreted this shift as representative of a mean conjugation length for P3HT;[13a,14] others have considered it as due to a superposition of two different chain populations, i.e., ordered (aggregated) at low energy and disordered (unaggregated) at high energy.[13b,15] For simplicity, we take the former, noting that our conclusions are independent of these two approaches. The blue shift in the RBM is representative of both inter- and intra-chain disorder induced by the incorporation of the fullerene molecules in the as-cast film. The "S-shape" of the RBM shift with PCBM loading in Figure 2.3b is more telling: both polymers seem to be unaffected by PCBM at low loadings (i.e., there are too few fullerenes to make a noticeable reduction in polymer ordering/conjugation length), but, there is a rapid change at intermediate loadings (i.e., fullerenes hindering planarization in the intra-chain axis and p-overlap in the inter-chain axis), followed by saturation at high loadings.

Looking closer, the onset of rapid change occurs at lower PCBM loading for rrand-P3HT (~35%) vs. rreg-P3HT (~50%). While this offset may appear slight, it is echoed in PL data (Figure 2.2) and suggests a fundamental difference in the mixing of PCBM with rreg- vs. rrand-P3HT. Finally, as indicated by the arrows in Figure 2.3b, the RBM redshifts upon thermal annealing at high PCBM loading, but it

slightly blueshifts at low loading. The former trend is well-reported and attributed to crystallization/ordering of the P3HT at elevated temperatures.[13-15] We attribute the latter trend to photo-oxidation of the polymer during annealing in residual O_2 at ~100 ppm (annealing experiments in pure O_2 resulted in blue shifts of ~1.5 cm^{-1}), which dominates over any red shifts due to P3HT ordering at low PCBM loading.

It is noteworthy that the critical PCBM weight fractions for rapid evolution of PL mirror those for the sharp increase in RBM Raman shift. In fact, the progression of the Raman shift and PL lineshape, taken together, suggest that (1) the morphology of polymer-fullerene blends is regiochemistry-dependent, and (2) there is a progression of as-cast film morphology with PCBM loading for both polymers. Informally speaking, it is clear that there is *some* trait of the rrand-P3HT that allows PCBM to distort ordering more readily than in the regioregular variant. In fact, this is similar to the observation made by Hallerman *et al.*,[10a] who showed a much more marked distortion of the room-T rrand-P3HT PL spectrum at 50% loading than that of rreg-P3HT (in accordance with our low-T results herein). In addition, they noted a much greater yield of charge-transfer emission at ~900 nm, suggesting more miscibility. They hypothesized that the less-rigid backbone and greater torsional degrees of freedom of the regiorandom polymer facilitated closer contact with PCBM. We invoke this explanation here—the flexible backbone of rrand-P3HT allows fullerenes to penetrate the polymer more easily because the polymer chains are not as close together, as in the more rigid rreg-P3HT case.

The overall morphological progression is the same for both polymers, irrespective of the onset of rapid change. At low loading, the fullerene molecules do not significantly affect the formation of aggregated P3HT nor do they significantly reduce the conjugation length of the non-aggregated chains (i.e., because Raman probes *all* of the P3HT chains present). Past the critical weight fraction (high PCBM loadings), the absence of H-aggregate emission and strongly blue-shifted Raman indicate that the presence of PCBM in the as-cast film has inhibited the formation of aggregated P3HT and shortened the average conjugation length, respectively. Note that increased PCBM loading does not indicate the progressive addition of fullerene molecules to an already-existing solid-film morphology, but rather, a completely new morphology characteristic of a specific P3HT:PCBM weight ratio kinetically-frozen during spin-casting from a fast-evaporating solvent. Furthermore, it has been demonstrated that PCBM cannot fit between the alkyl side groups nor between p-stacked chains, based on steric considerations (i.e., P3HT is a non-intercalating polymer)[11] and the fact that PCBM does not enter the alkyl-stacking "a" axis of P3HT aggregates during thermal annealing;[5] therefore, the interference of PCBM with P3HT ordering must occur during spin-casting.

This picture is corroborated by the PL intensity curve for the as-cast film shown in Figure 2.4a. The rreg-P3HT PL intensity is reduced by nearly five orders of magnitude over the range of PCBM loading, though the rate of PL quenching is not constant (e.g., the reduction is more rapid in the 50-80% PCBM range). This observation is consistent with an as-cast morphology that is aggregate-free and

disperse (i.e., molecular mixing of individual polymer chains and fullerenes). With further PCBM loading, it is expected that PL quenching will saturate as each subsequent quencher is less likely to see a P3HT donor. Using melting-point analysis, Kozub *et al.* have predicted miscibility of amorphous P3HT and molecular PCBM up to 0.42 volume fraction P3HT (~65 wt.% PCBM), after which, PCBM precipitates as a separate phase.[16] The data in Figure 2.4a suggest quenching, and hence miscibility, continues up to ~75-80 wt.% PCBM, after which, a miscibility limit is reached (note: we did observe a leveling-off in PL for PCBM loadings >80% (data not shown)).

Given that better device efficiencies are (generally) obtained after thermal treatment, we examined the evolution of PL with annealing. The PL intensities of all films increase upon annealing (Figure 2.4a, upper curve) as dispersion decreases and phase segregation increases.[10a] The qualitative change in the low-T PL lineshape (Figure 2.4b), however, is equally useful in describing the morphological evolution with annealing. After annealing for 5 min/145 °C, the largely featureless 80% PCBM as-cast spectrum increases by two orders of magnitude and regains its vibronic structure.

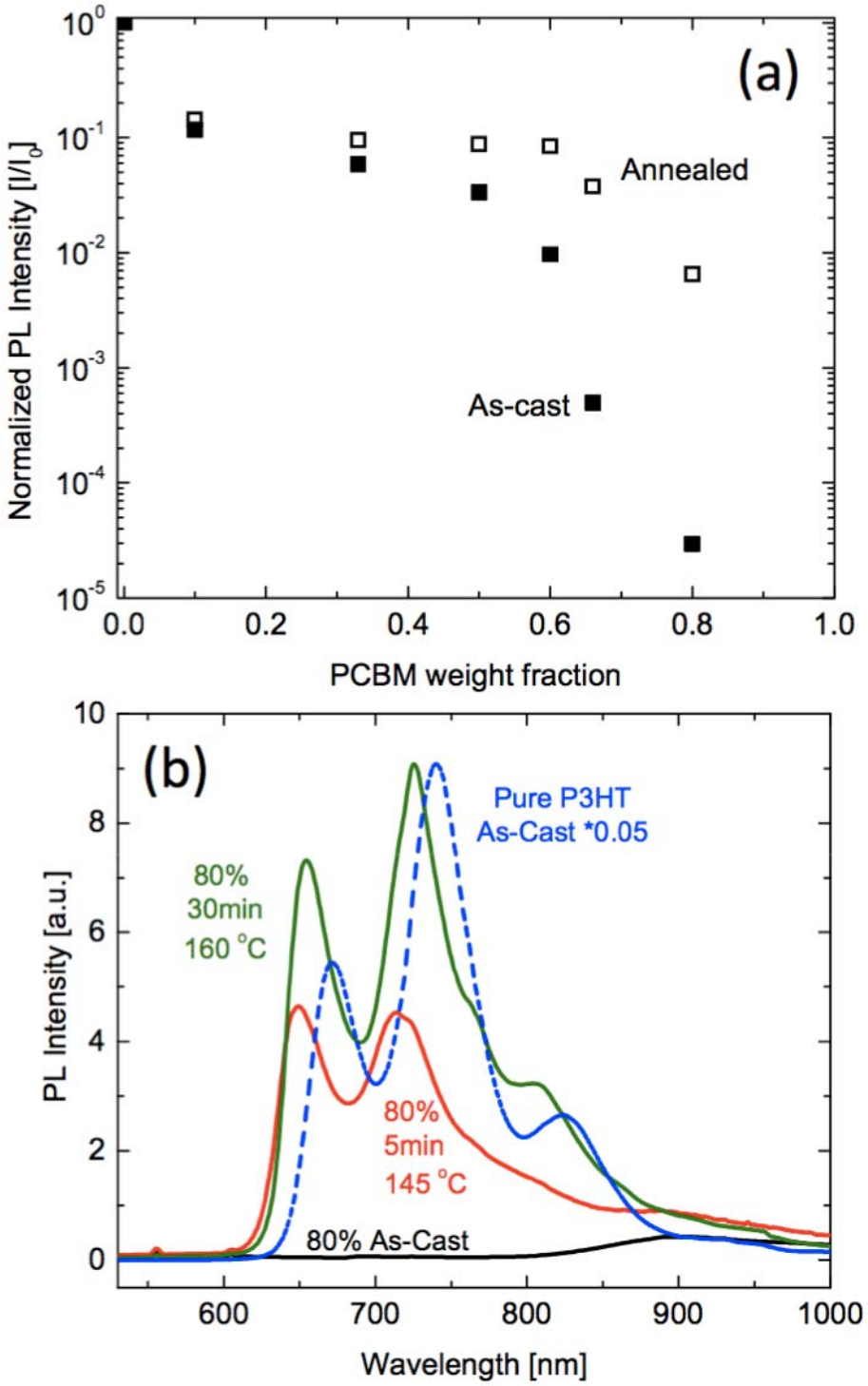

Figure 2.4 (a) Effect of 5 min/145 °C anneal on absolute PL (at 13K) from rreg-P3HT:PCBM films. PL intensity was adjusted for the P3HT wt. % in the film, system transmittance, and detector efficiency. (b) Evolution of absolute PL (at 13K) for rreg-P3HT film with 80 wt.% PCBM due to thermal annealing. The as-cast pure P3HT film is shown for reference (dashed).

The large increase in PL indicates substantial PCBM diffusion (and/or P3HT aggregation) and the emergence of H-aggregate-like PL lineshapes upon annealing are consistent with the growth of P3HT aggregates. It has been shown in ~1:1 P3HT:PCBM blends that P3HT crystal growth is rapid *and* that PCBM diffusion is near-complete under these annealing conditions.[5] However, some debate still exists as to whether P3HT crystallization proceeds unhindered or is limited by the diffusion dynamics of PCBM.[17] While the results here cannot affirm either claim, they perhaps suggest for 80% PCBM blends, where all optical spectra indicate complete dispersion in the as-cast film, that fullerene diffusion may be requisite for the polymer chains to migrate together and crystallize.

With higher anneal temperatures and longer times (30 min/160 °C), the PL spectrum only shows a modest increase in intensity (~2x), indicating that the quenching reduction, and thus PCBM diffusion, is nearly complete at milder annealing conditions (5 min/145 °C). However, the redshift of the lineshape and the decrease in the line intensity ratio after the 30 min/160 °C anneal indicate that further ordering of the aggregated polymer domains takes place in the final 25 min, even though GI-XRD data show that P3HT crystallite size (in the lateral, non p-stacking "a" direction) saturates after short annealing times (e.g., 5 min/170 °C).[5] This hints that low-T PL (namely, the 0-0/0-1 intensity ratio) may reveal subtle structural changes, by way of electronic interactions due to p-stacking, that other spectroscopies cannot observe.

2.5 Conclusion

In conclusion, we have shown that various optical measures, namely low temperature PL and high resolution Raman spectroscopy, are informative metrics of PCBM- and thermal annealing-induced (dis)order in P3HT bulk heterojunction films. Large changes in both PL and Raman shifts of the collective ring-breathing mode of P3HT (~1450 cm^{-1}) occur near ~30 and 50 wt.% PCBM for regiorandom and regioregular polymer blends, respectively, which reflect how PCBM hinders planarization (intra-chain) and p-overlap (inter-chain) of P3HT chains. Mild thermal annealing of blended films was seen to restore vibronic line shapes in the low-T PL (indicative of H-like aggregation), which result from PCBM phase segregation (lower dispersion) and growth of polymer aggregates. These combined optical measures provide an informative and straightforward way to assess morphology evolution due to processing in conjugated polymer systems that have applications in OPV and OLED research.

2.6 References

[1]I. Hwang, D. Moses, and A. J. Heeger, J. Phys. Chem. C **112**, 4350 92008); F. Padinger, R. S. Rittberger, and N. S. Sariciftci, Adv. Funct. Mat. **13**, 85 (2003).

[2]B. Collins, J. Tumbleston, and H. Ade, J. Phys. Chem. Lett **2**, 3135 (2011).

[3]Z. He, C. Zhong, Z. Huang, W. Wong, H. Wu, L. Chen, S. Su, and Y. Cao, Adv. Mater. **23**, 4636 (2011).

[4]S. van Bavel, E. Sourty, G. de With, K. Frolic, and J. Loos, Macromolecules **42**, 7396 (2009).

[5]N. Treat, M. Brady, G. Smith, M. Toney, E. Kramer, C. Hawker, and M. Chabinyc, Adv. Energy Mater. **1**, 82 (2011); S. Lilliu, T. Agostinelli, E. Pires, M. Hampton, J. Nelson, and J. Emyr Macdonald, Macromolecules **44**, 2725 (2011).

[6]See supplementary material for NMR results of polymer regioregularity.

[7]F. Spano, J. Chem. Phys. **122**, 234701 (2005); F. Spano, J. Clark, C. Silva, and R. Friend, J. Chem. Phys **130**, 074904 (2009).

[8a]P. Brown, D. Thomas, A. Kohler, J. Wilson, J. Kim, C. Ramsdale, H. Sirringhaus, and R. Friend, Phys. Rev. B **67**, 064203 (2003); [8b]J. Chang, J. Clark, N. Zhao, H. Sirringhaus, D. Breiby, J. Andreasen, M. Nielsen, M. Giles, M. Heeney, and I. McCulloch, Phys. Rev. B **74**, 115318 (2006).

[9]J. Clark, C. Silva, R. Friend, and F. Spano, Phys. Rev. Lett. **98**, 206406 (2007).

[10a]M. Hallermann, I. Kriegel, E. Da Como, J. Berger, E. von Hauff, and J. Feldmann, Adv. Funct. Mater. **19**, 3662 (2009); [10b]I. Riisness, C. Carach, and M.J. Gordon, Appl. Phys. Lett. **100**, 073308 (2012).

[11]A. Mayer, M. Toney, S. Scully, J. Rivnay, C. Brabec, M. Scharber, M. Koppe, M. Heeney, I. McCulloch, and M. McGehee, Adv. Funct. Mater. **19**, 1173 (2009).

[12]E. Agosti, M. Rivola, V. Hernandez, M. Del Zoppo, and G. Zerbi, Synthetic Metals **100**, 101 (1999).

[13a]J. Yun, J. Peet, N. Cho, G. Bazan, S. Lee, and M. Moskovits, Appl. Phys. Lett. **92**, 251912 (2008); [13b]Y. Gao and J. Grey, J. Am. Chem Soc. **131**, 965 (2009).

[14]T. Guo, T. Wen, G. Pakhomov, X. Chin, S. Liou, P. Yeh, C. Yang, Thin Solid Films **516**, 3138 (2008).

[15]W. Tsoi, D. James, J. Kim, P. Nicholson, C. Murphy, D. Bradley, J. Nelson, and J. Kim, J. Am. Chem. Soc. **133**, 9834 (2011).

[16]D. Kozub, K. Vakhshouri, L. Orme, C. Wang, A. Hexemer, and E. Gomez, Macromolecules **44**, 5722 (2011).

[17]W. Wu, U. Jeng, C. Su, K. Wei, M. Su, M. Chiu, C. Chen, W. Su, C. Su, and A. Su, ACS Nano **5**, 6233 (2011).

2.7 Supplementary Information

Regiochemistry of the polymers (dissolved in $CDCl_3$) was assessed with ^1H NMR (Bruker, 500 MHz) using chemical shifts in the 6.8-7.2 ppm range. P3HT can be fully regioregular (rreg, 100% head-tail linkages) or regiorandom (rrand, 50% HT linkages), depending on the location of the hexyl side chain (Figure 2.S1 inset). Since the aromatic proton on the thiophene ring is very sensitive to deshielding from neighboring hexyl groups, ^1H NMR in the 6.8-7.1 ppm range[1] can be used to assess regioregularity. For example, a fully random polymer typically displays four equally-weighted peaks near 7 ppm, whereas 100% rreg P3HT is dominated by the HT-HT peak at 6.98 ppm. Integration of the NMR peaks in Figure 2.S1 shows that the as-purchased P3HT samples used in this work had ~91% (rreg) and ~70% (rrand) HT conformations; as such, it was expected that the rrand polymer would exhibit characteristics of both regular and totally random polymers.

References

[1]T. Chen, X. Wu, and R. Rieke, J. Am. Chem. Soc. 117, 233 (1995).

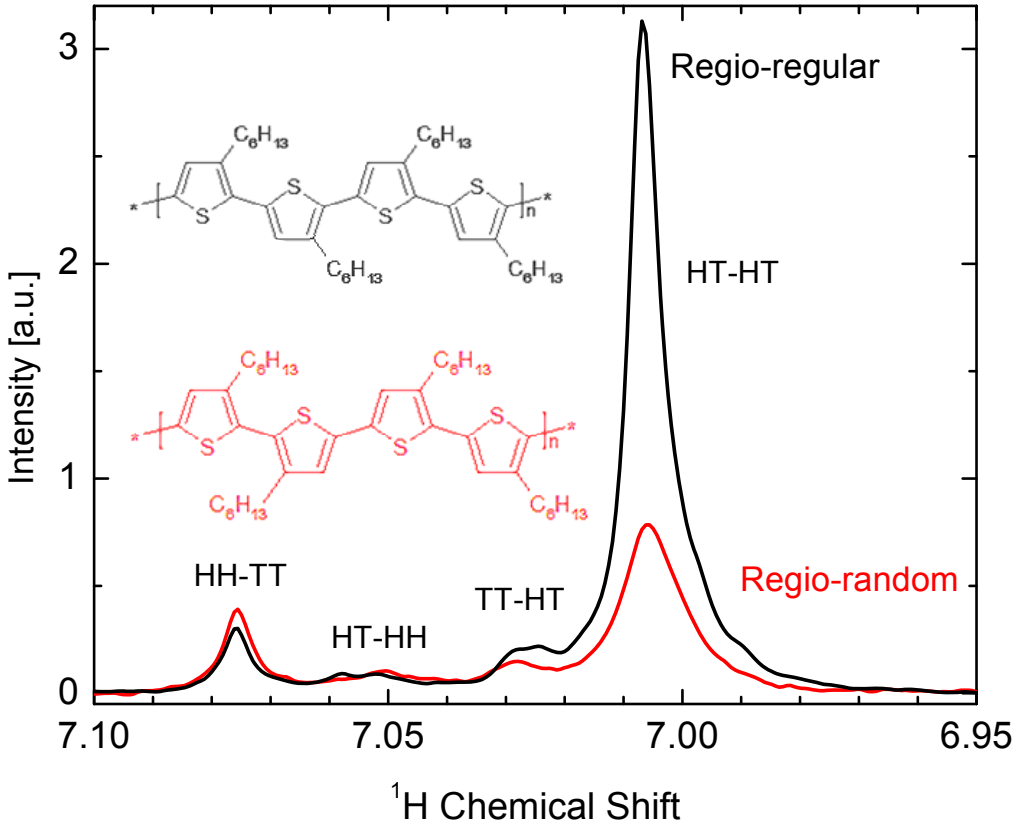

Figure 2.S1 ^{1}H NMR spectra of regioregular and random P3HT in $CDCl_3$ showing the aromatic proton shifts due to different head-tail linkages.

Chapter 3

Spatially-resolved spectral mapping of phase mixing and charge transfer excitons in bulk heterojunction solar cell films

---

Adapted from the Applied Physics Letters article:

I. Riisness, C. Carach, and M.J. Gordon. *Appl. Phys. Lett.* **100**, 073308. (2012)

3.1 Abstract

Donor-acceptor phase mixing and charge transfer excitons (CTXs) in bulk heterojunction solar cell films have been imaged using confocal photoluminescence (PL) and Raman microscopy. Spatially-resolved spectral analysis of PL was used to map fullerene diffusion and agglomeration as well as detect local changes in interfacial contact between donor and acceptor domains due to thermal annealing. CTX emission was most intense at the periphery of micron-sized fullerene agglomerates, which correlates with fullerene depletion in the surrounding film. Raman scattering indicates that the polymer phase is essentially immobile during the annealing process and that fullerene agglomerates reside atop a polymer-rich underlayer.

3.2 Introduction

Understanding charge transport processes in bulk heterojunction (BHJ) solar cells based on conjugated polymer-fullerene blends is critical to increase device efficiencies above ~7%.[1] In these materials, free carriers are created when singlet excitons formed in the photoactive polymer donor diffuse to a nearby donor-acceptor interface and dissociate.[2] However, before dissociation can occur, the singlet exciton must pass through a sub-gap charge transfer exciton (CTX) state, or bound polaron pair state, where the electron and hole reside in different material phases .[3] The CTX may subsequently dissociate into free charges that migrate through the BHJ network to the electrodes, or it may recombine through both radiative[3] and nonradiative (*e.g.* spin mixing to form triplet excitons)[4] channels. Because photogenerated charges

must ultimately pass through a CTX state at the donor-acceptor interface, the optical and electrical physics of CTXs strongly influences the extractable photocurrent and open circuit voltage of devices.[5]

Given their crucial role as intermediates in charge extraction from BHJ films, CTXs have received considerable interest as of late. For instance, the presence and energetics of CTXs in conjugated polymer-fullerene blends have been investigated using a variety of techniques including transient absorption[4,6,7] and photoluminescence (PL) spectroscopy,[8] electroluminescence,[9] ultra-violet and inverse photoelectron spectroscopy (UPS/IPES),[10] and field-induced PL quenching.[3] However, in this work, we show that confocal microscopy with spectral deconvolution of PL is a simple way to visualize CTX recombination as well as evaluate phase separation due to fullerene diffusion and agglomeration during thermal annealing.

3.3 Experimental Methods

Bulk heterojunction films (~100nm thick) with a 1:4 wt. ratio of poly[2-methoxy-5-(3',7'-dimethyloctyloxy-1,4-phenylene-vinylene] (MDMO-PPV: Mw=110kD, PDI=2.8; 1-material) and [6,6]-phenyl-C_{61}-butyric acid methyl ester (PCBM; American Dye Source) were spun from chlorobenzene onto ITO-coated glass slides and annealed at 130 °C for 1 hour in N_2 to induce phase separation. Photoluminescence (PL) and Raman spectroscopy were performed on a custom-built confocal microscope with sample scanning using ~230μW of 532nm laser light.

Light from the sample was collected in a confocal reflection geometry with a 100X objective and fiber-coupled to an imaging monochromator (JobinYvon-iHR320) with cooled CCD detector. Confocal images (20x20 μm^2) were obtained by raster scanning the sample with a piezoelectric stage using 500ms/pixel acquisition time.

3.4 Results and Discussion

Using spatially-resolved, spectral analysis of PL to locally assess phase mixing and CTX recombination requires knowledge of the optical behavior of film constituents. For instance, Figure 3.1 shows macroscale PL spectra of unannealed films of pure PCBM and 1:4 wt. ratio MDMO-PPV:PCBM blend. Spectral features in the blend PL include singlet exciton emission from MDMO-PPV (λ<700nm), lowest singlet exciton emission from PCBM (λ=700-1000 nm with λ_{peak}=740 nm),[11] and radiative recombination of the CTX state (λ>800nm with λ_{peak} ~900 nm);[3] resonant Raman peaks from MDMO-PPV (λ=550-650nm) can also be seen. Given the intensity overlap of PCBM and blend in the 700-780nm range, the PL contribution from PCBM in the far-red region of the blend spectrum (I_{blend}) can be removed through normalization and subtraction of a PCBM reference (I_{PCBM}) to provide the true CTX signal (I_{CTX}):

$$I_{CTX}(\lambda) = I_{blend}(\lambda) - I_{blend}(740)\frac{I_{PCBM}(\lambda)}{I_{PCBM}(740)} \qquad (1)$$

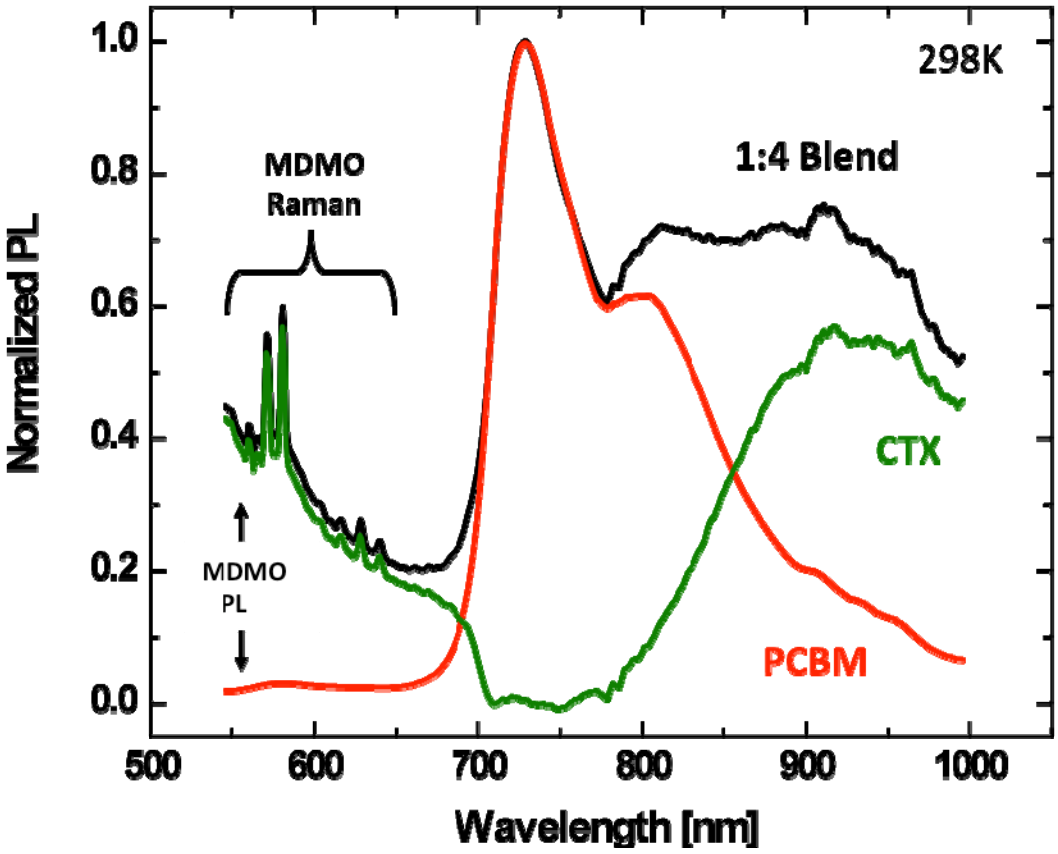

Figure 3.1 PL emission from pure PCBM and 1:4 wt. ratio MDMO-PPV:PCBM blend. CTX emission above 800nm is obtained using eqn. 1 (see text). All PL data were corrected for system transmittance and CCD sensitivity.

This broad emission starting at 800nm with a peak at 900nm represents radiative recombination of an intra-gap CTX state where the electron and hole are located in the fullerene and polymer phases, respectively. Additionally, we note that PCBM PL from a blended film blue-shifts slightly compared to pure PCBM[11] due to increased PCBM disorder in the blend (i.e., unfavorable PCBM packing and loss of fullerene-fullerene interactions); this effect was taken into account by blue-shifting the PCBM reference spectrum by 3nm to align the pure and blend PCBM PL peaks at 740nm.

Although macroscale PL provides useful information about CTX emission, film morphology can be investigated locally by combining spectral analysis of PL with confocal imaging. To that end, we employed spatially-resolved PL, using the aforementioned CTX extraction procedure, to evaluate the effect of thermal annealing on fullerene diffusion and phase separation in blended films. Figure 3.2 shows spectroscopic confocal images of PCBM PL (panel (a)) and the accompanying CTX emission (panel (b)) from an annealed film. Given that the local PCBM PL intensity can be used as a proxy for PCBM concentration, three distinct regions in panel (a) can be identified: a PCBM-rich agglomerate "A", a PCBM depletion zone "D" around the agglomerate, and a well-mixed blend zone "B" between agglomerates. The presence of these three zones in the PCBM PL image shows that thermal annealing induces PCBM diffusion and growth of micron-scale PCBM agglomerates. The diffusion

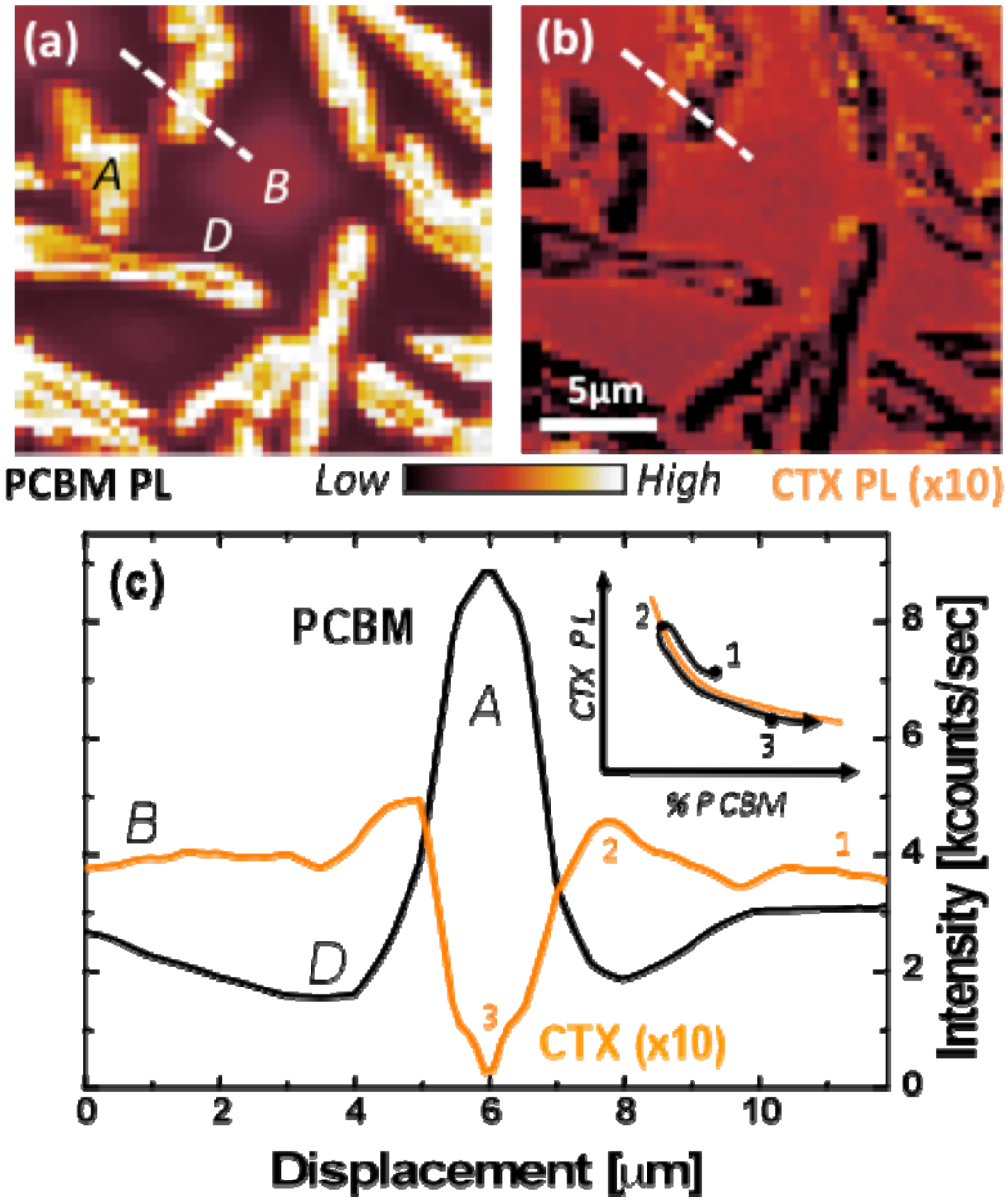

Figure 3.2 Confocal PL images of thermally annealed 1:4 wt. ratio MDMO-PPV:PCBM film in the (a) 740-750nm (PCBM PL) and (b) 850-860nm (CTX emission, scaled by 10X) regions. The *A*, *D*, and *B* notations represent the agglomerate, depletion, and blend zones, respectively. (c) Profiles of the PCBM and CTX emission along the line shown in (a). Panel (c) inset demonstrates the behavior of CTX PL as a function of PCBM loading, as represented by points (1,2,3) in the CTX line profile. All PL data were corrected for system transmittance and CCD sensitivity.

process leaves behind a depletion zone where the local PCBM concentration is low. Line profiles across the agglomerate (Figure 3.2 - panel (c)) show that the length scale for diffusion is several microns. AFM topography profiles (not shown) indicate that the agglomerate protrudes up from the bulk film (~50nm) and is surrounded by a topographically lower region, consistent with film collapse due to fullerene diffusion out of the depletion zone.

Confocal PL imaging of PCBM is an easy way to locally interrogate changes in film morphology due to annealing; unfortunately, it does not provide information about heterointerfaces that promote exciton dissociation. However, the CTX image and line profile in Figure 3.2 show that CTX emission is highest at the agglomerate-depletion zone interface and it decreases to zero inside the agglomerate. Absence of CTX signal from the agglomerate interior suggests that MDMO-PPV is not present; however, confocal Raman spectroscopy (Figure 3.3) of the agglomerate and blend zones indicates that this is not the case. The absolute Raman signal above the PL baseline in both spectra is similar, suggesting that the polymer does not diffuse during annealing.[12] Furthermore, the PL background from MDMO-PPV (see Figure 3.3) is significantly higher in the agglomerate than the blend region; this observation implies significant (vertical) phase segregation between the polymer and PCBM in the agglomerate region (i.e., the PCBM agglomerate appears to "float" on a polymer-rich underlayer). Additional measurements (not shown) indicate that the MDMO-PPV PL signal monotonically increases from the blend to depletion to agglomerate zones.

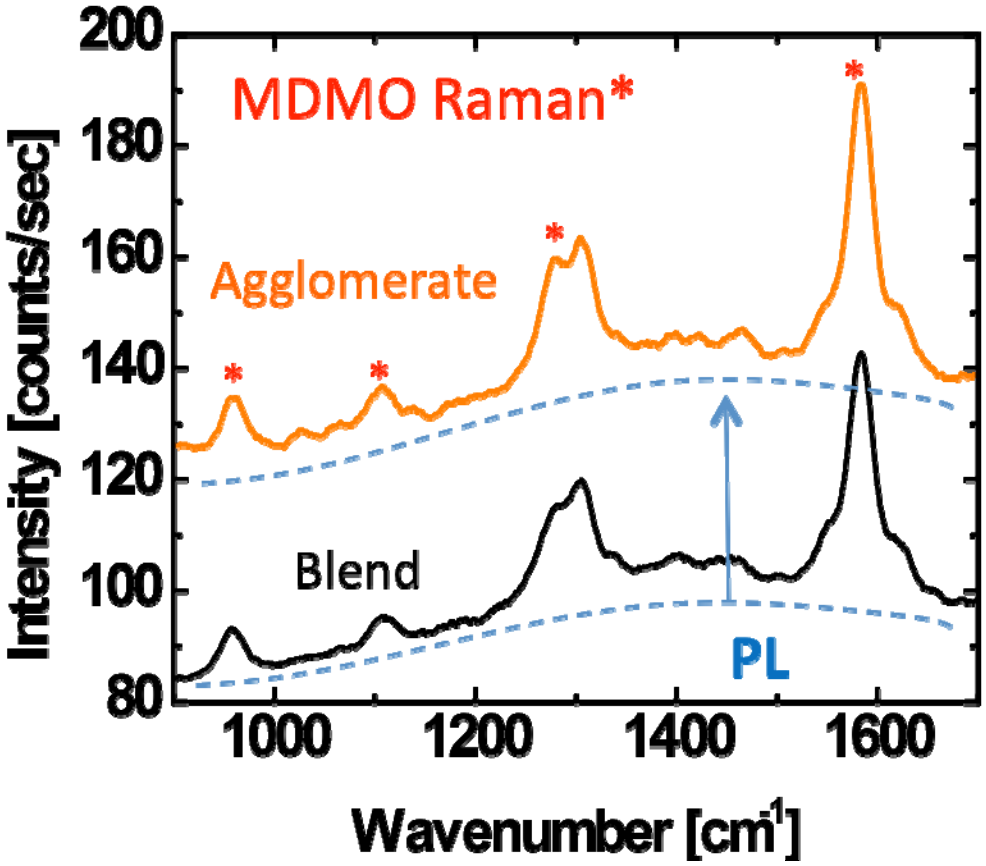

Figure 3.3 Confocal Raman spectra of thermally annealed 1:4 wt. ratio MDMO-PPV:PCBM blend in the agglomerate and blend regions (see Figure 3.2). Raman peaks from MDMO-PPV are denoted with * and the MDMO-PPV PL background is represented by the dashed lines.

To construct a picture of film morphology after annealing, all the PL and Raman data (see Figure 3.4) must be reconciled. In particular, one must explain why the CTX signal increases from the blend to the depletion zone, followed by total disappearance of the CTX signal in the agglomerate interior where the MDMO-PPV and PCBM PL signals are highest. We hypothesize the annealed morphology, and associated PL emission, involves differences in PCBM concentration, dispersion, and agglomeration in various regions as shown by the cartoons in Figure 3.4. In region "1", PCBM loading and domain size (dispersion) are high (low); polymer PL is low because polymer excitons can easily diffuse to nearby PCBM domains to dissociate, and CTX emission is governed by the local heterointerface density. However, in region "2", PCBM concentration is low and the dispersion is high; as such, polymer PL is higher than in the blend (i.e., polymer excitons must diffuse further to reach PCBM domains, resulting in greater radiative recombination) and CTX emission is increased due to more polymer-PCBM contact area (*i.e.,* higher PCBM dispersion due to lower loading,[13] as shown in Figure 3.2c inset). Finally, in the agglomerate (region "3"), polymer PL is highest due to strong vertical phase separation of the polymer and PCBM; PCBM PL is higher than in the blend region because the agglomerate is rich in PCBM, and CTX emission is nonexistent because there is minimal contact between the donor and acceptor phases. Changes in the local PCBM concentration from the blend to depletion zones are also borne out in the spectral shift of the CTX emission. For instance, Figure 3.5a shows that a significant blue shift of the CTX emission (ca. 50

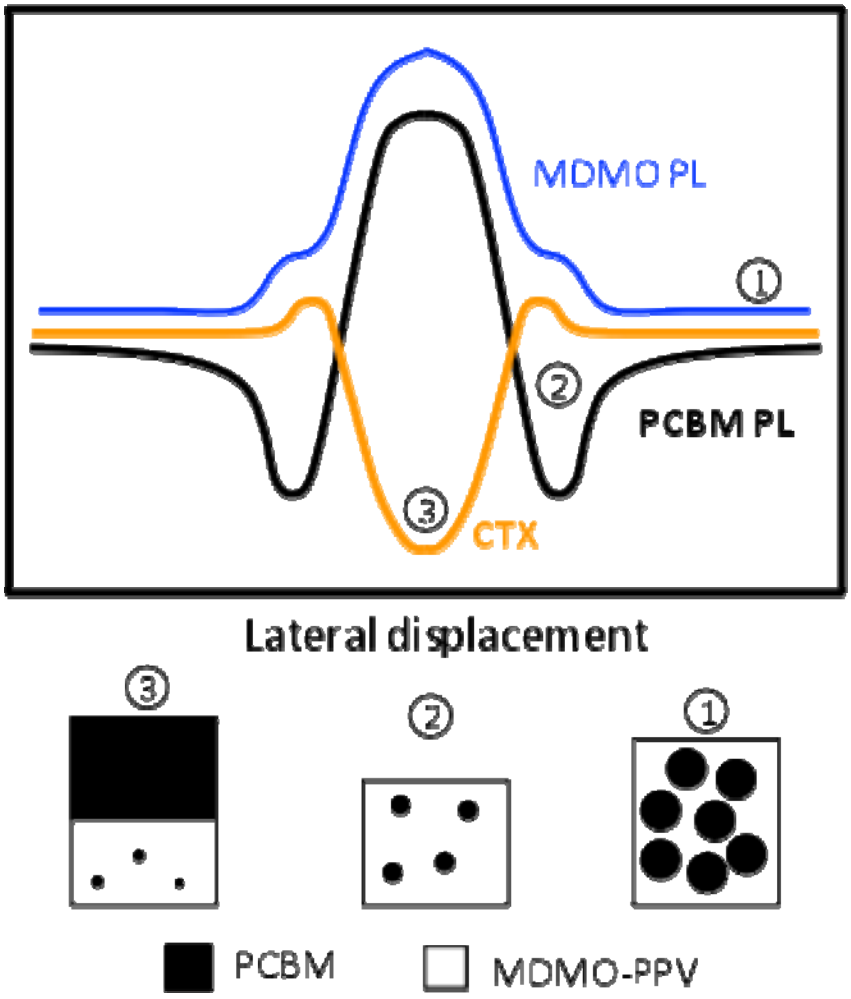

Figure 3.4 Schematic representation of MDMO-PPV and PCBM PL, as well as the CTX emission signal, for a line profile over an agglomerate (ref. Figure 3.2). The hypothesized local film morphology (e.g. PCBM concentration/dispersion and film thickness) associated with regions (1,2,3) are shown below the plot.

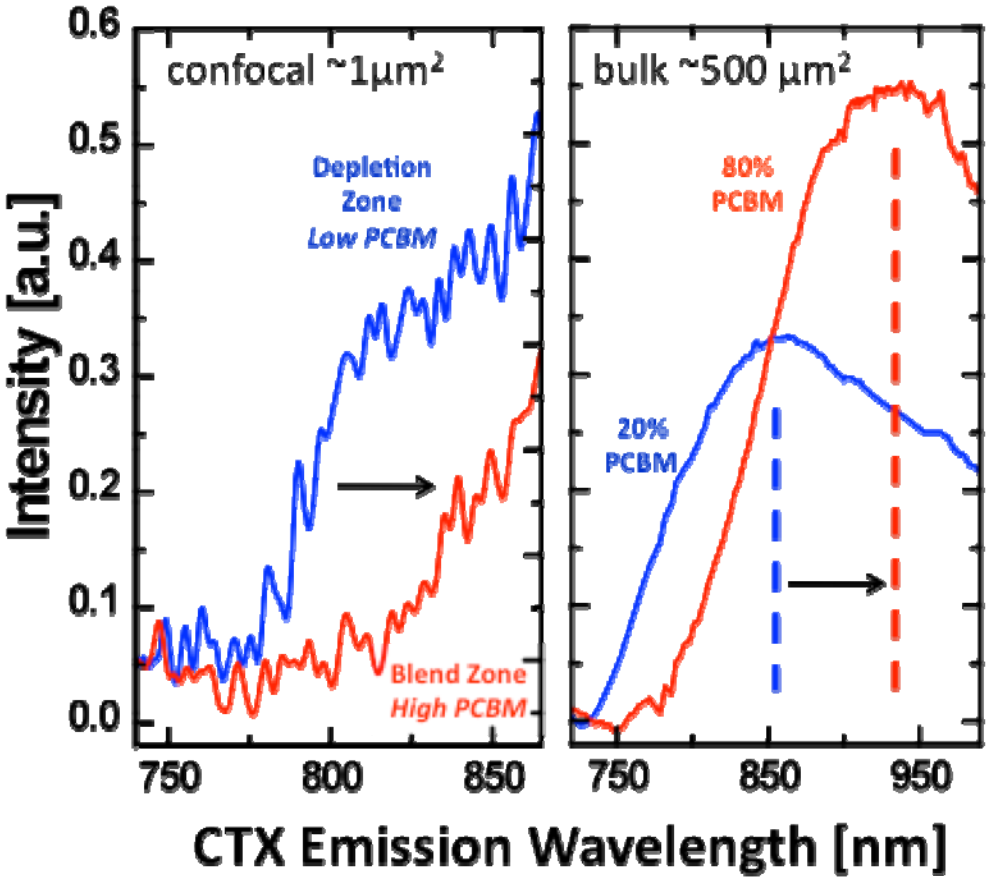

Figure 3.5 (a) Wavelength onset of PL for the CTX in the blend and depletion zones near a PCBM agglomerate (see Figure 3.2b), measured in confocal mode. (b) Macroscopic PL (probe area ~300 µm) of the CTX in unannealed MDMO-PPV:PCBM blends with 20 and 80 wt.% PCBM. In both cases, high PCBM content results in a spectral red-shift of the CTX emission.

nm) occurs in the depletion zone, relative to the blend, where the local PCBM content is low; this trend is echoed by macroscale PL measurements of blends with 20% and 80% PCBM (Figure 3.5b) as well as other studies which measured charge transfer energetics using field-dependent PL quenching[14] or Fourier-Transform photocurrent spectroscopy.[15]

The extensive vertical phase separation, compared to the micron scale extent of the depletion region in the lateral dimension, is justified if one considers PCBM diffusion to the growing agglomerate, which acts as an infinite sink (i.e., the longer the film is annealed, the larger the agglomerate becomes). Given the vast difference in film thickness (~100nm) and spatial extent of the depletion zone (order microns), PCBM diffusion in the vertical direction to the agglomerate will deplete the underlying polymer blend very quickly. As such, the strong vertical segregation of PCBM and polymer, as suggested by the intense PL from both PCBM and polymer in the agglomerate region, seems reasonable.

3.5 Conclusion

In conclusion, we have shown that spatially-resolved spectral analysis of PL emission, in conjunction with Raman spectroscopy, is an easy and informative way to assess phase mixing and changes in heterointerface density in conjugated polymer-fullerene blends due to thermal annealing. The latter was evaluated by spatially imaging radiative recombination of charge transfer exciton states that are present at the donor-acceptor heterointerface. Nucleation and growth of fullerene

agglomerates due to annealing is accompanied by the formation of three morphologically-distinct regions (*i.e.,* PCBM-rich agglomerate, polymer-rich depletion zone, and well-mixed blend zone) where the local PCBM concentration and dispersion are different. This work shows that combining spatially-resolved images of polymer and acceptor PL, CTX emission, and Raman can provide useful insight into phase separation and the formation of heterointerfaces in polymer blend solar cell systems.

3.6 References

[1]S. H. Park, A. Roy, S. Beaupre, S. Cho, N. Coates, J. S. Moon, D. Moses, M. Leclerc, K. Lee, and A. J. Heeger, Nat. Photonics **3**, 297 (2009).

[2]J. Gao, J. Hummelen, F. Wudl, and A. J. Heeger, Science **270**, 1789 (1995).

[3]M. Hallermann, S. Haneder, and E. Da Como, Appl. Phys. Lett. **93**, 053307 (2008).

[4]H. Ohkita, S. Cook, Y. Astuti, W. Duffty, M. Heeney, S. Tierney, I. McCulloch, D. Bradley, and J. R. Durrant, Chem. Comm. **37**, 3939 (2006).

[5]K. Vandewal, K. Tvingstedt, A. Gadisa, O. Inganäs, and J. Manca, Nat. Mat. **8**, 904 (2009).

[6]S. Westenhoff, I. Howard, and R. Friend, Phys. Rev. Lett. **101**, 016102 (2008).

[7]G. Grancini, D. Polli, D. Fazzi, J. Cabanillas-Gonzalez, G. Cerullo, and G. Lanzani, J. Phys. Chem. Lett. **2**, 1099 (2011).

[8]A. Morteani, P. Sreearunthai, L. M. Herz, R. Friend, and C. Silva, Phys. Rev. Lett. **92**, 045213 (2004).

[9]H. Kim, J. Y. Kim, S. H. Park, K. Lee, Y. Jin, J. Kim, and H. Suh, Appl. Phys. Lett. **86**, 183502 (2005).

[10]C. Deibel, D. Mack, J. Gorenflot, A. Schöll, S. Krause, F. Reinert, D. Rauh, and V. Dyakonov, Phys. Rev. B **81**, 085202 (2010).

[11]S. Cook, H. Ohkita, Y. Kim, J. Benson-Smith, D. Bradley, and J. Durrant, Chem. Phys. Lett. **445**, 276 (2007).

[12]N. D. Treat, M. A. Brady, G. Smith, M. F. Toney, E. J. Kramer, C. J. Hawker, and M. L. Chabinyc, Adv. Energy Mat. **1**, 82 (2011).

[13]M. Hallermann, I. Kriegel, E. Da Como, J. M. Berger, E. Von Hauff, and J. Feldmann, Adv. Func. Mat. **19**, 3662 (2009).

[14]D. Veldman, O. Ipek, S. C. J. Meskers, J. Sweelssen, M. M. Koetse, S. C. Veenstra, J. M. Kroon, S. S. van Bavel, J. Loos, and R. A. J. Janssen, J. Am. Chem. Soc. **130**, 7721 (2008).

[15]F. Piersimoni, S. Chambon, K. Vandewal, R. Mens, T. Boonen, A. Gadisa, M. Izquierdo, S. Filippone, B. Ruttens, J. D'Haen, N. Martin, L. Lutsen, D. Vanderzande, P. Adriaensens, and J. V. Manca, J. Phys. Chem. C **115**, 10873 (2011).

Chapter 4

Optical measures of thermally-induced chain ordering and oxidative damage in poly-thiophene films

Adapted from the Journal of Physical Chemistry B article:

C. Carach and M. J. Gordon. *J. Phys. Chem. B*, **117**, 1950, (2013).

4.1 Abstract

Thermally-induced chain ordering (aggregation) and oxidative damage in neat poly(3-hexylthiophene, P3HT) films was assessed using multiple optical metrics (low temperature photoluminescence (LT-PL), Raman, absorbance, and IR spectroscopies) and NMR through quantitative analysis of exciton/chromophore bandwidths, emission, vibronic lineshapes, and changes in film chemistry. Polymer morphology is discussed in light of how absorbance and PL provide complementary information about physically and chemically-related changes in conjugation due to chain alignment (kinking and torsion), π-stacking, crystallite domain growth, and photo-oxidation. LT-PL is shown to be sensitive to oxidation phenomena, while absorbance and Raman are not; in contrast, aggregation can be most easily evaluated via absorbance using a Franck-Condon-like model of vibronic excitation. IR and NMR reveal how hexyl side chains and thiophene units are attacked during annealing in O_2. We also demonstrate that competition exists between the "disordering" effect of photo-degradation and the physical "ordering" effect of aggregation, each of which dominate under different processing conditions. Ultimately, it is shown that various optical metrics of film disorder must be considered collectively to understand how processing affects film morphology.

4.2 Introduction

Photovoltaic cells made from conjugated polymer-fullerene blends have attracted much interest due to their potential to provide electrical energy at low processing costs. These so-called "bulk heterojunction" (BHJ) solar cells produce current via light absorption in the polymer, followed by electron transfer to the fullerene acceptor at a molecular junction. Chemical tailoring of polymer properties (e.g., lower bandgap and higher mobility) and empirical tuning of polymer-fullerene morphology with processing has resulted in power conversion efficiencies above 8%.[1]

The morphology of the polymer-fullerene blend is commonly optimized via thermal annealing to transform the disordered, molecularly-mixed structure into a more ordered, phase-separated morphology that enhances charge transport. In the case of the most widely studied BHJ blend, poly(3-hexylthiophene):[6,6]-phenyl-C_{61}-butyric acid methyl ester (P3HT:PCBM), annealing dynamics involve the growth of crystalline P3HT domains and the diffusion of PCBM through amorphous P3HT to form PCBM agglomerates.[2] Efforts to understand this complex morphology have spanned the entire realm of materials characterization techniques, from the most complex (e.g., synchrotron x-ray scattering[2], tip-enhanced Raman spectroscopy[3], and transient absorption[4]), to the more common (e.g., basic I-V testing[5]). Recent studies employing x-ray scattering show that the initial P3HT:PCBM BHJ morphology is composed of three phases: P3HT crystallites, PCBM agglomerates, and a "solution" of molecularly-dispersed PCBM and

amorphous P3HT.[2] Thermal annealing induces the diffusion and growth of PCBM agglomerates as well as the growth of P3HT crystallites[2,6] along the aliphatic (side chain) "a"-axis only; interestingly, the domain size in the π-stacking ("b") axis was not observed to change. This finding is rather curious because it is π-orbital coupling along the "b"-axis, in addition to transport along the polymer chain axis, that make conjugated polymers useful in photovoltaic devices—that is, excitons (and free polarons) can travel between π-stacked polymer chains and the enhanced conjugation length in the π-axis leads to a favorable red-shift[7] in absorbance.

Optical experiments on P3HT show that absorbance and emission lineshapes are affected by π-stacking. This data has been interpreted by modeling the electronic structure of π-stacked P3HT as cofacially-stacked, "H-aggregated" dye molecules[8] (we will take "π-stacked" to be synonymous with "aggregated" or "H-aggregated" throughout). In fact, absorbance and PL can provide a wealth of information about the extent and uniformity of π-stacking as well as the intra-chain conjugation length in P3HT. For instance, fitting the absorbance spectrum of P3HT to the H-aggregate model has shown that conjugation length increases with the boiling point of the solvent from which the film was cast[9] (notwithstanding the fact that the films were also annealed, which can affect aggregation also). P3HT is also very sensitive to oxidative degredation;[10] as such, "physical" aggregation phenomena (e.g., chain rearrangements, aggregate growth, etc.) must be considered in light of the fact that chemical attack of the polymer can also lead to chromophore and conjugation loss, which may otherwise be interpreted as physical disorder. We specifically address

these convoluted issues in this work using complementary optical techniques (low-temperature PL, absorbance, Raman, and IR) to study how the electronic structure of P3HT is affected by *physical* (aggregate growth, planarization, etc.) and *chemical* (oxidative damage) processes as a function of thermal annealing (low- and high-T) and background atmosphere (inert, O_2, etc.). Overall, it is shown that multiple optical metrics should be used to assess competition between the "ordering" effect of polymer chain rearrangement during annealing and the apparent "disordering" effect of photo-oxidation for films processed under different oxygen exposure conditions. In particular, we show that (1) oxidative damage to P3HT can be witnessed easily via low-temperature PL, whereas, Raman and absorbance are rather uninformative; (2) PL lineshape analysis and quenching must be considered collectively to assess polymer disorder; and (3) changes in polymer "ordering", which are thought to be due to physical effects, can be influenced considerably (or may be largely controlled) by chemical effects instead. This work also demonstrates that various optical metrics of film disorder should be viewed together to understand how processing affects film morphology and electronic structure; ultimately, reconciliation of these simple optical metrics could provide important clues and feedback to optimize device performance.

4.3 Experimental methods

Regioregular P3HT (M_W=52 kDa, PDI=2.2, Rieke 4002-EE, 91% head-tail-head-tail linkages as measured by ^{1}H NMR) was dissolved in chloroform (10 mg/mL) and

spin-cast on ITO-coated glass slides to form thin films (~80 nm). P3HT films were annealed in a glovebox (< 200 ppm O_2) or closed container on a calibrated hotplate in flowing Ar or O_2 (~500 sccm) in the dark, or under 365 nm illumination (~350 $\mu W/cm^2$). Absorbance data were taken using a home-built, double beam spectrometer (0.5 m Ebert monochromator with Hamamatsu R928 PMT). PL and Raman spectra were obtained with 457.9 or 514.5 nm pumping (Ar^+, ~2 mW, 300 μm spot, random polarization); light from the sample was collected with a 0.42NA long working distance objective and fiber-coupled to a JobinYvon iHR320 monochromator with cooled CCD detector. Samples were cooled to 13 K in a custom-built, closed-cycle helium refrigerator. IR spectra (500 averages/scan) were measured with a Bruker Equinox 55 FTIR with LN_2-cooled HgCdTe detector using P3HT samples spun on undoped Si. Liquid phase ^1H NMR (Bruker 500 MHz) was acquired by dissolving the P3HT starting material or films spun on ITO in $CDCl_3$ with sonication. Summary data presented in Figure 4.7 (e.g., absorbance and PL metrics) represent an average of at least four measurement points on each film; thickness differences across films resulted in optical density variations < 5%.

4.4 Results and Discussion

1. General Trends in Absorbance and PL

Given the complex optical phenomena and diversity of results in the literature for P3HT, we start by briefly reviewing the current understanding of absorption and emission from conjugated polymer aggregates where vibronic (electron-phonon)

coupling is important (Figure 4.1), as well as discuss common metrics used to assess chain organization. The broad absorbance feature of an as-cast P3HT film (Figure 4.1a)

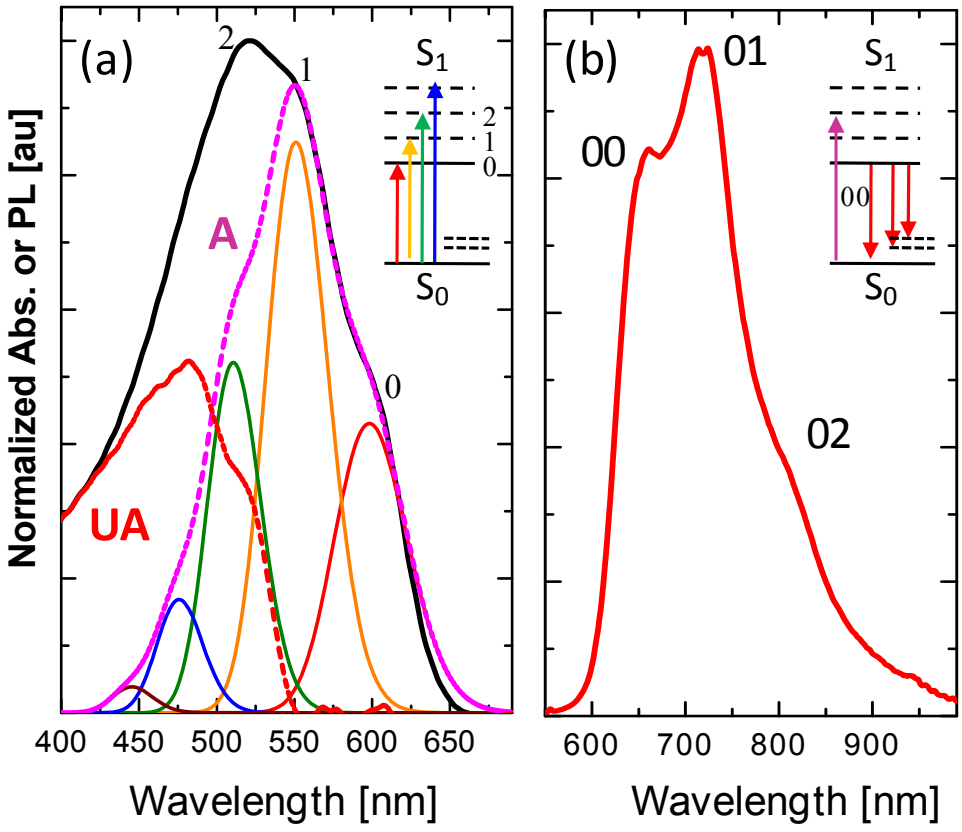

Figure 4.1 (a) Absorbance and (b) room temperature photoluminescence (514 nm pumping) spectra of as-cast ~80 nm thick P3HT film. Peak deconvolution in (a) shows absorption to different vibrational levels of the excited singlet state (0, 1, 2…), modeled using an H-aggregate-modified Frank-Condon fit. The "A" curve (dashed, purple) represents the total absorption associated with aggregated chains (i.e., adding up the Gaussian fits for the 0, 1, 2... vibrational states) and the "UA" curve (dashed, red), representing unaggregated P3HT chains, was determined by subtracting the "A" curve from the experimental data (heavy, black). Panel (b) details PL emission from the excited singlet state to different vibrational levels of the ground electronic state, i.e., the 00, 01, and 02 emissions. Fine structure in the PL is associated with Stokes losses (~1450 cm^{-1}) due to strong vibronic coupling. Insets show the various electronic (solid lines) and vibrationally-excited states (dashed lines) involved in absorption and emission

can be assigned to the collective π-π* ($S_0 \rightarrow S_1$) transition of the polymer chain, where the shoulders in the >500 nm region are indicative of vibronic coupling involving the vibrationally-excited states $\nu = 0, 1, 2$ of S_1 (the excited π* state, or exciton). Based on the pioneering theoretical work of Spano,[8] the absorbance spectrum can be thought of as a combination of (i) low-energy aggregated states ("A") that are a superposition of vibronic transitions involving Stokes losses from C=C bonds (i.e., simultaneous excitation of excitons and phonons), and (ii) a high-energy tail due to unaggregated P3HT chains ("UA"). The relative oscillator strengths of the vibronic transitions are perturbed from their single-molecule Franck-Condon (FC) form due to electronic coupling of P3HT chains along the π-axis. These absorption features can be modeled with a modified FC fit:[8]

$$A = \sum_{m=0} \left(\frac{e^{-s} s^m}{m!} \right) \left(1 - \frac{We^{-s}}{2E_p} \left(\sum_{n \neq m} \frac{s^n}{n!(n-m)} \right) \right)^2 \exp\left[\frac{-\left(\hbar\omega - E_{00} - mE_p\right)^2}{2\sigma^2} \right], \quad (4.1)$$

where W is the exciton bandwidth, S is the Huang-Rhys factor,[9] E_p is the phonon (C=C) energy loss, $E_{0\text{–}0}$ is the S_0-to-S_1 energy gap, σ is the Gaussian linewidth (i.e., $E_{0\text{–}0}$ homogeneity), and ω is the light frequency. Since the exciton bandwidth (W) is inversely proportional to the (intra-chain) conjugation length,[10] fitting Eqn. (4.1) to the measured absorbance spectrum can provide information about conjugation in the π-stacked aggregate (see Figure 1a).

We now move on to emission (Figure 4.1b); P3HT exhibits strong vibronic coupling in its photoluminescence (PL).[8c] For example, the 00, 01, and 02 shoulders in the PL correspond to transitions from the bottom of the S_1 (π^*, $\nu=0$) state to different vibrational levels of the electronic ground state S_0. These transitions are governed by selection rules peculiar to π-stacked polymer aggregates. The 00 transition is forbidden in a perfectly-ordered H-aggregate (i.e., alternating dipole moments in adjacent chromophores cancel the overall transition moment associated with the 00 emission), and as such, the $R_{em} = I_{00}/I_{01}$ peak intensity ratio is a useful measure of π-stacking disorder.[8] However, due to scattering with lattice phonons and thermally-activated emission from excitons above the bottom of the S_1 ($\nu=0$) band, i.e., lineshape broadening,[11] the utility of R_{em} measurements at room temperature as a descriptor for organization is limited. For example, room temperature PL (RT-PL) from as-cast and Ar-annealed (160 °C, 30 min) P3HT films (Figure 4.2a) are virtually indistinguishable, and the O_2 annealed film appears slightly perturbed (increased broadening in the near-IR) from the as-cast case. However, very different observations are obtained when the PL is measured at low temperature (13 K, LT-PL), as depicted in Figure 4.2b. In this case, non-radiative losses and thermally-activated hopping[11] are reduced, and emission proceeds preferentially (solely) from the bottom of S_1, resulting in a sharply-peaked, slightly red-shifted spectrum for the as-cast and Ar-annealed films. Higher R_{em} and slightly increased broadening in the Ar-annealed case might suggest that H-like aggregation (π-stacking) has decreased

with annealing. The O_2-annealed film has essentially no structure in either case, indicating destruction of the electronic structure characteristic to π-aggregated P3HT.

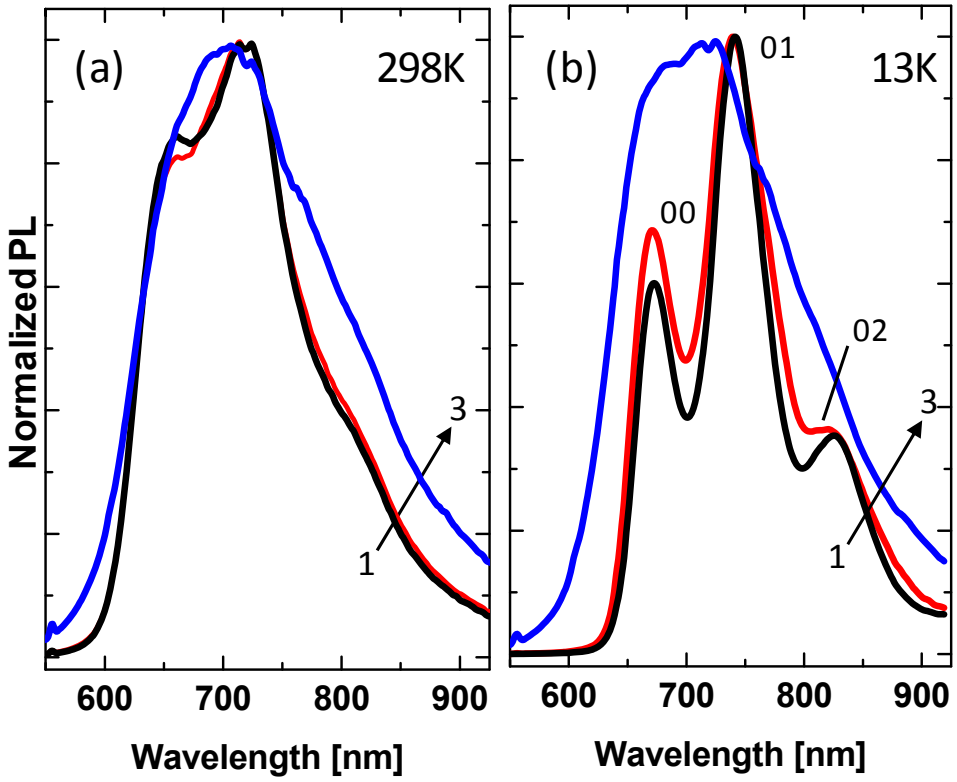

Figure 4.2 Evolution of (a) room temperature and (b) 13 K photoluminescence emission (514 nm pumping) of P3HT films annealed (160 °C / 30 min) under different O_2 exposure conditions. Processing conditions were as follows: (1) as-cast film (no annealing); (2) Ar, dark; and (3) pure O_2, dark. The 00, 01, and 02 designations represent emission from the excited singlet state to the ground, first, and second vibrationally-excited, ground electronic states, respectively.

2. Oxidation Effects

Oxidation is an important and arguably less studied topic related to OPV performance and lifetime.[12] Recent work suggests that oxygen radical attack of both the α-hydrogen and sulfur atoms of P3HT leads to the formation of alcohols,

aldehydes, ketones, and sulfinate esters[13] which eventually destroy P3HT:PCBM solar cell devices. In the following sections, we show how IR spectroscopy and NMR provide clues about P3HT chemistry as a function of processing to provide a context to interpret absorbance and PL measures of polymer chain disorder related to physical (aggregation and packing) vs. chemical (photo-oxidation) effects.

A. IR Spectroscopy

IR spectroscopy can be used to assess photo-oxidation of conjugated polymers and deduce the mechanism(s) of chain breakdown.[13] Here, we use IR to complement our LT-PL data (discussed later) with the overall intent to link changes in PL intensity and lineshapes with chemical attack of the polymer. For example, Figs. 4.3(a-b) show how the aliphatic bonds (2800-3000 cm^{-1}) of the hexyl side chain of P3HT change with annealing time. Controlled photo-oxidation for 30 min at 100 °C under UV light and O_2 flow (red curve) leads to a slight reduction in absorbance, which does not appreciably change when the annealing time is extended to 120 min. Changes in other regions of the IR spectrum (e.g., C=C, C=O, thiophene C-H) were not observed. As such, we conclude that P3HT films processed under these relatively 'mild' conditions may be subject to low levels of (oxidative) attack of the alkyl chains, but there is no evidence for destruction of the thiophene ring.

However, annealing under more extreme conditions (30 min, 160 °C, O_2) significantly reduces the aliphatic IR absorbance, as seen by the red curve in Figure 4.3(b). Annealing for 140 min. leads to further reduction of the aliphatic peaks, e.g., absorbance of the CH_2 in-plane vibration (1920 cm^{-1})[14] was reduced to ~70% of its

initial value. Longer annealing (270 min, not shown) did not result in further changes to the aliphatic region. Close examination of the fingerprint region (1300-1800 cm^{-1}, Figs. 4.3(c-d)) shows that the thiophene ring is being attacked by oxygen; at 30 and 140 min., both the symmetric (shoulder at ~1465 cm^{-1}) and asymmetric (peak at ~1512 cm^{-1}) thiophene C-C stretches (denoted #) have decayed. Annealing also results in growth of (i) the carbonyl region (~1620-1780 cm^{-1}),[13] particularly the peak at ~1724 cm^{-1} (+), which signifies that oxygen is incorporated into P3HT; (ii) olefinic C=C species (* at 1612 and 1646 cm^{-1}); and (iii) peaks in the ~1370 cm^{-1} region (X at 1355 and 1383 cm^{-1}) attributed to O-H bending modes.

Overall, IR spectroscopy results on P3HT indicate that (i) the thiophene ring is intact and a small fraction of alkyl chains may be damaged in films annealed under O_2/UV at 100 °C and (ii) annealing under O_2 at 160 °C leads to significant (oxidative) damage to both alkyl chains and the thiophene ring. It is important to note that the annealing conditions used for IR measurements, inasmuch as they provide a reference point for absorbance and PL measurements, were the most severe tested (e.g., 30 min/O_2/UV at 100 °C and 30 min/O_2 at 160 °C). It will be shown later that low-T PL is very sensitive to oxidative damage, both under severe annealing conditions as seen here (high temperature, high oxygen) as well as mild conditions (low temperature, inert environment) where changes in IR absorbance are extremely small or inconclusive.

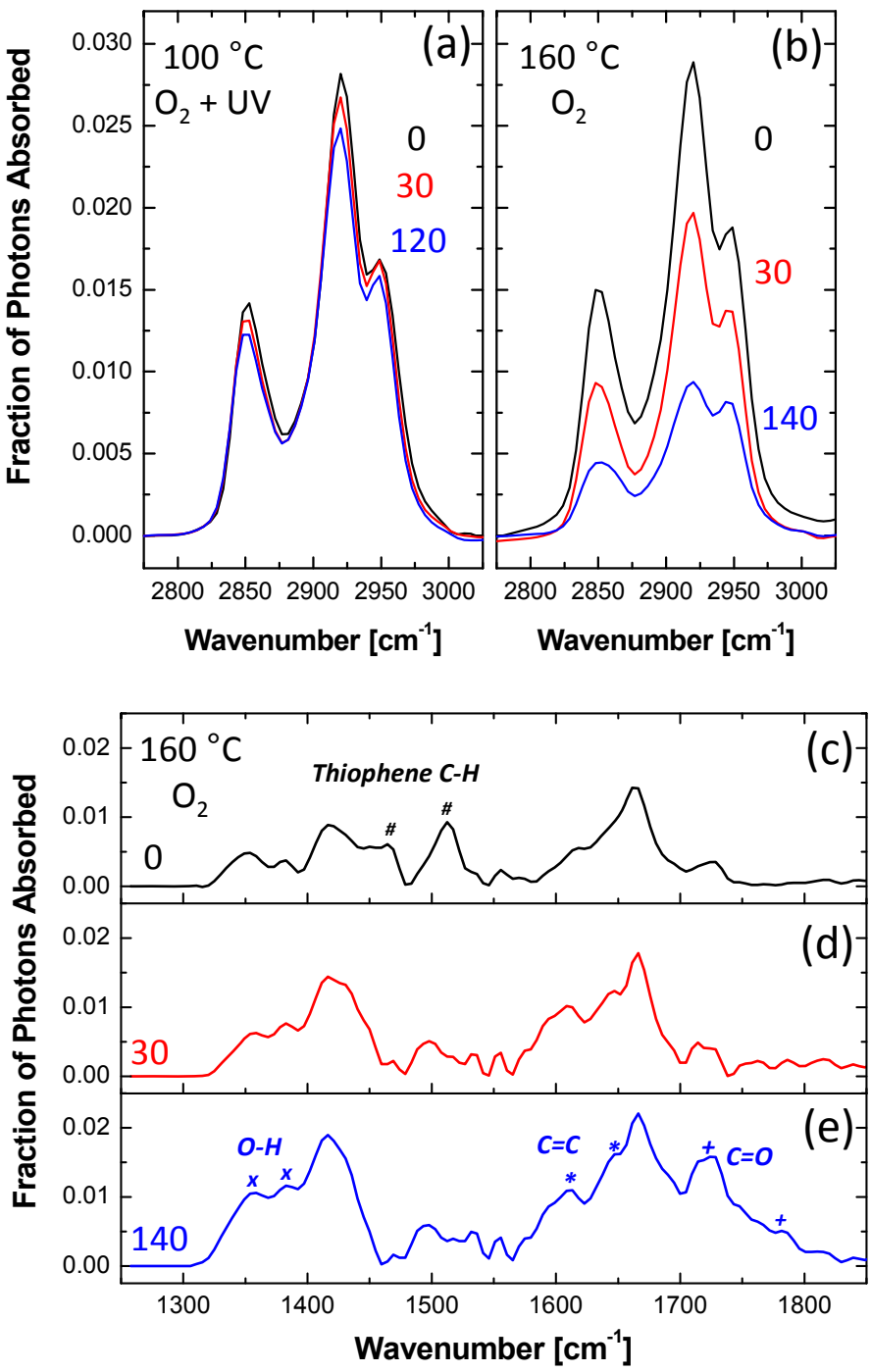

Figure 4.3 IR absorbance of P3HT films spun on undoped Si in the aliphatic (a-b) and fingerprint (c-e) regions as a function of annealing conditions in O_2. 0, 30, 120, and 140 refer to the annealing time in minutes at the condition listed. Thiophene C-H (#), O-H bending (X), C=C (+), and C=O (+) vibrations are noted for reference in panels (c-e).

B. NMR

Chemical attack of P3HT chains during film annealing in O_2 was investigated using ^{1}H NMR as shown in Figure 4.4 (see ref. [15] for peak identifications). Several general trends occur upon annealing: (i) the aromatic 'g' proton (7.0 ppm) on the thiophene ring associated with head-tail-head-tail monomer confirmation totally disappears, (ii) aliphatic protons on the hexyl side chain near the thiophene ring ('d-f') disappear, along with significant reduction in the -CH_3 proton 'a' signal, and (iii) the oxidized film shows a multitude of new peaks in the 3.5-6.0 ppm range that can be generally assigned to different alcohol, sulfinate/sulfate, and olefinic protons (panel (c)). These results clearly show that the polymer backbone and aliphatic side chain are severely attacked during O_2 annealing at 160 °C. We also note that the annealed film was very difficult to dissolve, another indicator that the aliphatic side chains were cleaved from the thiophene backbone and/or largely destroyed.

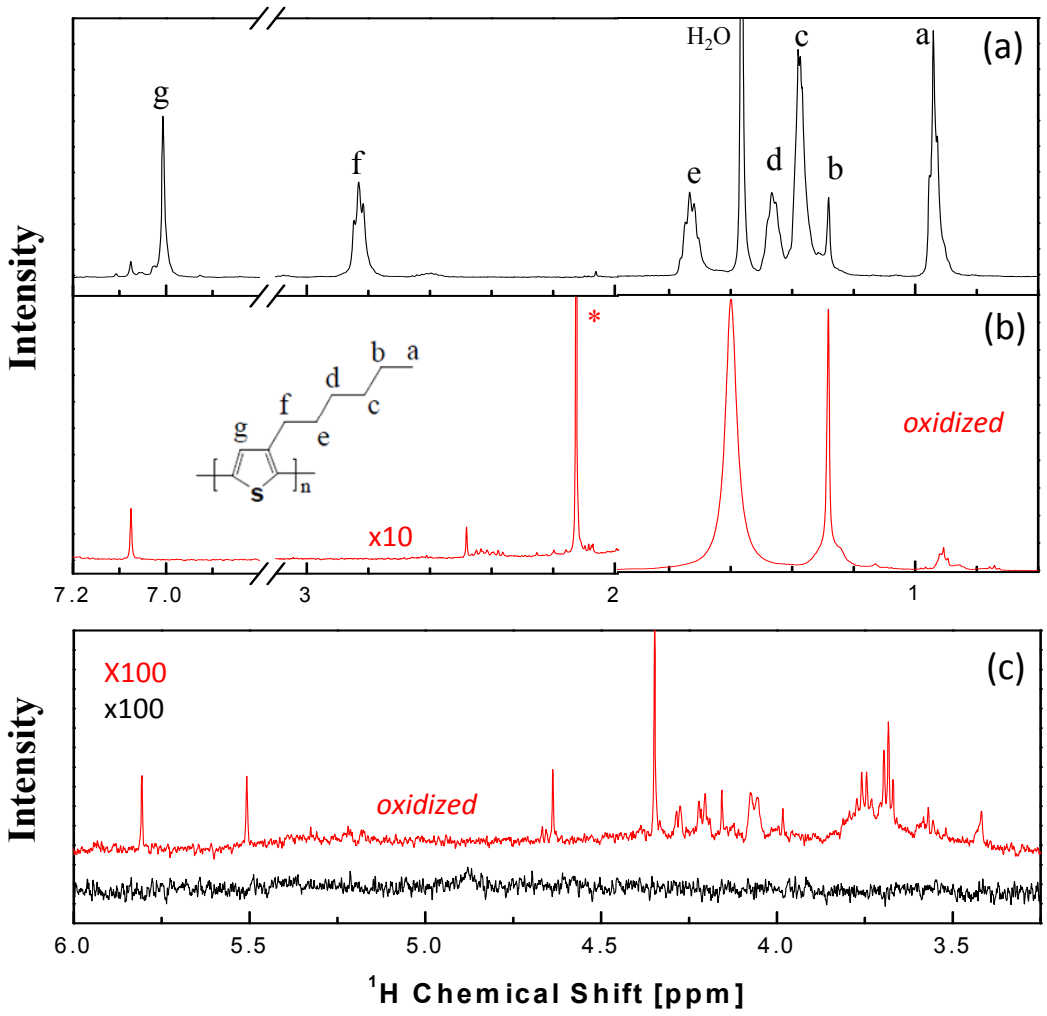

Figure 4.4 Liquid phase ^{1}H NMR of (a) as-received P3HT and (b) annealed P3HT film (160 °C, pure O_2, 140 min) dissolved in $CDCl_3$. Peaks labeled 'a-g' are associated with P3HT protons shown in the chemical structure inset. The peak at 1.56 ppm in panel (a) is due to water impurities in $CDCl_3$. The * peak in panel (b) at ~2.1 ppm is generally associated with ketone or sulfenate species. (c) Zoom of the 3.5-6.0 ppm range. The multitude of peaks for the oxidized film can be generally assigned to different alcohol, sulfinate/sulfate, and olefinic protons formed by O_2 attack of the polymer. In general, annealing P3HT films in O_2 results in loss of the aromatic proton (g) and destruction of the hexyl side chain bonding near the thiophene ring (protons d, e, and f).

C. Raman Spectroscopy

As a matter of completeness, we should mention that the Raman shift of the P3HT ring-breathing mode (RBM) at ~1450 cm^{-1} can be used as an indirect measure of conjugation length due to its symmetry with respect to the conjugation direction and change in nuclear coordinate from $S_0 \rightarrow S_1$.[16] Blue-shifts (i.e., positive changes in cm^{-1}) of this Raman mode indicate reduced conjugation length; such changes have been used to measure the disordering effect of PCBM incorporation into P3HT films.[17a] In the present case with neat P3HT films, annealing at 160 °C for 30 min in O_2 caused a blue-shift of ~8 cm^{-1} in the RBM (see Figure 4.5). Closer examination also shows that the C=C (1450 cm^{-1}) to C-C (1372 cm^{-1}) ratio is higher (14.6 vs. 10.3) for the annealed vs. as-cast films; an increase in this ratio has been previously attributed to lower planarity of P3HT chains and an associated reduction in conjugation length.[7,17b] Because the RBM can be deconvoluted into a superposition of unaggregated (higher cm^{-1}) and aggregated (lower cm^{-1}) peaks,[7,17b] blue shifts can be attributed to an increase in unaggregated chains. However, it is improbable that annealing would lead to less aggregation and/or less planarity; as such, we ascribe the changes in the C=C (RBM) and C-C peaks as due to oxidation-induced conjugation reduction (i.e., *chemically-induced* disorder) rather than changes in the *physical* alignment/packing of the P3HT chains (the interplay of physical vs. chemical changes will be discussed in the next section). On a final note, we should mention that the RBM blueshift upon annealing could also be interpreted as aggregated chains being more susceptible to oxygen attack (i.e., less Raman intensity

from aggregated chains compared to unaggregated). This seems unlikely if the oxidation reaction is limited by oxygen diffusion through the P3HT film, as aggregates have lower oxygen diffusion coefficients for poly(3-alkylthiophenes).[18] However, others have postulated that regions with higher conjugation length[19] (aggregated chains) may be more susceptible to oxygen attack because ionization potentials are lower than for unaggregated regions. The importance of and interplay between these two mechanisms is still under investigation.

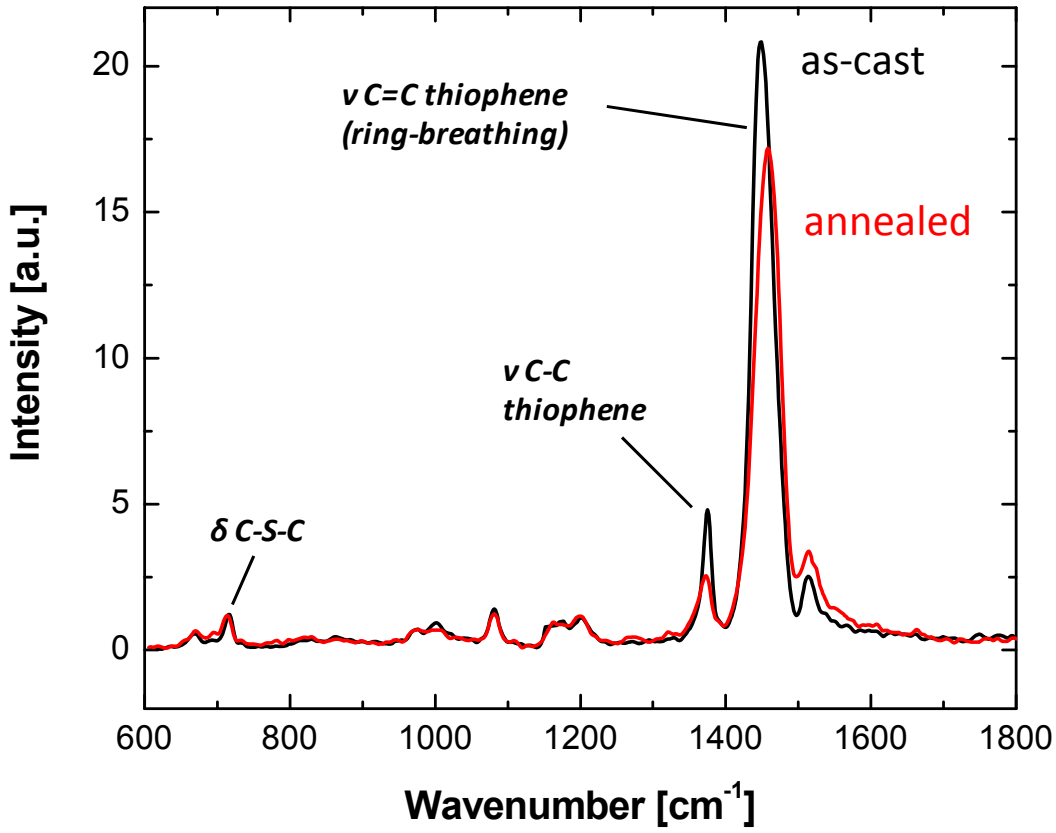

Figure 4.5 Raman spectra of as-cast (black) and annealed (30 min, 160 °C, O_2; red) P3HT films on ITO at 13 K. Annealing induces a blue-shift of ~8 cm^{-1} in the thiophene ring breathing mode (C=C, ~1450 cm^{-1}) and a relative increase in the C-C mode at 1372 cm^{-1}.

The C-S-C vibration at ~700 cm^{-1} did not appear affected by O_2 annealing, though the line strength was very small. Changes in the RBM Raman shift for less severe annealing conditions were relatively small ($\leq$ 2 cm^{-1}) and do not show a monotonic progression with annealing severity. Furthermore, no changes in the C-C or C-S-C peaks were observed for less severe annealing conditions. As such, the Raman shift of the RBM, inasmuch as it can be a proxy for conjugation loss by way of reduced vibronic coupling, seems to be a less sensitive metric of oxidation-induced disorder compared to the low-T R_{em} ratio and PL intensity.

3. Physical vs. Chemical Modification of Electronic Structure

Given the aforementioned backdrop, we now consider rigorous assessment of absorbance and low-T-PL metrics of P3HT films annealed in different environments and discuss general trends (see Figure 4.6). Changes in absorbance and PL can be associated with 'electronic' disorder, which is due to both physical (i.e., changes in conjugation length due to chain kinking and torsion, aggregation phenomena related to π-stacking or crystallite domain growth, etc.) and/or chemical (e.g., oxidative defects) effects. General trends in the absorbance and PL data with annealing can be summarized as follows: (i) absorbance changes are very small, especially for low annealing temperatures and (ii) low-T PL lineshape (R_{em}), line broadening, and intensity appear more sensitive to annealing temperature and O_2 background. Although absorbance changes are small, close inspection shows that (i) the low-energy vibronic shoulders (~550-625 nm) become better-defined, and (ii) the

absorbance envelope blue-shifts. Since increased definition of absorbance shoulders is broadly associated with better polymer order, but blues-shifts are associated with disorder, interpretation of the absorbance spectrum based on inspection alone seems ambiguous. In fact, spectral deconvolution and parameter extraction using the H-aggregate model discussed earlier is necessary to make any conclusions from absorbance data. In contrast, LT-PL spectra display unambiguous changes upon superficial inspection; a clear trend of increasing R_{em} and linewidth with greater O_2 content and annealing temperature is readily apparent. These general tendencies are summarized more quantitatively using metrics related to conjugation length and π-stacking (i.e., exciton bandwidth, σ , R_{em}, and integrated PL intensity), as shown in Figure 4.7.

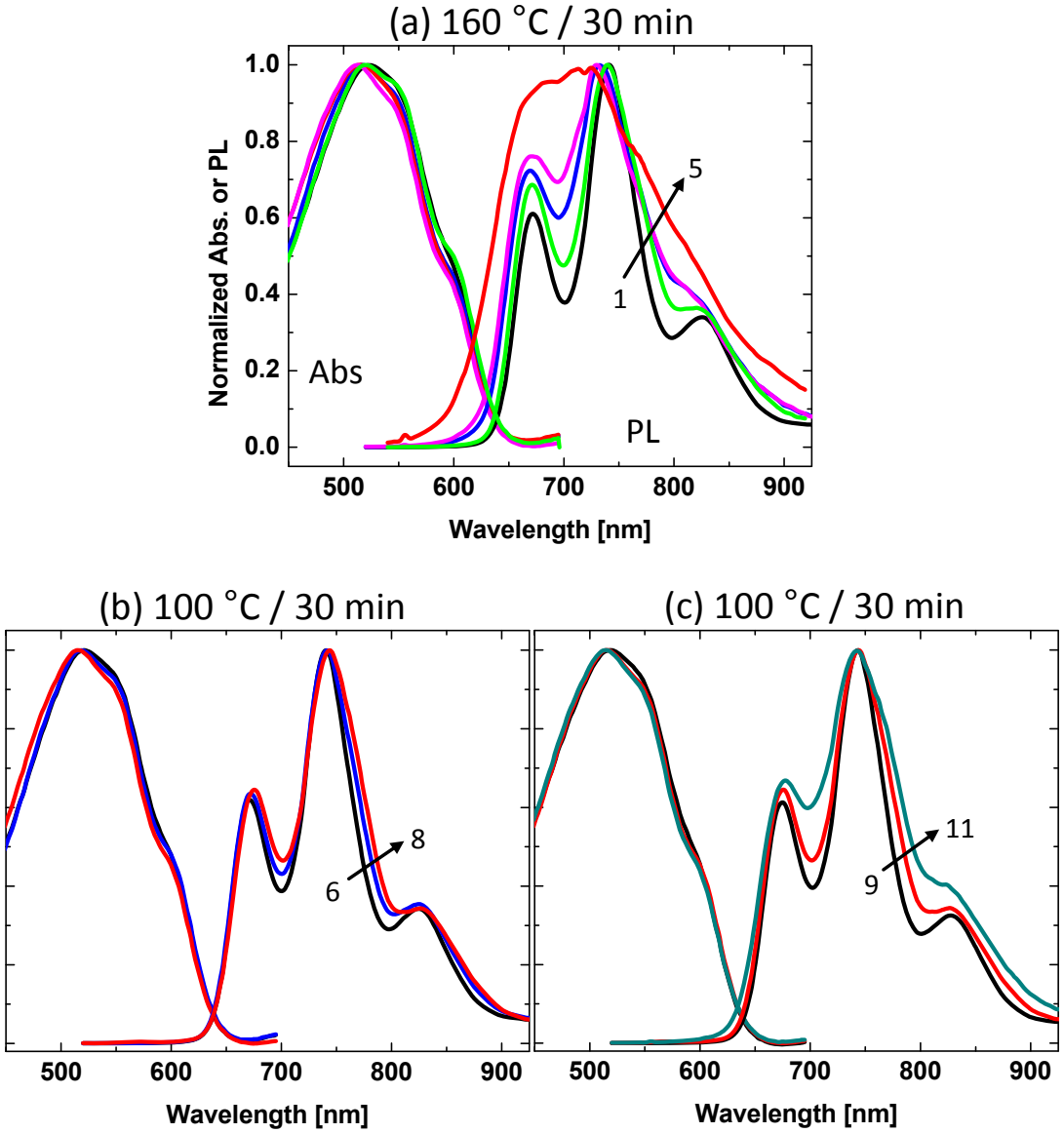

Figure 4.6 Normalized absorbance and low temperature photoluminescence (13 K) spectroscopy (514 nm pumping) of P3HT films processed under different thermal annealing conditions. Curves are as follows: (1) as-cast; (2) glovebox (< 200 ppm O_2), dark; (3) Ar, dark; (4) air, dark; (5) pure O_2, dark; (6) as-cast; (7) Ar, dark; (8) pure O_2, dark; (9) as-cast; (10) pure O_2, dark; (11) pure O_2 + 365 nm UV light.

In general, absorbance metrics (W and σ, Figure 4.7a) indicate that mild annealing under low O_2 conditions (i.e., 100 °C in Ar or 160 °C in a glovebox with < 200 ppm O_2) leads to a decrease in W (larger conjugation length) with a concomitant decrease in the Gaussian linewidth (σ), which indicates that the average chromophore energy gap ($E_{0\text{-}0}$) is more homogeneous. The former can be explained by (i) planarization of polymer chains or perhaps (ii) π-stacked aggregate growth in the "b"-axis at elevated temperature (which leads to better conjugation), and the latter can be attributed to more favorable chain alignment (greater uniformity of packing) in the "b"-axis. GI-XRD data mentioned in the introduction eliminates explanation (ii) because domain growth in the "b"-axis has not been shown to occur under annealing. As such, absorbance data suggest that mild annealing of neat P3HT films results in H-aggregated P3HT domains composed of slightly-straighter, more-uniformly stacked polymer chains. We further note that W and σ say nothing about possible aggregate growth in the aliphatic "a"-axis. Alternatively, a rough measure of the total amount of aggregated P3HT can be obtained by taking the ratio of aggregated to unaggregated absorbance (A:UA in Figure 4.1) and adjusting for their respective oscillator strengths; such analysis has shown a slight increase in aggregated P3HT in neat films spun from high boiling point solvents.[20] Similar treatment of the data herein (chloroform solvent) gives an aggregate fraction of ~41% for all films (data omitted for brevity), with an insignificant (< 2-3%) change upon annealing.

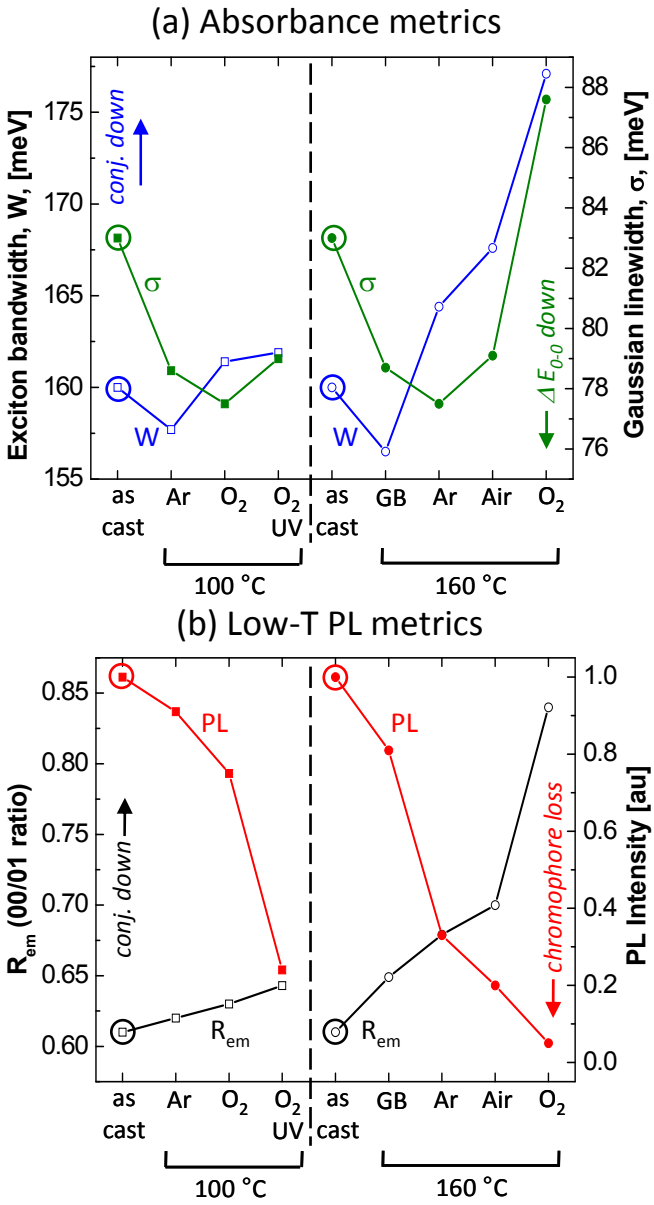

Figure 4.7 Summary of key optical metrics of P3HT chain "disorder" extracted from (a) absorbance and (b) low-T photoluminescence data in Figure 4.6 for various film processing conditions. Category labels represent films processed in argon + dark (Ar), O_2 + dark (O_2), glovebox with < 200 ppm O_2 + dark (GB), air + dark (Air), or O_2 + 365 nm UV exposure (O_2/UV), respectively, at 100 °C or 160 °C for 30 min. In panel (a), the exciton bandwidth (W) and E_{0-0} homogeneity, as measured by the Gaussian linewidth σ, are represented on the left (open symbol) and right (closed symbol) axes, respectively. For panel (b), R_{em} is the 00/01 vibronic intensity ratio (left, open symbol) and the integrated PL emission (right, closed symbol), normalized to the as-cast film case. Data for the as-cast film are represented by circled points. Changes in conjugation length, loss of chromophores, and homogeneity of E_{0-0}, as implied from the data, are noted. See text for details on the various optical metrics.

The remaining absorbance data generally show that W increases and σ decreases with the severity of the annealing process (e.g., higher T and/or higher O_2 result in larger changes; see Figure 4.7a) compared to the as-cast case. While the trend in σ still suggests more uniform packing, interpreting larger W as a reduction in conjugation on *physical* grounds seems implausible (i.e., P3HT chains should not "straighten out" during low-T annealing but "curl-up" during high-T annealing). The "reverse" trend in W with high-T annealing is more likely attributed to O_2-related defect generation that decreases π-orbital overlap between chains, rather than changes in chain linearity and planarity. This conclusion is discussed below in light of the PL and IR data, which indicate that chromophore loss is a more likely culprit.

The PL trends in Figs. 4.6 and 4.7b show that the overall emission intensity decreases progressively with the severity of annealing in terms of temperature and oxygen environment, while R_{em} and vibronic peak linewidths (webbing between the 00, 01, 02 peaks) steadily increase. Lower emission intensity is commonly attributed to two effects: (i) the population of aggregated chains has increased due to annealing (i.e., aggregates are less emissive[21] in some cases), and/or (ii) (oxidative) defects result in an effective loss of chromophores. Without complementary data, the dominant cause of the PL reduction remains ambiguous. The absorbance analysis discussed previously, as well as the aforementioned GI-XRD studies, would suggest that (i) does not occur (i.e., there is no crystal growth along the π-axis). The increase in R_{em} ratio and vibronic linewidth, which can only be quantitatively assessed at low temperature, indicates disordering of the polymer film with annealing under nearly

all conditions. As before, a more physically-disordered structure upon annealing is deemed as implausible. Moreover, the IR and NMR data shown in Figs. 4.3-4 and discussed in Section II conclusively show the presence of oxidized species after annealing (e.g., carbonyls, hydroxyls, sulfinates, and olefins). Therefore, the trend in R_{em} is only consistent with (ii), i.e., oxidative defects decrease the active chromophore population and reduce the effective π-stacking of polymer chains, which is (indirectly) observed as a loss of H-like aggregation (increasing R_{em}).

The fact that the more mildly-annealed films exhibit changes in absorbance metrics (W and/or σ) that point to an increase in "order" on physical or structural grounds, coupled with changes in PL metrics that point to a decrease in "order" on chemical grounds (R_{em}), imply that: (i) absorbance is more sensitive to "physical" ordering of P3HT, whereas LT-PL is more sensitive to chemical (oxidative) effects, and (ii) annealing P3HT films under similar conditions likely leads to simultaneous increases in both planarization/packing *and* oxidative damage. The increase in R_{em} upon annealing even in a controlled, low-oxygen environment, illustrates how oxidation is extremely sensitive to annealing temperature (160 °C vs. 100 °C). In fact, it has been shown that O_2 damage to conjugated polymers (PPVs) can take place "in an evacuated cryostat",[22] which we interpret as at least rough vacuum (< 10 mTorr). Furthermore, LT-PL can even discern small changes that occur under milder annealing conditions at 100 °C (Figure 4.6b). Although changes in R_{em} are small for the Ar and O_2-annealed films, the increased PL linewidths ("webbing" of the

vibronic peaks) give a clear image of the progression of disorder with annealing conditions. This study is extended one step further in Figure 4.6c, where the PL spectrum of an O_2-annealed film with UV illumination is added. The increased disorder is again seen through an increase in R_{em} and the broadening of the vibronic peaks, consistent with the accepted mechanisms of degradation hinging on UV-induced activation of oxygen radicals. It should be noted that the only change in the IR spectra of a similar film (30 min, 100 °C, O_2, UV – red curve, Figure 4.3a) is a very small reduction in the IR absorbance of the aliphatic C-H bonds, and the absorbance metrics (slightly smaller σ, slightly bigger W – Figure 4.7a) are inconclusive due to their sensitivity to the simultaneously-occurring physical aggregation. Therefore, out of the optical spectroscopy techniques employed (absorbance, IR, and PL), PL appears to be the most sensitive to oxidative disordering of P3HT.

The increased sensitivity of PL intensity to oxidation, as opposed to absorbance, can be explained by the propensity of excitons to migrate to highly-electronegative chemical defects like carbonyls where they are quenched via electron transfer to the defect.[23,24] The PL yield is reduced not only by fewer photogenerated excitons (i.e., through reduced absorbance), but also through oxidative defect-induced quenching. The qualitative changes in LT-PL spectra described here reinforce the idea of defect-induced disruption of conjugation (an effective increase in disorder) with increased annealing in O_2 that leads to an effective *decrease* in H-aggregation. This effect is clearly chemical in origin and competes with thermally-driven, physical

reorganization processes which tend to *increase* linearity/planarity of polymer chains and aggregate growth in the aliphatic axis (only), where the former affects the quality of π-stacking (H-aggregation) but not the domain size (in the π-stacked direction).

4.5 Conclusions

Overall, we can say that multiple optical metrics should be used to evaluate processing-induced (dis)ordering in polythiophene films. In particular, we saw that absorbance (especially) and room temperature PL were relatively insensitive to annealing-induced ordering and oxidative attack of neat P3HT films cast from the same solvent. However, it was seen that low-T PL, where temperature-induced broadening and thermally-activated emission from within the exciton band are minimized, was an effective and sensitive means to interrogate changes in π-conjugation due to mild annealing and/or oxidative defects. IR and NMR data from films annealed under severe conditions (30 min, 160 °C, O_2) show tell-tale signs of oxidative damage, i.e., attack/destruction of the aliphatic side chain and thiophene protons, creation of alcohol and sulfur-oxygen moieties, and the formation of carbonyl groups. Finally, this work shows that complementary (optical) metrics must be considered *collectively* to gain better insight into how film processing, through both physical *and* chemical phenomena, influences local morphology and electronic structure of conjugated polymer films.

4.6 References

[1]He, Z.; Zhong, C.; Huang, X.; Wong, W.; Wu, H.; Chen, L.; Su, S.; Cao, Y. *Adv. Mater.* **2011**, *23*, 4636.

[2]Treat, N. D.; Brady, M. A.; Smith, G.; Toney, M. F.; Kramer, E. J.; Hawker, C. J.; Chabinyc, M. L. *Adv. Energy Mater*. **2011**, *1*, 82.

[3]Wang, X.; Zhang, D.; Braun, K.; Egelhaaf, H.; Brabec, C. J.; Meixner, A. J. *Adv. Funct. Mater.* **2010**, *20*, 492.

[4]Grancini, G.; Polli, D.; Fazzi, D.; Cabanillas-Gonzalez, J.; Cerullo, G.; Lanzani, G. *J. Phys. Chem. Lett.* **2011**, *2*, 1099.

[5]Kim, Y.; Choulis, S. A.; Nelson, J.; Bradley, D. D. C.; Cook, S.; Durrant, J. R. *Appl. Phys. Lett.* **2005**, *86*, 063502.

[6]Lilliu, S.; Agostinelli, T.; Pires, E.; Hampton, M.; Nelson, J.; Macdonald, J. E. *Macromolecules* **2011**, *44*, 2725.

[7]Tsoi, W. C.; James, J. T.; Kim, J. S.; Nicholson, P. G.; Murphy, C. E.; Bradley, D. D. C.; Nelson, J.; Kim, J. *J. Am. Chem. Soc.* **2011**, *133*, 9834.

[8a]Spano, F. C. *J. Chem. Phys.* **2005**, *122*, 23470; [8b]Spano, F. C.; Clark, J.; Silva, C.; Friend, R. H. *J. Chem. Phys.* **2009**, *130*, 074904; [8c]Spano, F. *Acct. Chem. Res.* **2010**, 43, 429.

[9]Garcia-Sole, J; Bausa, L. E.; Jaque, D. *An introduction to the optical spectroscopy of inorganic solids* **2005**, West Sussex: John Wiley & Sons, Ltd.

[10a]Cornil, J.; dos Santos, D. A.; Crispin, X.; Silbey, R.; Bredas, J. L. *J. Am. Chem. Soc.* **1998**, *120*, 1289; [10b]Manas, E. S.; Spano, F. C. *J. Chem. Phys*. **1998**, *109*, 8087; [10c]Barford, W. *J. Chem. Phys*. **2007**, *126*, 134905.

[11]Mikhnenko, O. V.; Cordella, F.; Sieval, A. B.; Hummelen, J. C.; Blom, P. W. M.; Loi, M. A. *J. Phys. Chem. B* **2008**, *112*, 11601.

[12]Jorgensen, M.; Norrman, K.; Krebs, F. C. *Solar Energy Materials & Solar Cells*. **2008**, *92*, 686.

[13]Manceau, M.; Rivaton, A.; Gardette, J.; Guillerez, S.; Lemaitre, N. *Polymer Degradation and Stability*. **2009**, *94*, 898.

[14]Abdou, M. S. A.; Holdcroft, S. *Macromolecules.* **1995**, 26, 2954

[15a]Barbarella, G.; Bongini, A; Zambianchi, M. *Macromolecules* **1994**, *27*, 3039; [15b]Chen, T.; Wu, X.; Reike, R. *J. Am. Chem. Soc.* **1995**, *117*, 233; [15c]Mao, H.; Xu, B.; Holdcroft, S. *Macromolecules* **1993**, *26*, 1163.

[16]Agosti, E.; Rivola, M.; Hernandez, V.; Del Zoppo, M.; Zerbi, G. *Synth. Met.* **1999**, *100*, 101.

[17a]Carach, C.; Riisness, I.; Gordon, M. J. *Appl. Phys. Lett.* **2012**, *101*, 083302; [17b]Gao, Y.; Grey, J. K. *J. Am. Chem. Soc.* **2009**, *131*, 9654.

[18]Luer, L.; Egelhaaf, H.-J.; Oelkrug, D.; Cerullo, G.; Lanzani, G.; Huisman, B.-H.; de Leeuw, D. *Organic Electronics* **2004**, *5*, 83.

[19]Abdou, M. S. A.; Orfino, F. P.; Son, Y.; Holdcroft, S. *J. Am. Chem. Soc.* **1997**, *119*, 4518.

[20]Clark, J.; Chang, J.; Spano, F. C.; Friend, R. H.; Silva, C. *Appl. Phys. Lett.* **2009**, *94*, 163306.

[21]Nguyen, T.-Q.; Martini, I. B.; Liu, J.; Schwartz, B. J. *J. Phys. Chem. B* **2000**, *104*, 237.

[22]Klimov, V. I.; McBranch, D. W.; Barashkov, N.N.; Ferraris, J. P. *Chem. Phys. Lett.* **1997**, *277*, 109.

[23]Chang, Y.; Su, W.; Wang, L. *Solar Energy Materials & Solar Cells*. **2008**, *92*, 761.

[24]Yan, M.; Rothberg, L. J.; Papadimitrakopolos, F.; Galvin, M. E.; Miller, T. M. *Phys. Rev. Lett.* **1994**, *73*, 744.

Chapter 5

Assembly and Implementation of a Femtosecond Laser System for Transient Fluorescence Measurements on Organic Photovoltaic Materials

If a Planck resonator is in a radiation field, the energy of the resonator can be changed by the transfer of energy from the electromagnetic field to the resonator; this energy can be positive or negative depending on the phases of the resonator and of the oscillating field...these two processes we shall call "changes in state, induced by radiation."

- Albert Einstein

Nobody in football should be called a genius. A genius is a guy like Norman Einstein.

- Joe Theisman

This chapter highlights the development of a pulsed laser and photon counting system for more advanced study of organic photovoltaic materials. Whereas the previous chapters made use of fluorescence spectra as a function of *wavelength* to interrogate organic photovoltaic blends, the apparatus discussed in this chapter measures the fluorescence intensity as a function of *time*. The main purpose here is to provide a user's manual to a somewhat complicated home-built system for future Gordon Lab researchers. This constitutes a good portion of the current chapter, and is contained in Section 5.6 As always, there is important background knowledge to be learned, especially in the unfamiliar and esoteric field of mode-locked ultrashort pulses (Section 5.3) and the probably-unfamiliar, if not-so-esoteric, field of time correlated single photon counting (Section 5.5). In addition, there will be brief coverage of laser basics (Section 5.1), the Ti:sapphire crystal employed here (5.2), and a discussion of applications of ultrafast lasers, including those related to the study of organic photovoltaic materials (5.4). Finally, Section 5.7 presents proof-of-concept transient fluorescence measurements made with this system.

5.1 Laser Basics

A good starting point for an overview of lasers is the name itself – **L**ight **A**mplification by the **S**timulated **E**mission of **R**adiation. Let us start at the end and work backwards. Lasers produce *Radiation* that has four unique qualities when compared to non-laser light sources: laser light is monochromatic (one color), bright (high power per area), directional (low beam divergence), and coherent (the phase of

the EM wave does not change in space or time).[1] In fact, non-laser light is often termed incoherent light (e.g., flames, light bulbs, LEDs, arc discharge lamps, the Sun…). How do lasers create coherent, monochromatic light? Through a process called *Stimulated Emission.* How do lasers create bright, directional light? Via the *Light Amplification* process. Each of these will now be discussed.

Prior to 1917, two resonant optical processes were known: absorption and spontaneous emission (i.e., "luminescence"). These processes have been a large part of the discussion of the preceding chapters, and are sketched in Figure 5.1 for a simple 2-level system. A third process, "induced" or "stimulated" emission (Figure 5.1c) was postulated by Einstein in 1917 (forty years before stimulated emission was first observed in the maser, the predecessor of the laser).[2] In a nutshell, Einstein wrote down simple kinetic rate expressions for each optical process, and set the net transition rate equal to zero at equilibrium (similar to what a good chemical engineer would do for a pseudo-steady state approximation of a reaction intermediate):

$$\frac{dN_1}{dt} = -\frac{dN_2}{dt} = N_2 A_{21} + N_2 B_{21} u_\nu - N_1 B_{12} u_\nu = 0 \qquad (5.1)$$

Here, N_1 and N_2 are the (electron) populations of states 1 and 2; A_{21}, B_{21}, and B_{12} are the Einstein coffeicients for spontaneous emission, stimulated emission, and absorption, respectively; and u_ν is the energy density (J/m^3) of an electromagnetic wave of frequency ν. Einstein then demanded that the form of the rate law at equilibrium (i.e., Equation 5.1) be in accord with the thermodynamics of the day (such a procedure is often called "detailed balance", analogous to the Law of Mass Action in chemistry),[3] which consisted of Planck's Law of Radiation

$$I_\nu = \frac{2\pi h\nu^3}{c^2}\frac{1}{e^{h\nu/kT}-1} \tag{5.2}$$

(where h is Planck's constant, c is the speed of light, and ν is the radiation frequency) and the Boltzmann distribution function, shown here for a two-state system:

$$\frac{N_2}{N_1} = \frac{e^{-E_2/kT}}{e^{-E_1/kT}} \tag{5.3}$$

.

After a few substitutions, two important facts may be deduced. First, since at equilibrium:

$$\frac{B_{21}u_\nu}{A_{21}} = \frac{1}{e^{h\nu/kT}-1} \tag{5.4}$$

,

it can be seen that the stimulated emission rate B_{21} is much smaller than the spontaneous emission rate A_{21} at visible light frequencies and room temperature.

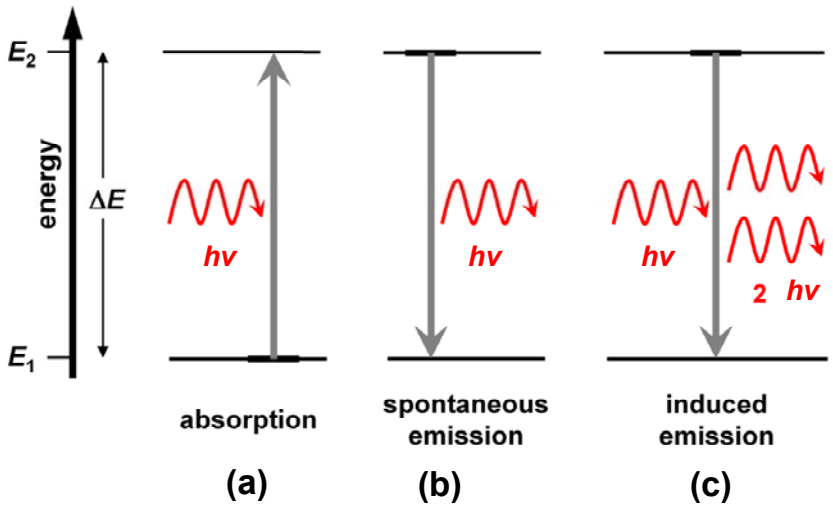

Figure 5.1 Energy level diagrams for a generic two-state system for (a) absorption, (b) spontaneous emission, and (c) induced or stimulated emission. The red arrows represent photons of energy hν, and the gray arrows indicate the direction of the transition.

Second, it can be shown that, for the rate of stimulated emission to exceed absorption, N_2 must be greater than N_1. This non-equilibrium state is called "population inversion", and the process of populating the upper state in a non-Boltzmann fashion is called "pumping". In addition to a pumping source to create electrons in the excited state, it requires a material that has 3 or 4 consecutive energy states with different transition rates. For example, the 2-state system in Figure 5.2a cannot have a population inversion because the emission rate(s) will exceed the absorption rate as soon as $N_2=N_1$. Pumping a 3-level system (Figure 5.2b) can lead to a population inversion since the fast 3→2 transition will leave a surplus of electrons in State 2 waiting to fall to State 1 via a slower 2→1 transition. A 4-level system (Figure 5.2c) is even better because the fast 2→1 transition leaves the "lasing" transition with a near-empty lower state. Finally, because photons are stimulated in the same manner, they have a definite phase relation to each other, and because they result from the same atomic (or molecular) transition, they are the same color; thus, stimulated emission (or laser light) is *coherent* and *monochromatic*.

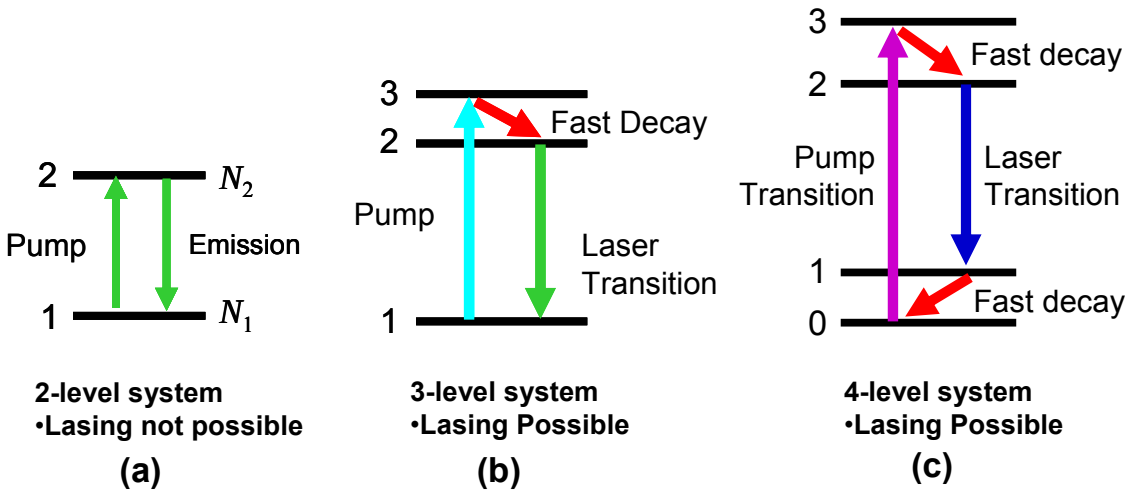

Figure 5.2 Energy level schematics for transitions in (a) 2-level, (b) 3-level, and (c) 4-level systems.

To produce a sizeable amount of stimulated emission (and thus increase the *brightness*), the material in which the population inversion is created is typically placed collinearly between two mirrors, thus forming a "cavity" or a "resonator". The mirrors allow stimulated photons to stimulate more photons upon each pass through the resonator, which amplifies the photon flux. One mirror is partially (say ~10%) transmissive; the stimulated emission escaping the linear cavity is then *directional*. Interestingly, the existence of photons circulating in a cavity necessitates a simultaneous classical description of the intracavity radiation as standing waves. In the longitudinal axis (z-direction, Figure 5.3a), the solutions of the wave equation are normal modes given by:

$$E = \sum_{n=0}^{n=N} E_n \sin[2\pi(\nu_0 + n_z \Delta\nu)] \qquad (5.5)$$

where E_n is the amplitude of the n^{th} longitudinal cavity mode, ν_0 is the fundamental cavity frequency, n_z is the n^{th} mode in the z-direction, and $\Delta\nu$ is the inter-mode

frequency spacing. The first few longitudinal modes are sketched in Figure 5.3b. Their frequency spacing is set by the cavity length:

$$\Delta\nu = \nu_{n+1} - \nu_n = \frac{c}{2L} \tag{5.6}$$

The transverse modes in the x- and y-directions involve a much more complicated derivation. For the case of linearly-polarized light spilling over outside the end mirrors, the transverse modes may be approximated as:[1]

$$U_{pq}(x,y) = H_p(\frac{\sqrt{2}x}{w})H_q(\frac{\sqrt{2}y}{w})e^{-(x^2+y^2)/w^2} \tag{5.7}$$

where H_p and H_q are Hermite polynomials of order p and q. The astute reader will note that the transverse modes take the same form as the eigenfunctions of the quantum harmonic oscillator described in Section 1.5. The first several transverse modes are displayed in Figure 5.3c. It is interesting to note that all of the modes shown here can be seen upon careful misalignment of the output coupler of the laser described in Section 5.6 (e.g., the 00 mode dominates when the output coupler is perfectly aligned, and higher order modes appear in succession with the degree of misalignment).

Now that the fundamentals have been laid down, a few words should be said about the diversity of laser types before moving on. Lasers can be categorized in several ways: by pump mechanism (optical, electrical, collisional, or chemical), by material phase (solid, liquid, or gas), by emission wavelength (IR, visible, or UV), and by time response (continuous or pulsed). For example, the laser used in the photoluminescence and Raman scattering experiments in the previous chapters was

an Argon ion laser, an electrically-pumped, gas phase, visibly-emitting, continuous wave (CW) laser. Conversely, the femtosecond laser that will be described here is an optically-pumped, solid-state, visibly- and NIR-emitting, pulsed laser made from a Titanium-doped sapphire crystal (Ti:sapphire). Its unique properties are described in the next section.

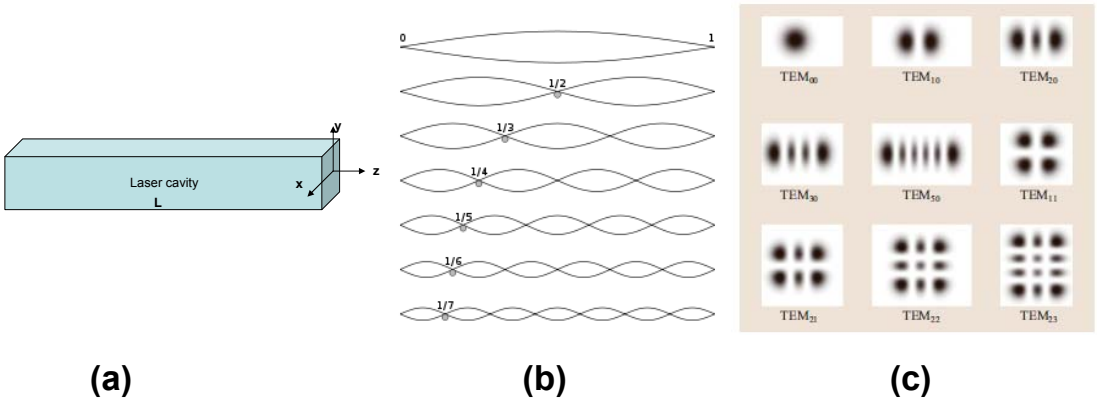

Figure 5.3 (a) A generic laser cavity of length L. (b) The first seven standing-wave solutions in the axial direction, called longitudinal modes, as given by Equation 5.5. (c) The first few transverse modes of the laser cavity, as given by Equation 5.7. The shading is proportional to the intensity (i.e., proportional to the square of the electric field). Reproduced from [5].

5.2 The Ti:sapphire Crystal

The Ti:sapphire crystal is formed by the direct substitution of Ti^{3+} ions for Al^{3+} ions in the sapphire (Al_2O_3) matrix. The electronic structure of the Ti^{3+} ion then consists of a single d-electron outside of a filled Argon shell. This simple picture, however, is perturbed by two interactions – the crystal field of the surrounding sapphire lattice and electron-phonon coupling. Figure 5.4a shows the crystal field splitting of the fivefold degenerate d orbitals into a lower triplet state $^2T_{2g}$ and an upper doublet state ^2E_g.[4] Because both states have even parity (both are "gerade"),

the $^2E_g \rightarrow {}^2T_{2g}$ transition is dipole-forbidden and the lifetime is ~3μs. This is the slow lasing transition. The fast, non-lasing transitions are vibrational relaxations (~ps) within the upper and lower vibronic bands (Figure 5.4b – here, coupling to a continuum of phonon modes is assumed, rather than to a single mode as in Figure 1.14). The wide vibronic bands are the result of strong electron-phonon coupling (large Stokes shift), and result in very broad, displaced absorption and emission bands (Figure 5.4c). Thus, the electron-phonon interaction, so crucial to the ability to glean morphological knowledge from optical spectra of conjugated polymers in the preceding chapters, helps again in a big way here, accounting for both the 4-level lasing in the Ti:sapphire crystal as well as the broadness of its absorption and emission bands. The absorption spectrum is peaked at ~500 nm, perfectly suited for optical pumping from an Argon ion laser (predominantly 488nm and 514 nm emission lines) or a frequency-doubled Nd:YAG laser (532 nm); the former is employed here. The emission spectrum reaches from 680 nm – 1130 nm. This wide tunability makes the Ti:sapphire laser useful in many CW applications (largely replacing dye lasers, which are more difficult to use and maintain). However, the wide emission bandwidth also makes it ideal to create ultrashort pulses. Due to the Heisenberg uncertainty principle, the product of the frequency bandwidth Δν and pulse width Δt must be greater than some constant K (where the constant depends on the pulse shape):

$$\Delta \nu \Delta t \geq K \tag{5.8}$$

Thus the broadest emission sources lead to the shortest pulses. How those pulses are created is the subject of the next section.

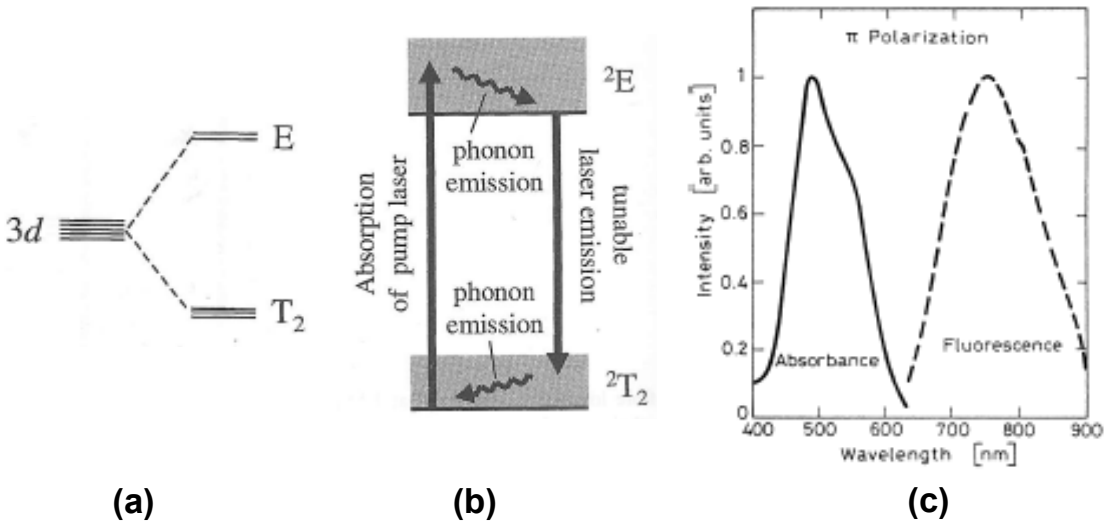

Figure 5.4 (a) Crystal field splitting of degenerate 3d orbitals into an upper doublet state E and a lower triplet state T_2. (b) A 4-level laser system where the fast transitions are vibrational relaxations within upper and lower vibronic bands. This energy diagram results from (a) when strong electron-phonon coupling is present. (c) The absorbance and fluorescence spectra of the Ti:sapphire crystal. All reproduced from [4].

5.3 Mode-locking and Ultrashort Laser Pulses

There are several ways of getting pulsed emission from a laser. For example, Q-switching and cavity dumping involve the placement of an electro-optical or acousto-optical modulator in the laser cavity to limit the gain duration. Pulse widths down to about ~1 ns can be achieved this way; production of shorter pulses is thwarted by the electrical or mechanical time response of the modulator. With a process called mode-locking, however, the pulse duration is limited mainly by the uncertainty principle, and pulses shorter than 1 fs can be created. It is a bit easier to explain what mode-locking is than to explain how it works. Essentially, mode-

locking means the phase of each longitudinal mode is fixed with respect to all the rest, $\varphi_n(t) \rightarrow \varphi_n$ (i.e., the phase of each mode is no longer time-dependent but is a constant). If this mode-locking criterion is met, it easy to see by superposition of the N oscillating modes (Figure 5.5) that the circulating power will be clumped into pulses of width Δt separated by the round-trip time of the cavity, $T_{RT} = 2L/c$ (T_{RT} ~10 ns and $1/T_{RT}$ ~ 100 MHz for a 1-meter long cavity).

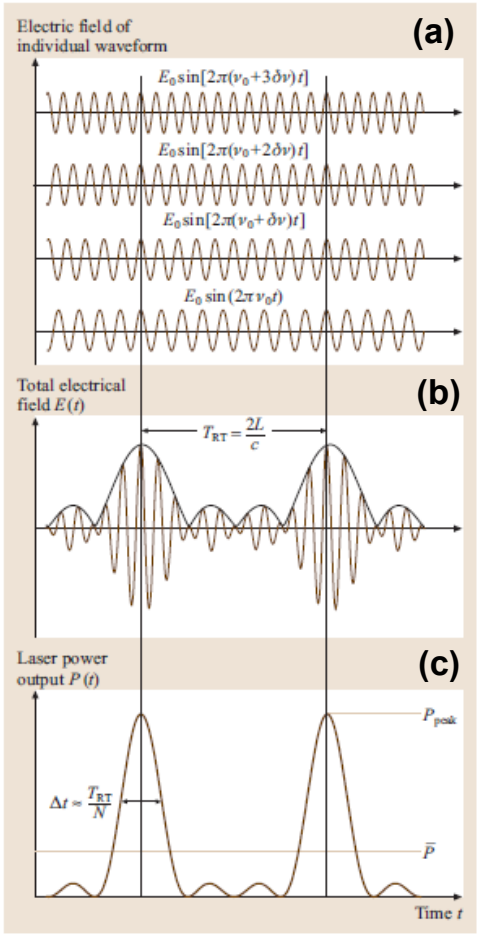

Figure 5.5 A graphical description of the mode-locking process. Panel (a) depicts the first four longitudinal modes of a laser cavity *with constant (zero) phase*, all oscillating simulatenously. Superposition of the electric fields of these modes leads to the composite waveform in (b). The power output of the laser, shown in (c), results from squaring the electric field in (b). Now it can be seen how pulsed or mode-locked output arises through simple mathematics if the phase of each mode is a constant. Reproduced from [5].

Now for the harder part: *mode-locking is caused by the application of some form of amplitude modulation that has a period equal to the cavity round trip time*. There are several practical mode-locking strategies, some being "active" (e.g., firing an electro- or acousto-optical modulator with a clock signal equal to T_{RT}) and others "passive" (e.g., inserting a saturable absorber that selectively enhances the gain of the high-intensity regions of the pulse train). The mode-locking mechanism of Ti:sapphire lasers falls into the latter category, and is called the optical Kerr effect. In analogy with the DC Kerr effect, where a DC voltage changes the refractive index of a material, the optical Kerr effect is a nonlinear phenomenon where the refractive index is dependent on the light intensity:

$$n(t,\vec{r}) = n_0 + \frac{\chi_3 E^2}{2n_0} = n_0 + n_2 I(t,\vec{r}) \tag{5.9}$$

Here, n_0 is the zero-frequency refractive index, E is the electric field magnitude, I is the space- and time-varying light intensity, and χ_3 is the third-order nonlinear susceptibility. The consequences of this third-order nonlinear effect are profound. In the longitudinal direction, the peak of the pulse experiences a higher refractive index than the wings. As the pulse traverses the Kerr medium (Ti:sapphire crystal), this leads to a lowering of the leading edge's frequency (i.e., it becomes more red), and a frequency increase of the trailing edge (Figure 5.6).[1] This process is called self-phase modulation (or "chirping") and leads to both spectral and temporal broadening of the pulse. For a beam oscillating in a (Gaussian) transverse 00 mode (Figure 5.3), the center of the beam will experience a higher refractive index than the outer regions of the beam. The Kerr medium thus acts as a graded-index lens,

focusing the high-intensity light at the beam center more strongly than light from the periphery (Figure 5.6b). An intensity-dependent loss can be created by surrounding the Kerr medium with lenses or curved mirrors. Proper lens/mirror spacing preferentially focuses the intense light back into the gain medium and the low-intensity light to the periphery. This is called "Kerr lens" mode-locking by a "soft" aperture (a physical "hard" aperture can also be inserted as in Figure 5.6b to attenuate unfocused low-intensity light). It is amusing to note that because the intensity fluctuations of the cavity radiation are not normally sufficient to generate the nonlinearity that starts the Kerr lens mechanism, mode-locking must usually be started by tapping a mirror or translating an intracavity prism.[6] Such is the case for the Ti:sapphire laser described in Section 5.6.

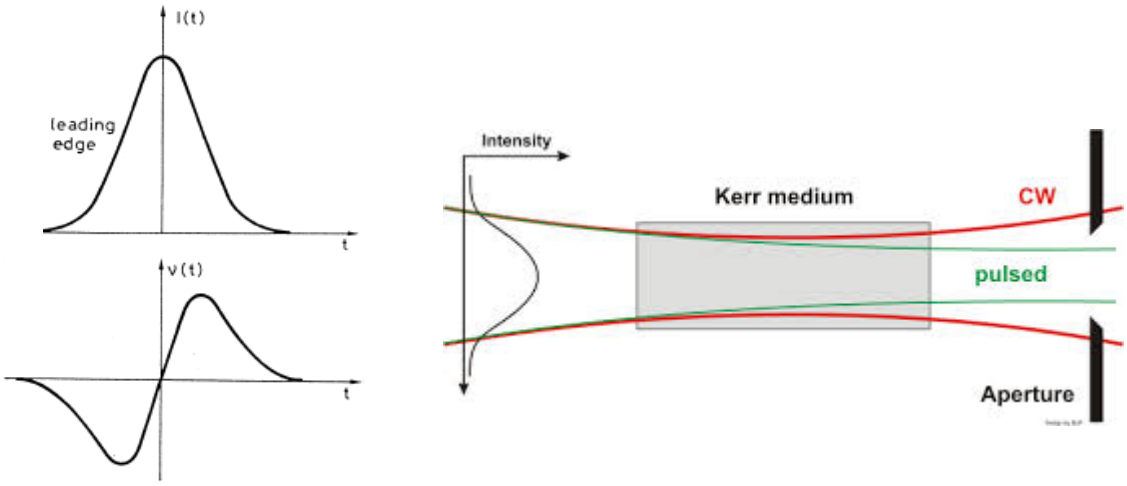

Figure 5.6 The optical Kerr effect. Panel (a) shows how the optical Kerr effect acting on the longitudinal intensity profile I(t) leads to self-phase modulation, where the leading edge is red-shifted to lower frequencies ν(t) and the trailing edge is blue-shifted to higher frequencies. Panel (b) shows how the optical Kerr effect acting on the transverse intensity profile leads to self-focusing or Kerr-lensing. Insertion of a hard aperture leads to a passive mode-locking scheme, where the CW mode is blocked and the pulsed mode is enhanced.

5.4 Applications of the Ti:sapphire Femtosecond Laser

So what is the value in having a laser that can emit femtosecond pulses? Well, such ultrashort pulses have two important features: (1) they have enormous peak power, and (2) they are of shorter duration than most physical phenomena. With regards to (1), a quick back-of-the envelope calculation shows that, for a laser with 1 W average power, a 100 MHz pulse train, and 10 fs pulses, the power dissipated by each pulse (i.e., the peak power) is 1 MW (10 nJ in 10 fs). This makes femtosecond lasers ideal for the study of physical effects which only occur at high powers, such as the nonlinear optical properties of solids and multi-photon absorption. In addition, the high peak powers but relatively low average powers of femtosecond lasers enable their use in the cutting and drilling of metals, so-called "cold micromachining".[7] Feature (2) opens up even more interesting applications for femtosecond lasers, namely, the study of ultrafast chemical dynamics. While Figure 5.7 may not be worth a thousand words, it is probably worth several hundred, and illustrates in more detail what I will summarize here in several sentences. Femtosecond light pulses are of shorter duration than almost any conceivable process in an atom or molecule – on a similar timescale to electronic motion (orbital jumps, electron transfer reactions), shorter than molecular vibrations and molecular dissociation events, and much shorter than the excited state lifetimes for fluorescent and phosphorescent processes. Femtosecond lasers thus made possible pump-probe spectroscopy, whereby an initial femtosecond pulse excites a molecule and a second, slightly-delayed pulse interrogates the result of the excitation. Pump-probe

spectroscopy was used to identify transition states during chemical reactions, earning Ahmed Zewail the 1999 Nobel Prize in Chemistry.[8] Moving right on the spectrum of time to slightly less impressive timescales (~100 ps - ~μs), femtosecond excitation can be used to measure the excited state lifetimes when coupled with a sufficiently fast detector; such transient fluorescence (and transient phosphorescence) experiments is the application for which the Gordon Lab femtosecond laser and photon counting system has been assembled. Fluorescence lifetime measurements have a myriad of applications in biology and chemistry. In addition, the fluorescence lifetime experimental setup can be coupled with x-y scanning stages for fluorescence lifetime imaging spectroscopy (FLIM) or extended to enable fluorescence correlation spectroscopy (which can measure fluctuations caused by diffusion, conformational changes, etc.).[9] One straightforward example of the utility of transient fluorescence is the identification of excited species with wavelength-overlapping fluorescence spectrums. The addition of time as a measurable entity then allows charge-transfer singlet states to be distinguished from spectrally-overlapping triplet states.[10]

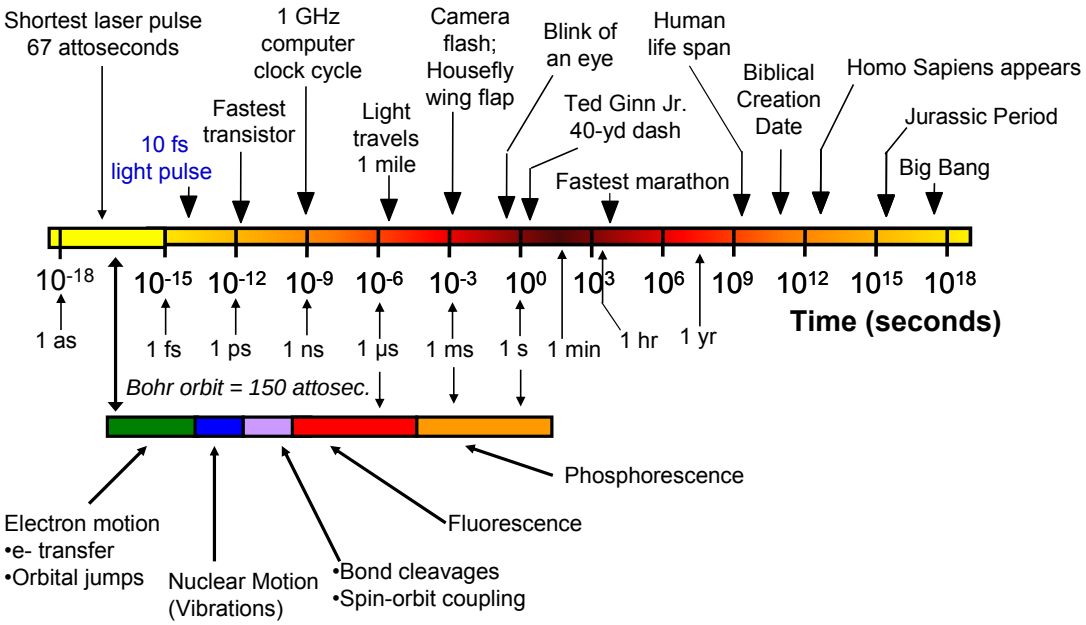

Figure 5.7 Time scales of various molecular and physical processes, from the shortest laser pulse to the age of the universe.

5.5 Photon Detection and Counting in Transient Fluorescence Experiments

Exciting a sample with short light pulses is only half of the battle in setting up a time-resolved fluorescence experiment. The fluorescent photons must also be detected as a function of time. This entails a light detector to transduce the optical signal into an electrical signal and some fast electronics to process the signal and link with a computer. Discussion of photodetectors is rather short because of the limited options at hand and because of the limited number of experimental "knobs" to turn on the photodetector. There are only two classes of photodetectors that have the time resolution to measure decay curves for the fastest-luminescing materials: photomultiplier tubes (PMTs) and avalanche photodiodes (APDs). The combination of detector gain, time resolution, and stability probably favors the use of PMTs over

APDs in most circumstanes; moreover, because the transient luminescence setup in Section 5.6 makes use of a PMT, only PMTs will be considered here. PMTs are vacuum tubes with a photocathode and a series of amplifying stages called dynodes. An incident photon creates a photoelectron at the photocathode (via the photoelectric effect), and this 1-electron signal is amplified by an overall factor of ~10^6-10^8 (the gain of the PMT) via secondary electron emission upon consecutive collisions with the charged dynodes (further details are available in [11]). The important specifications of PMTs include the gain, the transit time (time from photon hitting photocathode to electrical pulse leaving at anode), the transit time distribution or "spread" (TTS, due to the random nature of photoelectron trajectories), and the quantum efficiency curve. By and large, these specifications are fixed upon purchase of the tube – the user should select a tube with a reasonable quantum efficiency in the wavelength range of interest, and a transit time and/or TTS short enough for accurate measurement of the shortest luminescence lifetime of interest (if the gain is not sufficient, a preamplifier can always be used at the PMT output). There is only one knob to turn on the PMT, and that is the voltage; higher voltages increase the gain (gain ~ V^k where k is a constant dependent upon the number of dynode stages and their secondary emission characteristics) and decrease the transit time and TTS (both vary as $V^{-1/2}$),[11] to the extent of their maximum specified values.

The electrical signal arising at the anode (output) of the PMT can be processed by analog or digital ("photon counting") techniques, and also by time- or frequency-domain techniques. (An excellent summary of these techniques, as well as an in-

depth discussion of the Time-Correlated Single Photon Counting technique applied here, is contained in Reference [9]; much of the proceeding discussion will summarize some key concepts contained within). The technique that will be employed here falls into the photon counting and time-domain categories. Time-domain photon counting techniques include gated photon counting (essentially the digitally equivalent of analog boxcar recording) and multichannel scalers (fast digital memory). The former has the drawback of an under-sampled signal due to the small (usually ≤ 4) number of gates, leading to difficulty in reconstructing complex multiexponential fluorescence decay curves. While the latter can process many photons in a single memory sweep (high acquisition rate), its time resolution is limited by the write cycle time of the memory (~1 ns as of 2005,[9] insufficient for many short-lifetime molecules though perfectly fine for slower decays).

The technique employed here, called Time Correlated Single Photon Counting (TCSPC), can record photon events with resolutions down to 1 ps, with the provision that photon counting rates are low (< 0.1 photon per excitation cycle). With low-repetition rate (kHz) pulsed light sources, TCSPC could lead to prohibitively long acquisition times, but with a 100 MHz pulsed Ti:sapphire laser, acquisition time is not an issue. Furthermore, for samples that are sensitive to photobleaching (e.g., biomolecules or organic photovoltaic materials), low excitation power is necessary anyway, so a signal recording scheme based on low-intensity, high-frequency excitation (i.e., hitting the sample with few photons per pulse but lots of pulses) is quite optimal for such materials. TCSPC works by building up a histogram of the

arrival time of randomly-emitted single photon pulses (see Figure 5.8); after sufficient photons have been "binned", the histogram will well-approximate the fluorescence decay curve. For TCSPC (and any other photon-counting techinque), the PMT's electrical output must be terminated appropriately (50 ohm) to allow for distinguishable photon pulses. For TCSPC in particular, the photon pulses must be infrequent enough to guarantee that there are never two (or more) photons per laser pulse to avoid so-called "pileup" distortion to the fluorescence decay curve.

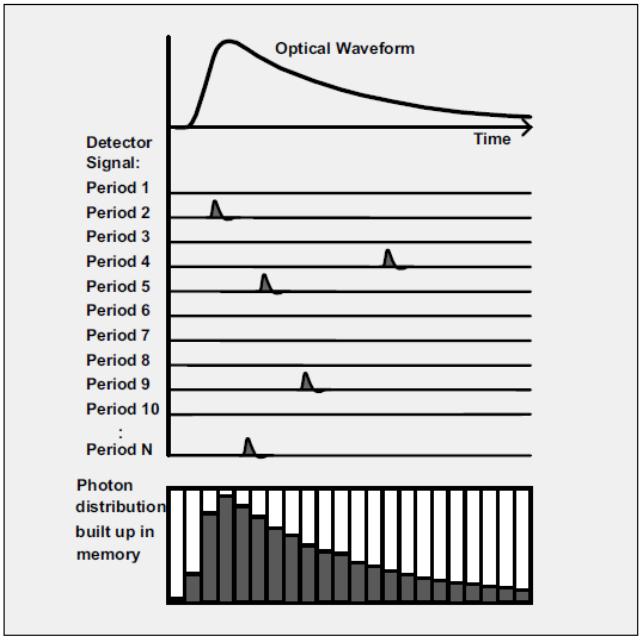

Figure 5.8 Time-Correlated Single Photon Counting (TCSPC). The optical waveform (e.g., a fluorescence decay curve) is built up photon-by-photon. Photon arrival times are measured and binned, building up a histogram. Reproduced from [9].

A block diagram for the TCSPC electronics is shown in Figure 5.9. Physically, this takes the form of a small card that is inserted into the PCI slot of a computer; the blocks shown in Figure 5.9 are all internal to the photon counting card used here.

There are only two inputs: the signal from the PMT (and possibly a subsequent preamplifier), and an electrical signal with the frequency of the laser pulses (in practice, this will be achieved with a fast photodiode, as discussed in the next section). Both signals pass through a threshold discriminator to eliminate spurious low-intensity pulses and a constant fraction discriminator to eliminate rise-time jitter. The time-to-amplitude converter (TAC) then outputs an analog voltage proportional the amount of time between laser pulse and fluorescent photon pulse. After amplification and analog-to-digital conversion, the time interval is stored in memory. The ultimate time resolution of the PMT-TCSPC apparatus is given by the Instrument Response Function (IRF), which is a convolution of the transit time spread of the PMT, the pulse shape of the laser signal, temporal dispersion in the optical system (photon path length differences due to reflections, scattering, etc.), and time jitter in the TCSPC card. In general, the TCSPC jitter is negligible (~1 ps) and the PMT TTS will dominate the IRF for most conventional PMTs (e.g., side-on tubes with ~1 ns transit time spreads). If a fast multichannel plate PMT is employed (TTS ~ 25 ps), then the optical path length and pulse shape from the laser may be limiting factors to the IRF. The shortest IRFs are ~20 ps FHWM with multichannel plate PMTs. Although, as a rule of thumb, the fluorescence lifetime can be accurately measured down to the FWHM of the IRF, determination of lifetimes much shorter than the IRF can be made by fitting the decay curve to a model (e.g., exponential decay).[9]

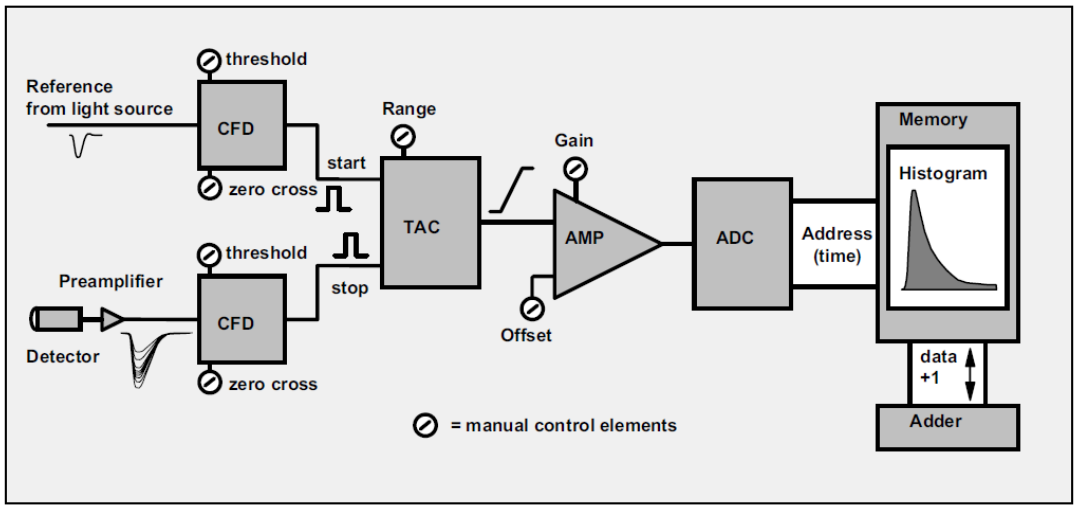

Figure 5.9 Block diagram of the TCSPC system. There are two input channels: a reference or "sync" channel from a photodiode providing the laser pulse stream, and a "detector" or "start" channel containing electrical pulses arising from individual photons. Discriminators are employed to reject spurious pulses. The time interval between reference and detector pulses is measured, converted to an analog signal, and then stored in digital memory. Reproduced from [9].

5.6 The Gordon Lab Femtosecond Laser and Photon Counting System

This section describes the femtosecond laser system and photon counting system employed in the Gordon Lab for the measurement of transient fluorescence spectra. In addition to providing specific information about this custom-built system, the aim here is to create a short guide of best practices and key "tricks" that are not necessarily obvious from the user's manuals of the individual components, but have been learnt the hard way through experience. The complete system is shown schematically in Figure 5.10 and can be divided into five subsections: (1) the Argon ion pump laser, (2) the Ti:sapphire femtosecond laser, (3) external optics (lenses, beamsplitters, frequency upconversion crystals), (4) light detectors and (5) the time-

correlated single photon counting card and associated electronics for signal processing. Each will now be discussed in order.

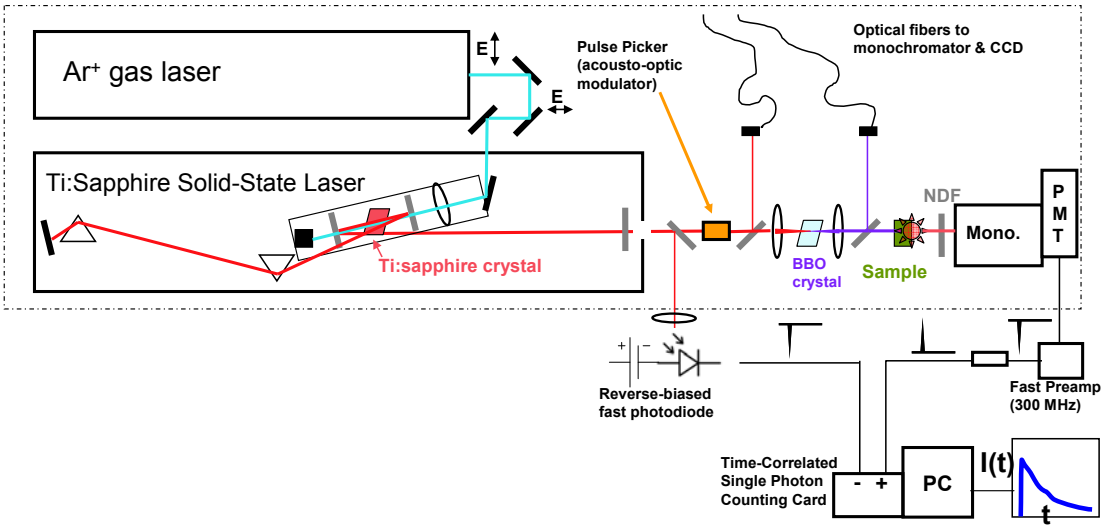

Figure 5.10 The Gordon Lab femtosecond laser and time correlated photon counting system. It consist of an argon ion pump laser, a Ti:sapphire femtosecond mode-locked laser, assorted external optics for beam massaging and frequency doubling, a monochromator and photomultiplier for fluorescence detection, a photon counting card, and some electronics for signal conditioning. The result of this complicated apparatus is a very uncomplicated graph of fluorescence intensity, I(t), vs time (though the time axis has nanosecond resolution).

5.6.1 Argon Ion Pump Laser

The Ti:sapphire laser is optically pumped by a Coherent Innova 70 argon ion laser. Because the Ti:sapphire laser requires significant power to initiate mode-locking (~4.5 W), the Innova must be operated without its intracavity wavelength-selective prism (i.e., all-lines mode). Likewise, the aperture must be fully open (the zero-aperture "0A" setting). With these considerations taken care of, the Innova should provide ~5 W of all-lines laser power at maximum tube power (~33 A, 237 V). A plot of output power vs. tube current is shown in Figure 5.11a. In addition, the Innova produces a very nice TEM_{00} mode (c.f. Figure 5.3c), very important since

Kerr-Lens mode-locking relies on a clean TEM_{00} mode. Unfortunately, the Innova experiences a power decline with time, as presented in Figure 5.11b, and output power usually dips below 5 W after about half an hour of run time. (Note the ~0.2 W offset depending on whether power is measured by the Innova's internal photodiode or an external bolometer; the values discussed here will be taken from the laser's internal meter). These few tenths of a Watt are crucial, as mode-locking is quite stable at powers ≥5 W, becomes unstable (spontaneously reverts to CW mode) at powers between 4.5 and 5 W, and becomes difficult to initiate at powers <4.5 W. While transient fluorescence measurements are still possible at powers <5 W, life is more difficult (higher probability of mode-locking stopping mid-experiment), and the Innova's power droop remains an unsolved problem. It should be noted that there is no more power to be squeezed out of the Innova by cleaning its optics, as the high reflector and output coupler are well-shielded from dust and are very clean.

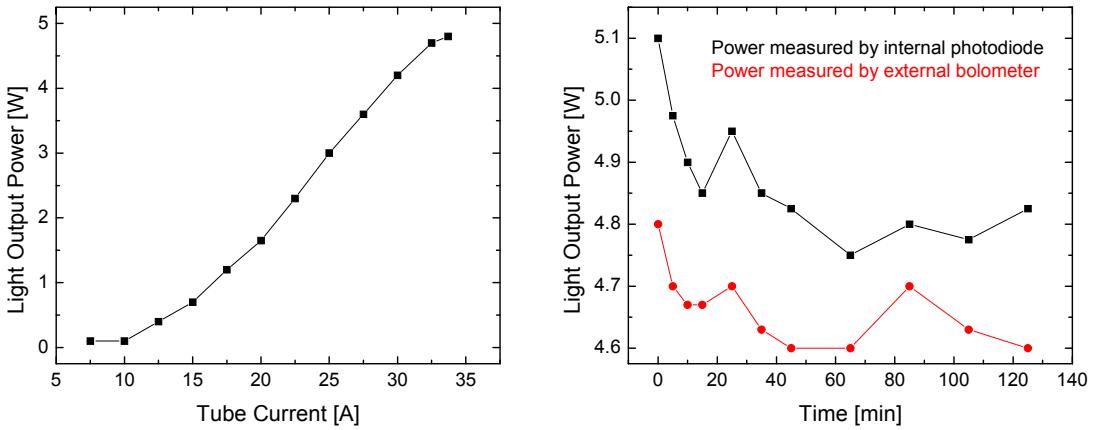

Figure 5.11 Argon ion pump laser power output. (a) Power output vs. tube current. (b) Power output droop with time. There is a slight discrepancy in the output power depending upon the measuring device.

5.6.2 Ti:sapphire Femtosecond Laser

The femtosecond laser employed here is Model TS Ti:sapphire Laser Kit from Kapteyn-Murnane Laboratories. An extensive summary is given in the proprietary user's manual, and this section is meant to be a supplement.[12] The laser is shown in relation to the other parts of the system in Figure 5.10 and is broken down into its individual components in Figure 5.12. As shown in Figure 5.10, the incoming argon ion beam passes through a series of mirrors that both raise the pump beam to a height of 4 in. from the laser table and rotate its polarization (from s-polarization to the p-polarization necessary for efficient coupling to the Ti:sapphire crystal). Any accidental bumping or other misalignment of these mirrors or input mirror (IM, Figure 5.12) necessitates realignment of the entire cavity, as the pump beam *must* be parallel to the plane of the laser table (rigorously 4 in above the table surface) and parallel to the axis of the subassembly (the mount containing optics #2-6, Figure 5.12). Ignore the manual's method of alignment via hitting the "mark" on the backside of the beam dump (this mark is no longer present, and these instructions are a bit ambiguous anyway). Instead, follow the longer procedure that involves removing all components of the subassembly except for #4 (CM1). Though such disassembly may be discomforting at first, with a few times practice the realignment procedure can be done within half an hour. The easiest way to ensure pump beam parallel-ness is to ensure that it passes through the pinhole both at its post holder between optics 2 and 3 *and* at the beam dump (BD) post holder. Alternate the pinhole between beam dumps as the input mirrors are iteratively tweaked (both IM

and those external to the laser housing) to pass the pump beam through the pinhole in both locations. The ~1 ft. separation between beam dump and pinhole post holders allows this procedure to create a sufficiently parallel pump beam; the perfectionist can be assuaged by placing a 4 in-high target another ~2 ft down the laser table along the central axis of the subassembly and assuring that the pump beam is still centered.

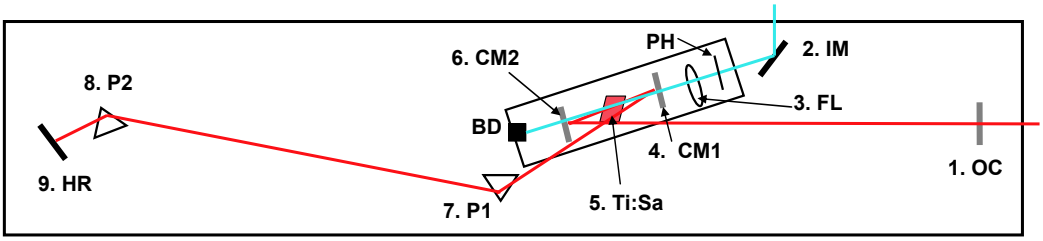

Figure 5.12 The Ti:sapphire laser cavity. Labeled are the output coupler (OC), input mirror (IM), focusing lens (FL), pinhole (PH), curved mirrors (CM1 and CM2), Ti:sapphire crystal (Ti:Sa), beam dump (BD), prisms (P1 and P2), and high reflector (HR). The pump beam from the argon ion laser (~514 nm) is traced in blue, and the Ti:sapphire laser beam (~800 nm) is traced in red.

The next step is to collimate the fluorescent light from the Ti:sapphire crystal. This is described in depth in the manual, but can be condensed into two steps. The first step is to turn off all lab lights, then iteratively adjust any combination of the angles of curved mirrors CM1 and CM2, the positions of prisms P1 and P2, and the angles of the output coupler (OC) and higher reflector (HR) to place the red fluorescent spot on both the HR and the OC. An infrared viewer can be used for this purpose but is not necessary; in fact, a dark room, a pair of blue-blocking laser goggles and a white piece of paper are probably more useful for visual feedback. The second step is just to optimize these positions and angles by maximizing the

output power. Do this by placing a high-pass optical filter just outside the output coupler (to block the pump beam) and a laser power meter after this filter. With a silicon photodiode power meter (with wavelength selection ~800 nm), the fluorescence powers being measured during this optimization process should be on the order of 10s of μW. The lasing threshold is ~100-200 μW of collimated fluorescence; above this level, the power meter reading will become unstable and will jump discontinuously to the 10s of mW as lasing occurs. CW lasing also depends strongly upon the relative positions of the optics in the subassembly. In particular, the focusing lens (#3) must be positioned so that the pump beam waist is in the Ti:sapphire crystal. Furthermore the positions of the curved mirrors CM1 and CM2 with respect to the Ti:sapphire crystal must be optimized for CW lasing. These positions are given in Table 5.1. Proper CW alignment can give an output power of ~550 mW of ~800 nm light for 4.5 W of argon ion pumping. (The 550 mW figure was the best ever recorded, just after a thorough cleaning of all optics; ~400 mW is more realistic after normal dust accumulation).

Table 5.1 Inter-optic distances for continuous wave and mode-locked laser operation. The distances should be measured between the bases of the respective optic mounts with calipers or a rigid ruler as necessary. All distances in inches. Optic numbers refer to those in the laser subassembly as labeled in Figure 5.12.

	Continuous Wave	**Mode-Locked 1**	**Mode-Locked 2**
Distance #3↔#4	0.449	0.449	0.445
Distance #4↔#5	1.134	1.134	1.133
Distance #5↔#6	1.063	1.031	1.022
Distance #6↔edge	2.026	2.059	2.122

Mode-locking requires only a realignment of curved mirror #2 and the prism pairs. First, withdraw prism glass from the beam path inside the laser cavity; mode-locking is impossible with excess prism glass. The spacing between the prism mount and the thumb screw mount (i.e., the length of exposed rail) should be ~0.502 in for Prism 1 and ~0.108 in for Prism 2. Note that most of the fluorescence appears to be "wasted" as most of the circular cross section of the fluorescent beam misses the prisms and the high reflector; this is normal. Next, translate curved mirror #2 (optic #6) towards the Ti:sapphire crystal until the measured distances match the "Mode-Locked 1" column in Table 5.1. This positioning of subassembly mirrors focuses the mode-locked beam back through the crystal and focuses the CW beam to the periphery, as discussed in Section 5.3. The best way to initiate mode-locking is to quickly push and release the spring-loaded mount of Prism 2; this provides the initial fluctuation in intracavity radiation intensity necessary for passive mode-locking.

Mode-locking can be identified by three different methods. The first is to simply watch for a change in the shape of the laser spot as it is projected onto a card. It helps to let the beam travel a few meters so that the spot is a bit larger. The mode-locked spot appears a bit smaller, rounder, and less bright than the CW mode due to the self-focusing effect of the Kerr lens, though the magnitude of change sketched in the laser manual (and reproduced in Figure 5.13a) is exaggerated. Though this is the quickest, simplest method, it might be the most difficult for the novice because it requires a trained eye. A second method is to employ a fast photodiode at the outlet of the laser (which is required for TCSPC anyway), as shown in Figure 5.10. Upon

mode-locking, the oscilloscope trace changes from a constant DC signal to a series of pulses with a frequency of ~88 MHz (or equivalently, ~11 ns pulse spacing). A mode-locked oscilloscope trace is shown in Figure 5.13b. The third method is to fiber-couple the laser beam to a monochromator/detector system and watch how the spectrum changes as CM2 is translated. As shown in Figure 5.14, the CW spectral shape is an extremely narrow spike (FWHM ~0.5 nm), whereas the mode-locked spectral shape is much broader due to self-phase modulation (FWHM ~40 nm). Additionally, whereas the spot shape and oscilloscope signal change more or less discretely as CW lasing transitions to ML lasing, the spectrum gets "jumpy" and erratic at the onset of deviation from the CW mode, giving a useful signal that the user is on the right track. The overall best method to quickly get to mode-locking operation is to center the monochromator at ~800 nm, snap the CCD detector every ~0.5 s, use the right hand to slowly translate CM2 towards the Ti:sapphire crystal, and use the left hand to nudge Prism 2 about once per second. Optimum post-cleaning ~800 nm mode-locked power is ~400 mW per 4.5 W pump power, though 200-300 mW mode-locked power is common for normal use. It should also be noted that there are many combinations of optics #3-6 that provide suitable resonator configurations for stable mode-locking; the configuration given in the "Mode-Locked 2" column in Table 5.1 has anecdotally demonstrated more stable mode-locking than the "Mode-Locked 1" configuration given by the laser manual.

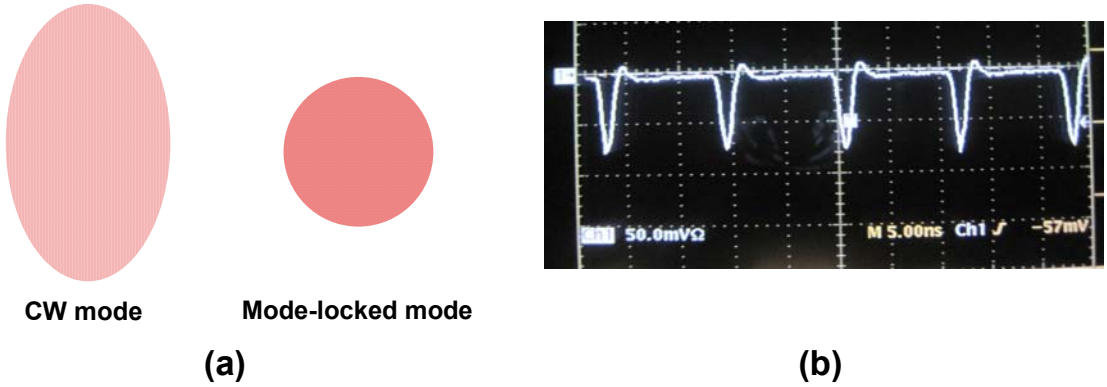

Figure 5.13 (a) The shape of the mode-locked mode is smaller and rounder than the CW mode (note: not to scale). (b) Mode-locked pulse train from the Gordon Lab Ti:sapphire laser on a 500 MHz oscilloscope. The 88 MHz repetition leads to a pulse period of ~11 ns.

At the end of the day, the ease of both CW lasing and mode-locked operation comes down to having sufficient circulating power in the laser cavity. If the laser cavity optics are properly aligned, the only limiting factors are (1) pump power and (2) cleanliness of optics. In addition to the aforementioned power droop of the Innova laser already discussed, thermal fluctuations require frequent realignment of the high reflector; output power can quickly drop from 5 W to ~4 W otherwise. The high reflector tilt knobs should be optimized every 5-10 minutes. Clean optics are also extremely important. Just a few specks of dust can push the intracavity power below the lasing or mode-locking thresholds. From experience, the most susceptible optics to dust are, in order, the prisms P1 and P2, the HR and OC, and finally CM1 and CM2. If lasing is difficult to achieve, blowing these optics off with dried air should be the first remedy (after re-optimizing the HR tilt on the Innova). If this does not result in higher output power, components #1-8 should be removed individually, cleaned, and replaced (starting with the most dust-susceptible). In-situ

optics cleaning is not an option due to an inability to clearly see the optic and inability to apply significant pressure on the cleaning cloth. As for the "cloth" to be used, I have found that "one swipe" methods that involve dragging a folded, moistened piece of lens paper across the optic are ineffective. Instead, glue-free cotton swabs moistened with high-purity methanol should be rubbed on the optic in a spiral pattern, from the center to the outside of the spiral. Output power should be measured subsequently to see if the cleaning helped or harmed; though some rounds of cleaning may increase dirtiness, progress will be eventually made in a "two steps forward, one step back" fashion.

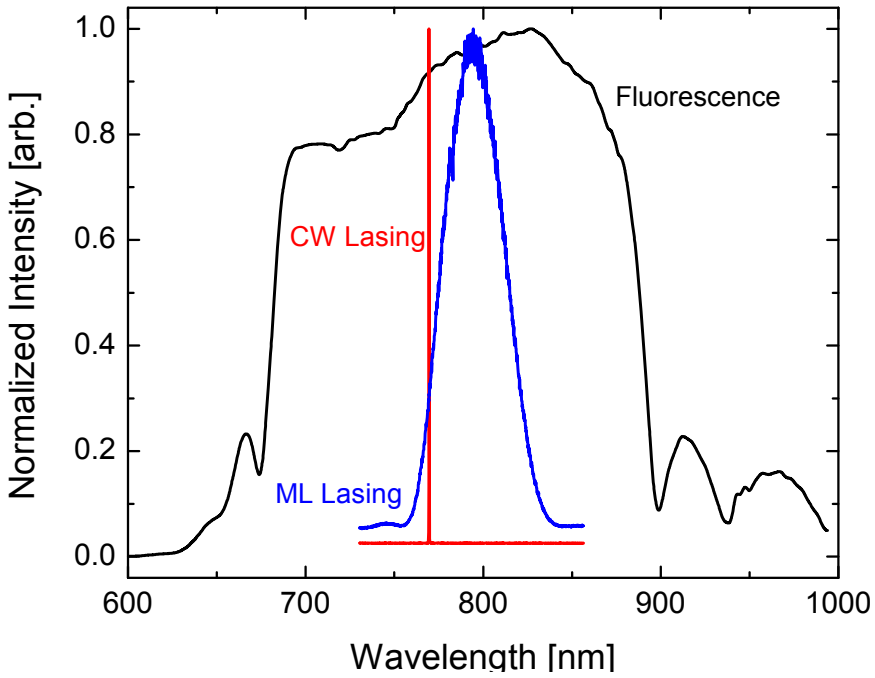

Figure 5.14 Normalized spectral shapes of the fluorescence envelope, continuous wave (CW) laser output, and the mode-locked (ML) laser output. Note that the bumps in the fluorescence spectrum are artifacts induced by the interference filter that was used to block the pump beam as the measurement was made. The tail of the fluorescence envelope at ~650 nm is visible to the unaided eye, allowing alignment to be performed even without the aid of an infrared viewing device.

5.6.3 External Optics

As shown in Figure 5.10, a few optical elements external to the laser cavity are employed. Several beamsplitters are necessary to divert light to the fast photodiode or (optionally) to a monochromator for spectral measurement; simple glass slides suffice here. A 45-mm focal length lens is used to focus the diverted beam to the fast photodiode (the smaller the laser spot, the faster the time response of the photodiode). A 25-mm focal length lens focuses the beam onto a BBO crystal for second harmonic generation (frequency doubling) from ~800 nm to 400 nm. The beam is subsequently collimated with another 25-mm lens. The BBO crystal (Inrad Optics) produces ~250 mW of ~405 nm mode-locked light from ~400 mW of ~800 nm mode-locked light.

5.6.4 Light Detectors

A fast PIN photodiode (Thorlabs FDS010) is used to monitor mode-locking and to provide the synchronization signal for photon counting. The photodiode must be reverse-biased to achieve a suitably fast response time. A simple circuit with applied bias and a low pass filter was built around the photodiode. Because the "sync" input of the photon counting card requires negative pulses, it is best if the photodiode is wired in a "negative output" configuration – see page 304 of reference [9] for details. (A "positive output" configuration is problematic because it requires a subsequent pulse inverter to create negative pulses, which diminishes and distorts the signal. It is better to avoid the pulse inverter altogether and wire for negative pulses). Optimal

applied bias is ~5-10 V; <2 V provides insufficient time response, and >10 V provides no better time response and slightly increases the dark current.

The mode-locked beam, after being doubled by the BBO crystal, excites the sample, and fluorescence is directed to a monochromator. Note that in the actual setup, the monochromator is set at a 90° angle to the pump beam to avoid the onslaught of stray pump light that would result from a head-on geometry. In fact, even with a 90° alignment, a low-pass filter should be placed in front of the monochromator inlet slit to block stray pump light. The monochromator is a Jobin Yvon Micro-HR that has been fitted with a stepper motor to drive the grating and a Hamamatsu R928 photomultiplier tube to detect photons. The combined photoresponse of the grating and the tube allow fluorescence measurement from ~350-950 nm. As stated in Section 5.5, the ultimate time resolution of a photon counting system is given by the Instrument Response Function, which should be dominated by the 1.2 ns transit time spread for the R928 tube. Interestingly, a simple IRF measurement by scattering 800 nm mode-locked light from a water-filled cuvette and into the monochromator gives an IRF, defined as the FWHM of the recorded signal, of ~700 ps for ~1000-1100 V applied to the PMT, significantly less than the transit time spread of the PMT (note that a more rigorous IRF measurement would involve scattering from an aqueous colloid rather than plain water).[9]

5.6.5 Signal Processing Electronics and Photon Counting

As discussed in Section 5.5 and shown in Figure 5.9, time correlated single photon counting is performed by a integrated PCI card that must be fed two input signals:

the reference or "sync" signal that is essentially the pulse train coming from the laser, and the detector signal that consists of randomly-emitted pulses from the fluorescent photons striking the PMT. (The detector signal is called the "start" signal in the language of the photon counting card used here – a Time Harp 200, PicoQuant GmbH). The "sync" input requires ~-200 mV amplitude pulses and comes directly from the negative-output wired photodiode. Pulses as low as -50 mV suffice, but any lower and the Time Harp cannot lock onto all pulses and under-counts the pulse train. The "start" input, conversely, requires +100-1500 mV pulses. Therefore, the output from the PMT is amplified (Ortec VT120 300 MHz preamp) and inverted (Becker & Hickl A-PPI-D pulse inverter). This leads to ~200-400 mV pulses for a PMT voltage of ~4-4.5 V, well suitable for the Time Harp card.

There is one further topic of import that relates to signal processing: modifying the length of all optical paths and signal cables to fit the fluorescence decay within the allotted time window. This is a more advanced topic that is discussed in more depth in the Time Harp manual as well as Reference [9], but will be quickly summarized here in an oversimplified way. Basically, with an 88 MHz laser, the window for time acquisition is ~11 ns. Ideally, the fluorescence decay should start as close to "t=0" as possible in order to fit the complete decay curve within the window. However, without prior consideration of photon and electron transit times, the peak of the decay curve is equally probable to end up anywhere within the 11 ns window. Adding to the optical or electrical path length to either of the reference or detector lines can shift the fluorescence peak toward the far-left, t=0 region of the

acquisition window. Simply adding additional coaxial cable (50-ohm, RG-58) is usually a much easier solution than modifying the optical path. As shown in Figure 5.15, adding 1 meter of electrical cable to the detector line adds a delay of 5 ns (perhaps surprisingly, the speed of signal propagation in 50-ohm coax is about half the speed of light, ~0.6 c). It is useful to have a large supply of coaxial cables of assorted lengths in order to tack additional cable onto either reference or detector lines to optimize the peak of the fluorescence decay.

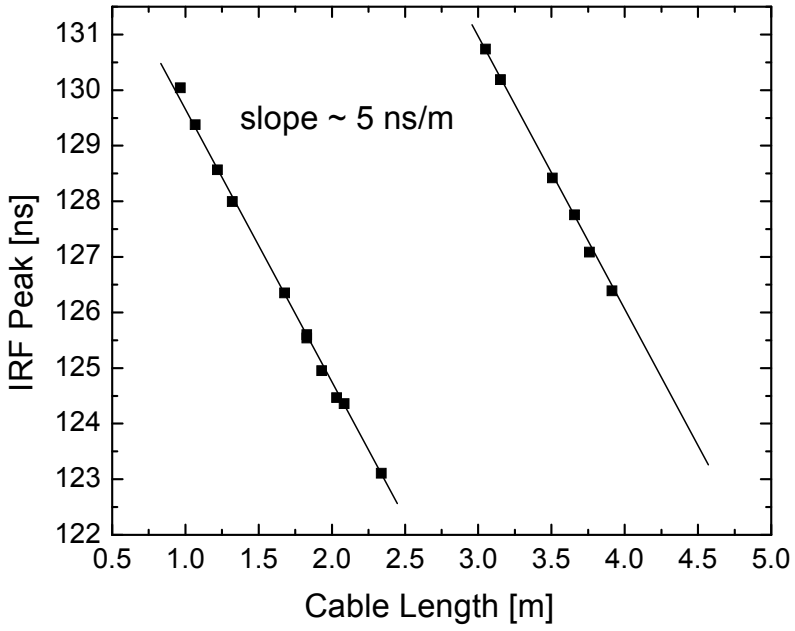

Figure 5.15 The peak of the Instrument Response Function (IRF) as a function of the cable length difference in reference in detector paths. The IRF is obtained by detecting the time response of the ~800 nm mode-locked beam scattered from a water-filled cuvette. The times on the y-axis are arbitrary (i.e., 123 ns could be considered t=0). A cable length of 2 meters means that the reference coaxial cable is 2 meters longer than the detector coaxial cable. The slope of 5 ns/m corresponds to a signal velocity of 20 cm/ns ~ 0.6c. Note that the horizontal gap in the two data sets is approximately twice the cavity length (~3.5 m). The vertical gap between the two data sets is equal to the pulse period (though this is not well represented due to the difficulty in measuring the IRF peak toward the edges of the time window; a cable length of 2.5 m, for example, should correspond to both 122 ns and 122 ns + 11 ns = 133 ns).

5.7 Experimental Results

Getting the lasers, detector, electronics, and photon counting card all working in unison requires a little practice and a little patience, but as of the present, the system is capable of measuring fluorescence lifetimes in the range of ~1 ns to ~11 ns. The time resolution is limited on the low end by the transit time spread of the photomultiplier tube and is limited on the high end by the repetition rate of the laser. However, a pulse picker (acousto-optic modulator) is currently being implemented to reduce the effective sample excitation rate from ~100 MHz to <1 MHz, opening the doors for measuring fluorescence (or phosphorescence) lifetimes out into the μs range. An example of fluorescence lifetime data is given in Figure 5.16, where fluorescence decay curves are displayed for three different conjugated molecules commonly used as laser dyes and other photochemical applications. Each compound was dissolved in ethanol at low concentration (<0.01 mg/ml), and spectra were recorded via ~30 mW 405-nm pulsed excitation in a quartz cuvette (1 cm optical path length). The PMT was operated at 1050 V, and the Time Harp settings were -50 mV for the sync line threshold discriminator, 120 mV for the start line constant fraction discriminator (CFD), and 20 mV for the CFD zero crossing level. Incident light intensity was reduced using a combination of neutral density filters and narrow inlet slits such that the total count rate was $<10^5$ counts per second, or <1 detected photon per ~1000 laser pulses (guaranteeing the absence of pile-up distortion). Acquisition times were ~10-60 s. The measured lifetimes of Coumarin 6 and Eosin Y are in near-exact agreement with literature (2.55 ns and 2.86 ns, respectively,

though the precision is probably limited to two significant digits).[13,14] Only the measured lifetime of Methylene Blue, τ=0.64 ns, is at odds with the literature value of 0.47 ns,[15] but this is almost certainly due to the TTS-limited time resolution of our system (IRF ~700 ps). Future work involves the extension of lifetime measurements to lifetimes >11 ns and to thin films of organic photovoltaic materials.

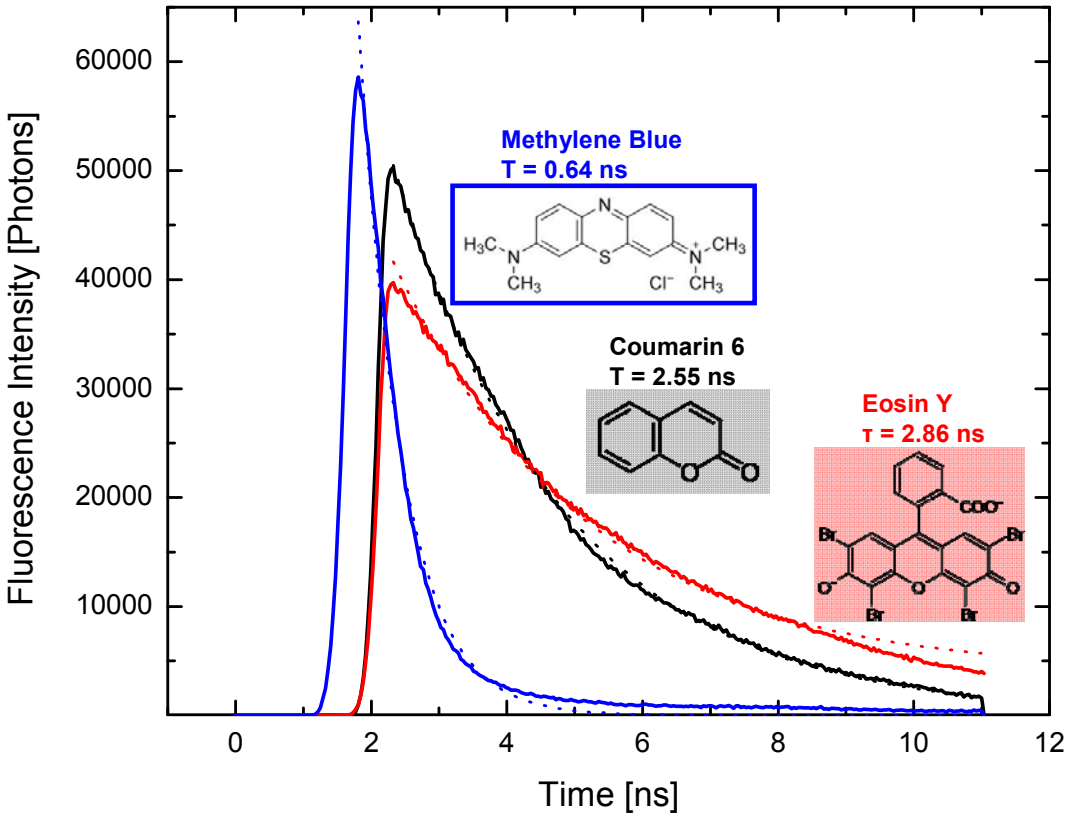

Figure 5.16 Transient fluorescence spectra of selected dye molecules, measured with the Gordon Lab femtosecond laser and photon counting system. The time axis is arbitrary; curves can be shifted left or right for convenience. The solid curves are the measured data, and the dotted curves are least squares fits to a single exponential decay model of the form $y = y_0 + A*\exp[-t/\tau]$.

5.8 References

[1]O. Svelto. *Principles of Lasers,* (Springer, New York, 1998).

[2]A. Einstein. *Phys. Z.* **18,** 121 (1917).

[3]H. Metiu. *Physical Chemistry: Quantum Mechanics,* (Taylor & Francis, New York, 2006).

[4]M. Fox, *The Optical Properties of Solids,* (Oxford University Press, New York, 2001).

[5]F. Träger (Ed.). *Handbook of Lasers and Optics,* (Springer, New York, 2007).

[6]P. M. W. French. *Rep. Prog. Phys.,* **58,** 169 (1995).

[7]C. Breck Hitz, J. Ewing, and J. Hecht. *Introduction to Laser Technology, 4th Edition,* (John Wiley & Sons, Hoboken, 2012).

[8]A. H. Zewail. Nobel Lecture (1999).

[9]W. Becker. *Advanced Time-Correlated Single Photon Counting Techniques,* (Springer, Berlin, 2005).

[10]I. Riisness and M. J. Gordon. *Appl. Phys. Lett,* **102,** 113302 (2013).

[11]*Photomultiplier Tubes: Basics and Application, 3rd Edition.* Hamamatsu Corporation (2006).

[12]*Instruction Manual, Model TS Ti:Sapphire Laser Kit,* Kapteyn-Murnane Labs (2006)

[13]*Lifetime Data of Selected Fluorophores,* ISS Biomedical technical note, http://www.iss.com/resources/reference/data_tables

[14]A. V. Deshpande and N. B. Iyer, *Journal of Luminescence,* **46,** 339 (1990).

[15]L M. Moreira, J. P. Lyon, A. P. Romani, D. Severino, M. R. Rodrigues and H. P. M. de Oliveira, *Phenotiazinium Dyes as Photosensitizers in Photdynamic Therapy: Spectroscopic Properties and Photochemical Mechanisms,* Intech Open Science (2012).